

Stokes parameters of skylight based on simulations and polarized radiometer measurements

Der Fakultät für Physik und Geowissenschaften

der Universität Leipzig

eingereichte

DISSERTATION

zur Erlangung des akademischen Grades

Doktor der Naturwissenschaften
(Dr. rer. nat)

vorgelegt

von **M.Sc. Li Li**

geboren am 21.03.1983 in Beijing, China

Leipzig, den 18.01.2016

1. Berichterstatter: Prof. Dr. Manfred Wendisch
2. Berichterstatter: Prof. Dr. Zhengqiang Li

Datum der Beschlussfassung: 24.10.2016

Bibliographic Description:

Li, Li

Stokes parameters of skylight based on simulations and polarized radiometer measurements

University of Leipzig, Dissertation

156 p., 81 ref., 42 fig., 8 tab.

Abstract

A method to calculate the Stokes parameters Q , U , as well as angle of polarization (AoP) from the new generation CIMEL Dual-Polar sun/sky radiometer CE318-DP polarized skylight measurements is developed in this thesis. Besides the degree of linear polarization ($DoLP$) and the total radiance I , the parameters Q , U , and AoP have much potential to improve retrievals of aerosol microphysical and chemical properties. However, they have not been derived based on the CE318-DP so far because they change with the reference plane that is hard to know due to an uncontrolled initial angle related to installation of the optical sensor head to the automated mount of this type of instrument. In this work, the polarization pattern of skylight with the direction of polarization perpendicular to the scattering plane (i.e., the principal plane in the solar principal plane geometry) is applied to correct the initial angle and then to obtain Q , U , and AoP . The perpendicular and parallel polarized radiances I_r and I_l , as well as the linear depolarization ratio ρ are further derived after Q is known. A new polarized almucantar geometry based on CE318-DP is measured to illustrate abundant variation features of these parameters. These new polarization parameters in conjunction with $DoLP$ and I are analyzed based on some typical long-term sites within the Sun/sky-radiometer Observation NETwork (SONET) and a joint site of the AErosol RObotic NETwork (AERONET) in China. Results calculated in this work are consistent with previous results, and generally comparable with the vector radiative transfer simulations and the measurements by other polarimetric instrument. Considering a 1° discrepancy of AoP , 3% fractional uncertainty in I and 0.005 uncertainty in $DoLP$ propagated to Q and U , the uncertainties of Q in both of solar principal and almucantar planes and that of U in the almucantar geometry are acceptable.

Contents

1	Introduction	1
1.1	Motivation	3
1.2	Objectives	6
1.3	Outline of this thesis	7
2	Theoretical basis	9
2.1	Quantitative description of polarized skylight	9
2.1.1	Definitions of polarization parameters	9
2.1.2	Angle of polarization and signs of Stokes parameters	12
2.1.3	Perpendicular and parallel polarized radiances	13
2.2	Interaction of polarized light with atmospheric particles	15
2.2.1	Scattering theory	15
2.2.2	Single scattering codes	24
2.2.3	Optical parameters	26
2.3	Radiative transfer of polarized light in the atmosphere	31
2.3.1	Theory of polarized radiative transfer	31
2.3.2	Vector radiative transfer models	36

3	Measurement of skylight polarization	39
3.1	Instrument description	39
3.2	Calibration of the polarized radiances	44
3.3	Measurement sites	47
4	Method of Stokes parameter derivation	50
4.1	Definitions of the reference frames	50
4.2	Calculation of the polarization parameters	53
4.3	Results	63
4.3.1	Solar principal plane geometry	64
4.3.2	Almucantar geometry	84
5	Validation and uncertainty assessment	93
5.1	Validation of the polarization parameters	93
5.1.1	Comparison with previous measurements of $DoLP$ and I	93
5.1.2	Comparison between measurements and model results .	94
5.1.3	Comparison with the AMPR measurements	98
5.2	Uncertainty estimation	101
6	Concluding remarks	111
6.1	Summary	111
6.2	Outlook	118
	Bibliography	121

CONTENTS

Nomenclature	131
Acronyms	136
List of Figures	137
List of Tables	145
Acknowledgments	147
Curriculum Vitae	149

Chapter 1

Introduction

Polarization is a fundamental property of electromagnetic (EM) waves, that is defined as the distribution of the electrical field in the plane normal to the propagation direction (Liu and Voss, 1997; Kokhanovsky, 2003; Hovenier et al., 2004). Light is composed of an ensemble of EM waves. Natural light, such as the solar radiation incident at the top of the atmosphere (TOA), is unpolarized in which the orientation of the oscillating electrical field vector changes randomly. Scattering interactions of the incident solar radiation with atmospheric suspended particles, for example, the molecular scattering (i.e., the Rayleigh scattering), the spherical aerosol/cloud particle scattering (i.e., the Mie scattering), and the nonspherical aerosol/cloud particle scattering, change the state of polarization. The scattered skylight becomes partially polarized during penetration of the incident sunlight through the atmosphere (Kokhanovsky, 2003; Smith, 2007).

A characteristic polarization pattern exists in clear sky, which is related to the position of the sun, the distribution of various atmospheric constituents, and the properties of the underlying surface (Coulson, 1988; Horváth and Varjú, 2004). In cloudy sky or some other atmospheric conditions, a polarization pattern of skylight is also evident, which has been widely used by some insects and human beings for navigation (Horváth and Varjú, 2004; Smith, 2007). However, in different atmospheric conditions, the details of

skylight polarization are different depending on the properties of scattering particles. They can provide unique information on the optical and microphysical properties of atmospheric particles.

Atmospheric aerosol is the ensemble of colloidal suspension of liquid or solid particles in the atmosphere. It has important influences on the global climate either directly by scattering and absorption of the solar radiation or indirectly by affecting cloud droplet concentration or cloud radiative properties (Wendisch and von Hoyningen-Huene, 1994; Dubovik et al., 2002; Wendisch and Yang, 2012). Atmospheric aerosol particles have been recognized as one of the most uncertain atmospheric components due to the poor knowledge of their complex optical and microphysical properties, chemical compositions, as well as rapid spatial and temporal variations of these properties (Boucher et al., 2013). The polarization of skylight is sensitive to microphysical properties and chemical compositions of the atmospheric aerosol particles (e.g., particle size, shape, complex refractive index, vertical profile) (Kokhanovsky, 2003; Smith, 2007; Zeng et al., 2008; Cheng et al., 2010; Wang et al., 2014b). Qualitative and quantitative explanations of skylight polarization have been applied to study atmospheric aerosol properties for decades (Vermeulen et al., 2000; Li et al., 2006; Hasekamp and Landgraf, 2007; Li et al., 2009; Bayat et al., 2013; Arai, 2013). Skylight polarization measurements can effectively improve retrievals of the fine mode size distribution, the real part of refractive index, and the sphericity parameter of aerosol particles (Dubovik et al., 2006; Li et al., 2009). In addition, polarization data has high potential to derive more information about aerosol particle shape and types (Emde et al., 2010; Nousiainen et al., 2011).

Several spaceborne and airborne polarization instruments have been designed to detect atmospheric aerosol properties. For example, POLDER (Polarization and Directionality of Earth’s Reflectances), APS (Aerosol Polarimetry Sensor, failed to launch), RSP (Research Scanning Polarimeter), DPC (Directional Polarimetric Camera), 3MI (Multi-Viewing Multi-Channel Multi-Polarization Imaging Mission), SGLI-VNR (Second Generation Global Imager-Visible and Near Infrared Radiometer), and AMPR (the advanced Atmosphere Multi-angle Polarization Radiometer) (Cairns et al., 1999; Deuzé

et al., 2001; Peralta et al., 2007; Okamura et al., 2008; Gu et al., 2010; Song et al., 2012; Marbach et al., 2013). Ground-based polarization instruments, such as the polarized CIMEL sun/sky radiometer CE318-2 and the Polarization Radiance Distribution Camera System RADS-IIP, avoid problems with effects of surface background on polarization measurements and provide more polarization information about atmospheric particles (Voss and Liu, 1997; Liu and Voss, 1997; Bayat et al., 2013).

The Dual-Polar sun/sky radiometer CE318-DP, manufactured by CIMEL¹, is a new generation of ground-based polarization instrument for atmospheric aerosol remote sensing. It has been introduced into the AERosol RObotic NETwork (AERONET) and the Sun/sky-radiometer Observation NETwork (SONET) to provide long-term and continuous polarization observations for aerosol characterization around the world and focus on China, respectively (Holben et al., 1998; Li et al., 2015). By comparison with the previous version, the polarized radiometer CE318-2 that measures sky polarization only with one channel (i.e., at 870 nm wavelength), the new CE318-DP has enhanced capabilities of detecting linear polarization of skylight in an extended spectrum with center wavelengths from 340 to 1640 nm (Li et al., 2015). More information on aerosol properties is expected to be obtained from the multi-wavelength skylight polarization measurements of the CE318-DP.

1.1 Motivation

The polarization state of light is commonly described by a Stokes vector consisting of four parameters I , Q , U , and V (Horváth and Varjú, 2004; Hovenier et al., 2004; Bhandari et al., 2011). These Stokes parameters are defined with reference to vectors parallel and perpendicular to a reference plane (Bhandari et al., 2011). Among them, I is the total spectral radiance of light (i.e., the radiant energy confined in a given direction per unit time per unit wavelength/frequency range per unit solid angle per unit area perpendicular to the given direction) which can be decomposed into the components polarized

¹CIMEL Electronique: 172 rue de Charonne 75011 Paris, France (www.cimel.fr)

linearly in a reference plane and perpendicular to it (i.e., I_l and I_r); Q and U quantify the fraction of linear polarization parallel to the reference plane and at 45° with respect to the reference plane, respectively; and V gives the fraction of right-handed circular polarization (Horváth and Varjú, 2004). Considering that the contribution of V characterizing circular polarization is negligible for the scattered skylight, the partially polarized skylight is predominantly linear polarized (Coulson, 1988; Tilstra et al., 2003). Then it can be considered as a superposition of unpolarized light and linearly polarized light and is usually described by the first three components of the Stokes vector (i.e., I , Q , and U) (Horváth and Varjú, 2004; Li et al., 2009). The Degree of Linear Polarization (*DoLP*) and the Angle of Polarization (*AoP*) derived from the Stokes parameters I , Q , and U are also frequently used to describe amount of linear polarization and orientation of polarization with respect to the reference plane, separately.

Although the new generation CE318-DP detects linear polarization of skylight in multi-channels, only the *DoLP* and the Stokes parameter I have been obtained from its polarization measurements so far. Other Stokes parameters Q and U , as well as the *AoP* are currently not available. This is due to the fact that, *DoLP* and I are constant with different reference planes, but the value of Q , U , and *AoP* depend on reference plane and corresponding reference coordinate system. For CE318-DP, the reference plane is not fixed but is related to installation of the instrument. So, Q , U and *AoP* are difficult to derive from the CE318-DP measurements. However, they contain unique information on atmospheric aerosol particles. Calculation of these additional parameters will bring many benefits to improve atmospheric aerosol remote sensing:

First, the Stokes parameters Q and U contain valuable information not only on intensity of the linearly polarization, but also on the polarization orientation which is influenced by atmospheric aerosol particles. Simulation results have shown that Q and U in both the solar principal plane (defined as the plane containing both the directions of incident sunlight and the local zenith) and the almucantar plane (contains directions with the same solar zenith angle but varying azimuthal angles) are highly sensitive to aerosol

particle size, shape, real part of complex refractive index (Li et al., 2013). The strength variation values of Q and U at the peak positions in the principal and almucantar planes could be utilized to obtain information on aerosol properties and then help to identify aerosol types.

Second, when Q is known, the parallel and perpendicular polarized radiances I_l and I_r can be separated from the total radiance I (these quantities are spectral which will be omitted in the following discussions). Unlike the Stokes vector, I_l and I_r are scalar parameters (He et al., 2014). Previous study has shown that, the polarized portion of the Rayleigh scattering (i.e., elastic scattering of light by particles much smaller than the wavelength of the radiation) is always polarized perpendicular to the scattering plane. However, the polarized component of the Mie scattering (i.e., the scattering of light by a homogeneous sphere where the size of the scattering particles is comparable to the wavelength of the light) from atmospheric particles can be polarized either parallel or perpendicular to the scattering plane (Pust and Shaw, 2008). I_l and I_r depend on the properties of the scattering particle. The unique features of them can be used for atmospheric aerosol remote sensing. Thus, it is meaningful to calculate the Stokes parameter Q of skylight and then to separate the parallel and perpendicular polarization components from the total radiance.

Last but not least, the spatial distribution of the angle of linear polarization of skylight is also influenced by atmospheric particles. Although AoP of electromagnetic radiation scattered by aerosol and cloud particles in hazy or partly cloudy skies exhibits little change from the clear sky around the viewing angles of maximum $DoLP$, AoP that depart from the clear sky have also been measured in other viewing angles in the cases of hazy or cloudy conditions (Horváth and Varjú, 2004). Pust and Shaw (2008) have shown that the AoP itself provides information about the droplet size distribution of clouds. Simulation results have also shown that the angle of polarization of skylight in the almucantar plane not only is sensitive to particle shape, real and imaginary of parts of complex refractive index, but also has a feature that is constant for different size of particles (see Fig. 5.9 in Chapter 5).

In general, the polarization parameters Q , U , and AoP have significant potential to gain detailed information on aerosol microphysical properties and chemical compositions. The potential of these additional parameters increases the value of measurements of the SONET, which has more than half of its observation stations equipped with the new CE318-DP. Abundant polarization raw data have been collected within the SONET to study properties of different types of aerosol particles in key areas of China. These new polarization parameters obtained from the raw polarization measurements will be beneficial for improving retrievals of aerosol properties and for understanding nonspherical aerosol particles according to the special sensitivities of skylight polarization to particle shape. Meanwhile, they are also very meaningful for validating polarization measurements and aerosol products of spaceborne and airborne instruments (e.g., DPC, AMPR).

1.2 Objectives

In order to improve the understanding of aerosol properties based on skylight polarization measured by the new CE318-DP, the objectives of this thesis are:

- to develop a method to derive the Stokes parameters Q , U , and the AoP from ground-based CE318-DP measurements. Subsequently, the parallel and perpendicular polarized radiances I_l and I_r are obtained from the Stokes parameter I . The linear depolarization ratio of skylight ρ are then derived from I_l and I_r . Thus, polarization parameters of skylight obtained from CE318-DP measurements are enriched from the current $DoLP$ and I to Q , U , AoP , I_l , I_r , and ρ .
- to enhance the data harvest of skylight polarization measurements by extending the observations of CE318-DP from the current solar principal plane geometry to the almucantar geometry considering that the Stokes parameter U and the angle of polarization contain less information in the solar principal plane.
- to analyze the features of these polarization parameters (including I , Q ,

U , $DoLP$, AoP , I_l , I_r , and ρ) influenced by different aerosol types based on long-term observations in some key areas of China within the SONET.

1.3 Outline of this thesis

In response to the needs for obtaining more polarization parameters of skylight from the CE318-DP measurements and for improving aerosol remote sensing according to the special sensitivities of skylight polarization to aerosol properties, the main target of this study is introduction of a method to calculate Q , U , AoP and to derive I_l , I_r , as well as ρ from the CE318-DP measurements. In addition to $DoLP$ and I , these new obtained skylight polarization parameters affected by typical aerosol particles are analyzed based on long-term observations in some key areas of China within the SONET. The thesis is organized as follows:

Chapter 2 provides the concepts of polarization parameters for describing linearly polarized skylight and especially discusses the relationship between AoP and the sign of Stokes parameters Q and U in detail. The scattering theory and some single scattering codes (e.g., Mie code, T -matrix code, spheroids kernels) describing interactions of the polarized skylight with atmospheric particles, as well as some optical parameters describing the optical properties of particles are introduced. Furthermore, the vector radiative transfer equation that describes radiative transfer of polarized light in the atmosphere is elaborated, and two representative radiative transfer models (i.e., SOS and SCIATRAN) are presented, which are later used to simulate the multi-spectral multi-angle polarized skylight observed by the ground-based CE318-DP and to simulate sensitivities of the observed polarized skylight to different aerosol properties.

In Chapter 3, polarization measuring principles of the new generation CE318-DP are introduced, which are based on a combination of different polarizers and filters. Furthermore, the polarized observation geometry is extended from the solar principal plane to the almucantar plane considering that some polarization parameters reveal enhanced sensitivities in the

almucantar geometry. To calculate the Stokes parameters I , Q , and U from three radiance measurements, absolute radiometric calibration coefficients for the polarized channels need to be known. That is why the calibration process is briefly introduced. The long-term sites of CE318-DP polarization measurements within the SONET are listed in this chapter. Polarization measurements for selected cases at representative sites will be analyzed.

Chapter 4 introduces the two reference planes and corresponding coordinate systems in the instrument and sky frames related to the CE318-DP polarization measurements. On this basis, a method to correct initial angle of the instrumental reference plane, and to calculate the Stokes parameters Q , U , and AoP is introduced. The results of skylight polarization parameters in the solar principal plane and the almucantar geometries are discussed in detail. For the polarized principal plane observations, five typical cases influenced by different aerosol types (including a haze polluted urban case at the “Beijing-RADI” site, a rural case at the “ZhangyeHH” site, a clean continental case at the “Lhasa” site, a mineral dust case at the “Minqin” site, and a maritime case at the “Zhoushan” site) are illustrated. Furthermore, a heavy haze polluted and a clear sky conditions are analyzed based on the new polarized almucantar observations at the “Beijing-RADI” site.

In Chapter 5, results of the Stokes parameters I , Q , U , the $DoLP$ and AoP calculated in this study are evaluated by comparing with the former results of I and $DoLP$, with the results simulated by the Successive Order of Scattering (SOS) vector radiative transfer model, and with synchronous measurements of the advanced Atmosphere Multi-angle Polarization Radiometer (AMPR). Among these polarization parameters, the algorithm to derive Q and U from the CE318-DP measurements is a key result of this thesis. Uncertainties in the derived polarization parameters Q and U are evaluated.

Chapter 6 contains the summary and outlook of this study.

Chapter 2

Theoretical basis

2.1 Quantitative description of polarized sky-light

2.1.1 Definitions of polarization parameters

Polarization of light can be described by different means (e.g., the polarization ellipse, the Poincaré sphere, the Jones vector) (Bass et al., 1995; Liou, 2002). The most common way is the four-dimensional Stokes vector \vec{S} introduced by G. Stokes in 1852 (Goldstein, 2003; Horváth and Varjú, 2004; Wendisch and Yang, 2012):

$$\vec{S} = \begin{pmatrix} F \\ Q \\ U \\ V \end{pmatrix} = \frac{1}{2} \sqrt{\frac{\epsilon}{\kappa}} \cdot \begin{pmatrix} E_l \cdot E_l^* + E_r \cdot E_r^* \\ E_l \cdot E_l^* - E_r \cdot E_r^* \\ E_l \cdot E_r^* + E_r \cdot E_l^* \\ i(E_l \cdot E_r^* - E_r \cdot E_l^*) \end{pmatrix}, \quad (2.1)$$

where E_l and E_r represent the electric field components of the scattered wave parallel (l) and perpendicular (r) to the reference plane, respectively. By definition, all Stokes parameters have the units of irradiance (i.e., radiant energy confined in a given direction per unit time per unit area perpendicular to the given direction, in units of W m^{-2}). F is a measure of the total irradiance of

light. Q and U quantify the irradiance of parallel minus perpendicular components and the irradiance in reference to a polarization plane that is tilted by $\pm 45^\circ$, respectively. They describe the linearly polarized radiation and depend on the choice of reference plane. V describes the circularly polarized irradiance. $i = \sqrt{-1}$. The superscript “*” indicates complex conjugate. ϵ and κ are the electric permittivity and the magnetic permeability. The factor $(1/2)\sqrt{\epsilon/\kappa}$ is constant and is usually omitted (Wendisch and Yang, 2012).

In this study, polarization of light is measured by the sun/sky radiometer. From an observer’s point of view, radiometer measures the amount of radiant energy dE , in a wavelength interval $d\lambda$, which is transported in a time interval dt , through an element of surface area d^2A , and in directions confined to an element of solid angle $d^2\Omega$, having its axis perpendicular to the surface elements $\cos\theta$. Then the Stokes vector can generally be denoted by $(I, Q, U, V)^T$ with the units of radiance ($\text{W m}^{-2} \text{ nm}^{-1} \text{ sr}^{-1}$) (Liou, 2002; Horváth and Varjú, 2004; Hovenier et al., 2004).

Besides the Stokes vector, further polarization parameters are deduced from the Stokes parameters to describe the polarization state of light:

The Degree of Polarization (DoP) is given by

$$DoP = \frac{\sqrt{Q^2 + U^2 + V^2}}{I}; \quad 0 \leq DoP \leq 1. \quad (2.2)$$

For completely polarized radiation, $Q^2 + U^2 + V^2 = I^2$, thus $DoP = 1$; and for unpolarized radiation, $Q = U = V = 0$, thus $DoP = 0$.

The Degree of Linear Polarization ($DoLP$) is defined as

$$DoLP = \frac{\sqrt{Q^2 + U^2}}{I}; \quad 0 \leq DoLP \leq 1. \quad (2.3)$$

For the solar principal plane observations, the viewing direction is in the principal plane. Then, the principal plane, the local meridian plane and the scattering plane are same, see Fig. 2.1. The principal plane is commonly chosen as reference. In this reference frame, $U = 0$, and $DoLP$ can also be written as

$$DoLP = -\frac{Q}{I}. \quad (2.4)$$

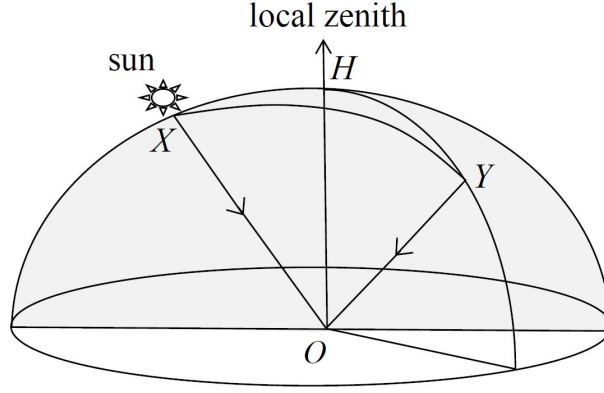


Figure 2.1: Illustration of the reference planes. XO indicates the solar incident direction; OH denotes the local zenith; and YO is the viewing direction. The gray plane XOH is the solar principal plane which contains the directions of the incident sunlight and the local zenith; the plane YOH is the local meridian plane which contains the viewing direction and the local zenith; the plane XOY is the scattering plane which contains the direction of the incident sunlight and the scattered light in the viewing direction.

The Degree of Circular Polarization ($DoCP$) is defined as

$$DoCP = \frac{V}{I}. \quad (2.5)$$

The angle of polarization χ , also known as plane of polarization, the direction of polarization, and the orientation angle (Voss and Liu, 1997; Tilstra et al., 2003; Goldstein, 2003; Hovenier et al., 2004), indicates the angle between the plane of polarization and the plane of reference. It is calculated as

$$\tan 2\chi = \frac{U}{Q}, \quad (2.6)$$

then,

$$\chi = \frac{1}{2} \arctan \frac{U}{Q}; \quad 0 \leq \chi < \pi. \quad (2.7)$$

The ellipticity angle β is defined as

$$\tan 2\beta = \frac{V}{\sqrt{Q^2 + U^2}}; \quad -\pi/4 \leq \beta \leq \pi/4. \quad (2.8)$$

With these polarization parameters, the Stokes vector is expressed as

$$\vec{S} = \begin{pmatrix} I \\ Q \\ U \\ V \end{pmatrix} = I \cdot \begin{pmatrix} 1 \\ DoP \cdot \cos 2\beta \cdot \cos 2\chi \\ DoP \cdot \cos 2\beta \cdot \sin 2\chi \\ DoP \cdot \sin 2\beta \end{pmatrix}. \quad (2.9)$$

As discussed in Chapter 1, skylight polarization in the Earth's atmosphere is commonly described by the parameters related to linear polarization, including the Stokes parameters I , Q , U , the degree of linear polarization, and the angle of polarization. Among them, $DoLP$ and I are independent of the reference plane; while the value of the Stokes parameters Q , U , and AoP change with the choice of different reference planes (Hovenier et al., 2004).

2.1.2 Angle of polarization and signs of Stokes parameters

According to Eq. (2.9), the Stokes parameters Q and U are associated with the angle of polarization χ and the ellipticity angle β :

$$Q = I \cdot DoP \cdot \cos 2\beta \cdot \cos 2\chi, \quad (2.10)$$

$$U = I \cdot DoP \cdot \cos 2\beta \cdot \sin 2\chi, \quad (2.11)$$

where $0 \leq \chi < \pi$ and $-\pi/4 \leq \beta \leq \pi/4$. Since $|\beta| \leq \pi/4$, $\cos 2\beta \geq 0$, and we also have $DoP \geq 0$, then

$$\text{Sign of } (\cos 2\chi) = \text{Sign of } Q. \quad (2.12)$$

Therefore, from different values of χ differing by $\pi/2$ those satisfying both Eq.(2.7) and Eq.(2.12) are chosen (Hovenier et al., 2004). The relationship between the angle of polarization and signs of the Stokes parameters Q and U are listed in Tab. 2.1 and illustrated in Fig. 2.2.

Table 2.1: Ranges of the angle of polarization χ determined by signs of Q and U for the linearly polarized light.

$V = 0$	$Q > 0$	$Q = 0$	$Q < 0$
$U > 0$	$\tan 2\chi > 0,$ $\cos 2\chi > 0,$ $0 < \chi < \pi/4$	$\tan 2\chi$ not exist, $\cos 2\chi = 0,$ $\chi = \pi/4$	$\tan 2\chi < 0,$ $\cos 2\chi < 0,$ $\pi/4 < \chi < \pi/2$
$U = 0$	$\tan 2\chi = 0,$ $\cos 2\chi > 0,$ $\chi = 0$	$\tan 2\chi$ not exist, $\cos 2\chi = 0,$ χ uncertain	$\tan 2\chi = 0,$ $\cos 2\chi < 0,$ $\chi = \pi/2$
$U < 0$	$\tan 2\chi < 0,$ $\cos 2\chi > 0,$ $3\pi/4 < \chi < \pi$	$\tan 2\chi$ not exist, $\cos 2\chi = 0,$ $\chi = 3\pi/4$	$\tan 2\chi > 0,$ $\cos 2\chi < 0,$ $\pi/2 < \chi < 3\pi/4$

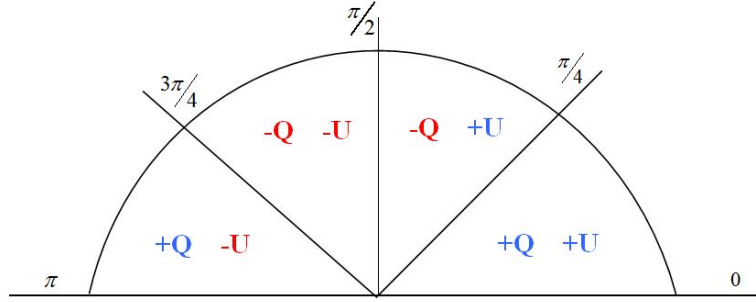


Figure 2.2: Relation between the angle of polarization and signs of Stokes parameters Q and U .

2.1.3 Perpendicular and parallel polarized radiances

The Stokes parameters I and Q are commonly expressed by the polarized components parallel and perpendicular to the reference plane (Liou, 2002):

$$I = I_l + I_r, \quad (2.13)$$

$$Q = I_l - I_r. \quad (2.14)$$

As discussed in Chapter 1, the total radiance of skylight can be regarded as a combination of the unpolarized radiance I_{unp} and the linearly polarized

radiance I_{lin} (omitting the circularly polarization). That is,

$$I = I_{\text{unp}} + I_{\text{lin}}. \quad (2.15)$$

The parallel and perpendicular polarized radiances are written as

$$I_l = (I + Q)/2 = I_{l,\text{unp}} + I_{l,\text{lin}}, \quad (2.16)$$

$$I_r = (I - Q)/2 = I_{r,\text{unp}} + I_{r,\text{lin}}, \quad (2.17)$$

where $I_{l,\text{unp}}$ and $I_{r,\text{unp}}$ denote the parallel and perpendicular components of the unpolarized radiance; while $I_{l,\text{lin}}$ and $I_{r,\text{lin}}$ represent the parallel and perpendicular components of the linearly polarized radiance, respectively.

Past research has shown that, unlike the polarized portion of the Rayleigh scattering, which is polarized perpendicular to the scattering plane, the polarized components of the Mie scattering from atmospheric aerosol particles can be polarized either parallel or perpendicular to the scattering plane, see Chapter 1 (Pust and Shaw, 2008). I_l and I_r provide measurements highly sensitive to aerosol properties. Compared with the total radiance I , they have an enhanced potential for atmospheric aerosol remote sensing.

With the parallel and perpendicular polarized radiances, the linear depolarization ratio ρ is derived by

$$\rho = \frac{I_r}{I_l} = \frac{I - Q}{I + Q}. \quad (2.18)$$

There have been numerous studies on depolarization of linearly polarized light in the backscattering direction (i.e., at the scattering angle of 180°) for Lidar measurements. However, research on depolarization properties of the scattered light at other scattering angles have not extensively been studied in the past although they offer new prospectives for understanding atmospheric aerosol particles (Sun et al., 2012, 2013). For aerosol particles with different shape and size, the depolarization ratios of scattered light reveal different features at different scattering angles (Sun et al., 2013). The depolarization ratio derived from the sun/sky radiometer measurements will also be discussed in the following chapters.

2.2 Interaction of polarized light with atmospheric particles

2.2.1 Scattering theory

Polarization of light is caused by interactions (including scattering and absorption processes) with optical elements (e.g., polarizer, retarder, reflector, and scatterer) (Kokhanovsky, 2003). Air molecules, aerosol particles, and cloud droplets in the atmosphere all can be considered as optical elements. The interaction of electromagnetic radiation with a single particle is described by the following equation (Wendisch and Yang, 2012):

$$\vec{E}' = \frac{e^{-ikR+ikz}}{ikR} \cdot \mathbf{A}(\vartheta) \cdot \vec{E} \quad (2.19)$$

where \vec{E} is the electric field vector of the incident electromagnetic wave and \vec{E}' is the electric field vector of the wave after the interaction. $\mathbf{A}(\vartheta)$ is the complex scattering matrix (also called the complex amplitude scattering matrix). $k = 2\pi/\lambda$ is wavenumber. λ is wavelength. z is the coordinate in the direction of the incoming wave. R is the radial distance from the scattering particle. ϑ is scattering angle that is defined as the angle between the incident and scattering directions. It is calculated by

$$\cos\vartheta = \sin\theta \cdot \sin\theta' \cdot \cos(\varphi - \varphi') + \cos\theta \cdot \cos\theta', \quad (2.20)$$

where θ and φ are the zenith and azimuthal angles of the incident light; while θ' and φ' are the zenith and azimuthal angles of the scattered light.

All information on single scattering properties of the particle are included in the complex scattering matrix $\mathbf{A}(\vartheta)$ (Wendisch and Yang, 2012). The main task of scattering theory is to find elements of $\mathbf{A}(\vartheta)$ for particles with different microphysical properties and chemical compositions.

For a nonspherical particle, the complex scattering matrix $\mathbf{A}(\vartheta)$ has four nonzero elements. That is,

$$\mathbf{A}(\vartheta) = \begin{bmatrix} A_{11}(\vartheta) & A_{12}(\vartheta) \\ A_{21}(\vartheta) & A_{22}(\vartheta) \end{bmatrix}. \quad (2.21)$$

For a sphere, the elements $A_{12} = A_{21} = 0$, then

$$\mathbf{A}(\vartheta) = \begin{bmatrix} A_{11}(\vartheta) & 0 \\ 0 & A_{22}(\vartheta) \end{bmatrix}. \quad (2.22)$$

The nonzero elements of $\mathbf{A}(\vartheta)$ are commonly obtained by solving Maxwell's equations when the radius r , the complex refractive index m , and shape of the particle are known (Zdunkowski et al., 2007).

Elements of the complex scattering matrix $\mathbf{A}(\vartheta)$ are complex scattering amplitudes, which are difficult to measure. Instead of using complex quantities, a 4×4 real scattering matrix $\mathbf{F}(\vartheta)$ (also called Mueller matrix) alternatively describes the relation between “incident” (before interaction with the optical element) and “scattered” (after interaction with the optical element) Stokes vectors. Likewise, interaction of light of arbitrary polarization and a single particle is described by the Stokes vectors and the scattering matrix as follow:

$$\vec{S}' = \frac{1}{k^2 R^2} \cdot \mathbf{F}(\vartheta) \cdot \vec{S}, \quad (2.23)$$

where \vec{S} is the Stokes vector of the incident light, and \vec{S}' is the Stokes vector of the light after the interaction event. $\mathbf{F}(\vartheta)$ is the scattering matrix, which is defined with respect to the scattering plane that holds directions of incident and scattering light (Kokhanovsky, 2006; Wendisch and Yang, 2012).

For a nonspherical particle, the scattering matrix $\mathbf{F}(\vartheta)$ has 16 nonzero elements (omitting the argument ϑ). That is

$$\mathbf{F}(\vartheta) = \begin{bmatrix} F_{11} & F_{12} & F_{13} & F_{14} \\ F_{21} & F_{22} & F_{23} & F_{24} \\ F_{31} & F_{32} & F_{33} & F_{34} \\ F_{41} & F_{42} & F_{43} & F_{44} \end{bmatrix}. \quad (2.24)$$

For randomly-oriented nonspherical particle with a plane of symmetry,

the scattering matrix $\mathbf{F}(\vartheta)$ has the following 6 nonzero elements:

$$\mathbf{F}(\vartheta) = \begin{bmatrix} F_{11} & F_{12} & 0 & 0 \\ F_{12} & F_{22} & 0 & 0 \\ 0 & 0 & F_{33} & F_{34} \\ 0 & 0 & -F_{34} & F_{44} \end{bmatrix}. \quad (2.25)$$

For a homogeneous or radially inhomogeneous spherical particle (as particle of higher symmetry), $F_{11} = F_{22}$, and $F_{33} = F_{44}$. Then the scattering matrix $\mathbf{F}(\vartheta)$ has only 4 nonzero elements:

$$\mathbf{F}(\vartheta) = \begin{bmatrix} F_{11} & F_{12} & 0 & 0 \\ F_{12} & F_{11} & 0 & 0 \\ 0 & 0 & F_{33} & F_{34} \\ 0 & 0 & -F_{34} & F_{33} \end{bmatrix}. \quad (2.26)$$

The nonzero elements of the scattering matrix $\mathbf{F}(\vartheta)$ are determined by the complex scattering matrix $\mathbf{A}(\vartheta)$ (De Rooij and Van der Stap, 1984):

$$F_{11} = F_{22} = \frac{1}{2}(A_{11} \cdot A_{11}^* + A_{22} \cdot A_{22}^*), \quad (2.27)$$

$$F_{33} = F_{44} = \frac{1}{2}(A_{11} \cdot A_{22}^* + A_{22} \cdot A_{11}^*), \quad (2.28)$$

$$F_{12} = -\frac{1}{2}(A_{11} \cdot A_{11}^* - A_{22} \cdot A_{22}^*), \quad (2.29)$$

$$F_{34} = \frac{i}{2}(A_{11} \cdot A_{22}^* - A_{22} \cdot A_{11}^*), \quad (2.30)$$

where A_{11} and A_{22} are complex scattering amplitudes in complex scattering matrix.

Then, polarization of the scattered light can be expressed as:

(A) for Rayleigh scattering by a very small spherical particle (such as visible light scattered by air molecules in the atmosphere):

As an approximation of spherical particle scattering, the Rayleigh scattering matrix for the spherical particle with particle size much smaller than

the incident wavelength is given by (Wendisch and Yang, 2012)

$$\mathbf{F}_{\text{Rayl}}(\vartheta) = \alpha^6 \cdot \left| \frac{m^2 - 1}{m^2 + 2} \right|^2 \times \begin{bmatrix} +(1 + \cos^2 \vartheta)/2 & -(1 - \cos^2 \vartheta)/2 & 0 & 0 \\ -(1 - \cos^2 \vartheta)/2 & +(1 + \cos^2 \vartheta)/2 & 0 & 0 \\ 0 & 0 & \cos \vartheta & 0 \\ 0 & 0 & 0 & \cos \vartheta \end{bmatrix}, \quad (2.31)$$

where $\alpha = 2\pi \cdot r / \lambda$ indicates the size parameter; the complex refractive index $m = m_r + i \cdot m_i$, and m_r is the real part and m_i is the imaginary part.

If the incident radiation is unpolarized, we have

$$\begin{pmatrix} I' \\ Q' \\ U' \\ V' \end{pmatrix} = \alpha^6 \cdot \left| \frac{m^2 - 1}{m^2 + 2} \right|^2 \times \begin{bmatrix} +(1 + \cos^2 \vartheta)/2 & -(1 - \cos^2 \vartheta)/2 & 0 & 0 \\ -(1 - \cos^2 \vartheta)/2 & +(1 + \cos^2 \vartheta)/2 & 0 & 0 \\ 0 & 0 & \cos \vartheta & 0 \\ 0 & 0 & 0 & \cos \vartheta \end{bmatrix} \begin{pmatrix} I \\ 0 \\ 0 \\ 0 \end{pmatrix}, \quad (2.32)$$

then,

$$DoLP = \frac{1 - \cos^2 \vartheta}{1 + \cos^2 \vartheta}, \quad (2.33)$$

$$I'_r = \frac{1}{2} \alpha^6 \cdot \left| \frac{m^2 - 1}{m^2 + 2} \right|^2 \cdot I, \quad (2.34)$$

$$I'_l = \frac{1}{2} \alpha^6 \cdot \left| \frac{m^2 - 1}{m^2 + 2} \right|^2 \cdot \cos^2 \vartheta \cdot I. \quad (2.35)$$

The perpendicular polarized radiance for Rayleigh scattered light I'_r is constant for different scattering angles; while the parallel polarized radiance I'_l is a function of the scattering angle ϑ and $0 \leq I'_l \leq I'_r$. There are three possible situations:

i) in the forward and backward direction ($\vartheta = 0^\circ$ or 180°), $I'_l = I'_r$, the scattered light is unpolarized;

ii) in the direction normal to the scattering plane ($\vartheta = 90^\circ$), $I'_l = 0$, the scattered light is perpendicular polarized;

iii) in other scattering directions, $I'_l < I'_r$, the scattered light is partially polarized. In this situation:

$$I' = I'_{\text{unp}} + I'_{\text{lin}} = I'_{l,\text{unp}} + I'_{r,\text{unp}} + I'_{l,\text{lin}} + I'_{r,\text{lin}}, \quad (2.36)$$

where

$$I'_{\text{unp}} = I'_{l,\text{unp}} + I'_{r,\text{unp}} = I \cdot (1 - \text{DoLP}) = \cos^2 \vartheta \cdot I, \quad (2.37)$$

and

$$I'_{l,\text{unp}} = I'_{r,\text{unp}}. \quad (2.38)$$

Then,

$$I'_{l,\text{unp}} = I'_{r,\text{unp}} = (\cos^2 \vartheta / 2) \cdot I, \quad (2.39)$$

and we can get

$$I'_{r,\text{lin}} = I'_r - I'_{r,\text{unp}} = (1 - \cos^2 \vartheta) / 2 \cdot I, \quad (2.40)$$

$$I'_{l,\text{lin}} = I'_l - I'_{l,\text{unp}} = 0. \quad (2.41)$$

In other words, the polarized portion of the Rayleigh scattered components is always polarized perpendicular to the scattering plane (Pomozi et al., 2001; Pust and Shaw, 2008).

If the incident radiation is perpendicular linearly polarized, we have

$$\begin{pmatrix} I' \\ Q' \\ U' \\ V' \end{pmatrix} = \alpha^6 \cdot \left| \frac{m^2 - 1}{m^2 + 2} \right|^2 \times \begin{bmatrix} +(1 + \cos^2 \vartheta) / 2 & -(1 - \cos^2 \vartheta) / 2 & 0 & 0 \\ -(1 - \cos^2 \vartheta) / 2 & +(1 + \cos^2 \vartheta) / 2 & 0 & 0 \\ 0 & 0 & \cos \vartheta & 0 \\ 0 & 0 & 0 & \cos \vartheta \end{bmatrix} \begin{pmatrix} I \\ -I \\ 0 \\ 0 \end{pmatrix}, \quad (2.42)$$

then,

$$DoLP = 1, \quad (2.43)$$

$$I'_r = \alpha^6 \cdot \left| \frac{m^2 - 1}{m^2 + 2} \right|^2 \cdot I, \quad (2.44)$$

$$I'_l = 0. \quad (2.45)$$

Rayleigh scattering does not change the polarization state. The scattered light is also linearly polarized perpendicular to the scattering plane.

If the incident radiation is parallel linearly polarized, we have

$$\begin{pmatrix} I' \\ Q' \\ U' \\ V' \end{pmatrix} = \alpha^6 \cdot \left| \frac{m^2 - 1}{m^2 + 2} \right|^2 \times \begin{bmatrix} +(1 + \cos^2 \vartheta)/2 & -(1 - \cos^2 \vartheta)/2 & 0 & 0 \\ -(1 - \cos^2 \vartheta)/2 & +(1 + \cos^2 \vartheta)/2 & 0 & 0 \\ 0 & 0 & \cos \vartheta & 0 \\ 0 & 0 & 0 & \cos \vartheta \end{bmatrix} \begin{pmatrix} I \\ I \\ 0 \\ 0 \end{pmatrix}, \quad (2.46)$$

then,

$$DoLP = 1, \quad (2.47)$$

$$I'_r = 0, \quad (2.48)$$

$$I'_l = \alpha^6 \cdot \left| \frac{m^2 - 1}{m^2 + 2} \right|^2 \cdot \cos^2 \vartheta \cdot I. \quad (2.49)$$

Rayleigh scattering does not change the polarization state in this case. The scattered light is linearly polarized parallel to the scattering plane.

(B) for spherical particle scattering (such as visible light scattered by the spherical aerosol and cloud particles in the atmosphere):

If the incident radiation is unpolarized, we have

$$\begin{pmatrix} I' \\ Q' \\ U' \\ V' \end{pmatrix} = \frac{1}{k^2 R^2} \cdot \begin{bmatrix} F_{11} & F_{12} & 0 & 0 \\ F_{12} & F_{11} & 0 & 0 \\ 0 & 0 & F_{33} & F_{34} \\ 0 & 0 & -F_{34} & F_{33} \end{bmatrix} \begin{pmatrix} I \\ 0 \\ 0 \\ 0 \end{pmatrix}, \quad (2.50)$$

then,

$$DoLP = -\frac{F_{12}}{F_{11}}, \quad (2.51)$$

$$I'_r = \frac{F_{11} - F_{12}}{2k^2 R^2} \cdot I, \quad (2.52)$$

$$I'_l = \frac{F_{11} + F_{12}}{2k^2 R^2} \cdot I. \quad (2.53)$$

The scattered light is partly polarized light, containing both perpendicular and parallel polarized components. The perpendicular polarized radiance I'_r could be either larger or less than the parallel polarized radiance I'_l , depending upon the particle properties and the scattering angles.

If the incident radiation is perpendicular linearly polarized , we have

$$\begin{pmatrix} I' \\ Q' \\ U' \\ V' \end{pmatrix} = \frac{1}{k^2 R^2} \cdot \begin{bmatrix} F_{11} & F_{12} & 0 & 0 \\ F_{12} & F_{11} & 0 & 0 \\ 0 & 0 & F_{33} & F_{34} \\ 0 & 0 & -F_{34} & F_{33} \end{bmatrix} \begin{pmatrix} I \\ -I \\ 0 \\ 0 \end{pmatrix}, \quad (2.54)$$

then,

$$DoLP = 1, \quad (2.55)$$

$$I'_r = \frac{F_{11} - F_{12}}{k^2 R^2} \cdot I, \quad (2.56)$$

$$I'_l = 0. \quad (2.57)$$

If the incident radiation is parallel linearly polarized , we have

$$\begin{pmatrix} I' \\ Q' \\ U' \\ V' \end{pmatrix} = \frac{1}{k^2 R^2} \cdot \begin{bmatrix} F_{11} & F_{12} & 0 & 0 \\ F_{12} & F_{11} & 0 & 0 \\ 0 & 0 & F_{33} & F_{34} \\ 0 & 0 & -F_{34} & F_{33} \end{bmatrix} \begin{pmatrix} I \\ I \\ 0 \\ 0 \end{pmatrix}, \quad (2.58)$$

then,

$$DoLP = 1, \quad (2.59)$$

$$I'_r = 0, \quad (2.60)$$

$$I'_l = \frac{F_{11} + F_{12}}{k^2 R^2} \cdot I. \quad (2.61)$$

The light scattered by a spherical particle does not change the polarization state when the incident radiation is linearly polarized (either perpendicular or parallel). In these two situations, the scattered light is also linearly polarized and has the same polarization direction as the incident light (i.e., perpendicular or parallel to the scattering plane) (Kobayashi et al., 2014).

(C) for nonspherical particle scattering (such as visible light scattered by the randomly-oriented nonspherical aerosol or cloud particles with a plane of symmetry in the atmosphere):

If the incident radiation is unpolarized, we have

$$\begin{pmatrix} I' \\ Q' \\ U' \\ V' \end{pmatrix} = \frac{1}{k^2 R^2} \cdot \begin{bmatrix} F_{11} & F_{12} & 0 & 0 \\ F_{12} & F_{22} & 0 & 0 \\ 0 & 0 & F_{33} & F_{34} \\ 0 & 0 & -F_{34} & F_{44} \end{bmatrix} \begin{pmatrix} I \\ 0 \\ 0 \\ 0 \end{pmatrix}, \quad (2.62)$$

then,

$$DoLP = -\frac{F_{12}}{F_{11}}, \quad (2.63)$$

$$I'_r = \frac{F_{11} - F_{12}}{2k^2 R^2} \cdot I, \quad (2.64)$$

$$I'_l = \frac{F_{11} + F_{12}}{2k^2 R^2} \cdot I. \quad (2.65)$$

The $DoLP$, I'_r , and I'_l for nonspherical particle scattering with unpolarized incident radiation are described by the same expressions as those of spherical particles. However, the elements F_{11} and F_{12} are different between these two cases. The light scattered by nonspherical particle is partly polarized, containing both perpendicular and parallel polarized components. The relative values of I'_r and I'_l also depend on different particle properties and scattering angles.

If the incident radiation is perpendicular linearly polarized, we have

$$\begin{pmatrix} I' \\ Q' \\ U' \\ V' \end{pmatrix} = \frac{1}{k^2 R^2} \cdot \begin{bmatrix} F_{11} & F_{12} & 0 & 0 \\ F_{12} & F_{22} & 0 & 0 \\ 0 & 0 & F_{33} & F_{34} \\ 0 & 0 & -F_{34} & F_{44} \end{bmatrix} \begin{pmatrix} I \\ -I \\ 0 \\ 0 \end{pmatrix}, \quad (2.66)$$

then,

$$DoLP = \frac{F_{22} - F_{12}}{F_{11} - F_{12}}, \quad (2.67)$$

$$I'_r = \frac{F_{11} - 2F_{12} + F_{22}}{2k^2 R^2} \cdot I, \quad (2.68)$$

$$I'_l = \frac{F_{11} - F_{22}}{2k^2 R^2} \cdot I. \quad (2.69)$$

If the incident radiation is parallel linearly polarized, we have

$$\begin{pmatrix} I' \\ Q' \\ U' \\ V' \end{pmatrix} = \frac{1}{k^2 R^2} \cdot \begin{bmatrix} F_{11} & F_{12} & 0 & 0 \\ F_{12} & F_{22} & 0 & 0 \\ 0 & 0 & F_{33} & F_{34} \\ 0 & 0 & -F_{34} & F_{44} \end{bmatrix} \begin{pmatrix} I \\ I \\ 0 \\ 0 \end{pmatrix}, \quad (2.70)$$

then,

$$DoLP = \frac{F_{22} + F_{12}}{F_{11} + F_{12}}, \quad (2.71)$$

$$I'_r = \frac{F_{11} - F_{22}}{2k^2 R^2} \cdot I, \quad (2.72)$$

$$I'_l = \frac{F_{11} + 2F_{12} + F_{22}}{2k^2 R^2} \cdot I. \quad (2.73)$$

Unlike spherical particles, nonspherical particles scatter linearly polarized (either perpendicular or parallel) incident radiation and generate partly polarized scattered light, resulting in a decrease in the incident polarization and an increase in polarization perpendicular to the original polarization (Kobayashi et al., 2014).

As a special case, when considering only the total radiance of the scattered light, we have the expression similar to Eq. (2.23) (Wendisch and Yang, 2012):

$$I' = \frac{1}{k^2 R^2} \cdot f(\vartheta) \cdot I, \quad (2.74)$$

where $f(\vartheta) = F_{11}(\vartheta)$ is the scattering function (i.e., the first element of the scattering matrix, dimensionless). It describes the angular distribution of scattered EM radiation in scalar radiative transfer equation with unpolarized incident light.

2.2.2 Single scattering codes

The scattering matrix $\mathbf{F}(\vartheta)$ or the scattering function $f(\vartheta)$ are obtained from single scattering calculations by a number of scattering codes. In this thesis, a Mie code and a T -matrix code¹ are employed to calculate the single scattering properties of spheres and nonspherical particles. The Mie code is used to compute far-field light scattering by polydisperse homogeneous spherical particles using the Lorenz-Mie theory, while the T -matrix code is applied in calculation of light scattering by polydisperse, randomly oriented particles of identical axially symmetric shape, for example, spheroids, finite circular cylinders, and even-order Chebyshev particles (Mishchenko and Travis, 1998).

Previous studies have shown that the scattering matrix or scattering function of natural nonspherical aerosol particles, such as mineral dust, can be adequately modeled by using a shape distribution of spheroids although natural dust particles are more complex, not perfect spheroids (Nousiainen et al., 2011; Sun et al., 2012). Thus, only spheroids with different aspect ratios (i.e., the ratios of the horizontal to rotational axes) are considered in single scattering calculation in this study.

To calculate scattering by randomly oriented spheroids with different size and shape distributions, a software package has been employed, integrating spheroid kernel look-up tables simulated for 25 shape bins of the spheroid aspect ratios ranging from ~ 0.3 to ~ 3.0 and for 22 logarithmically equidistant bins in the range of sizes from 0.05 to 15 μm (Dubovik et al., 2006). Compared with the Mie and the T -matrix codes, it makes simulation of mixture of spheroids more fast and flexible, especially for the mixture of different

¹See http://www.giss.nasa.gov/staff/mmishchenko/t_matrix.html, accessed April 2012.

particle shapes.

The microphysical parameters of aerosol particles (including the particle radius, size distribution, real and imaginary parts of the complex refractive index for specific wavelength, as well as shape parameters and shape distributions for nonspherical particles) constitute the input of the single scattering codes. After scattering calculation, the optical parameters (containing the extinction, scattering, and absorption cross sections C_{ext} , C_{sca} , and C_{abs} , the single scattering albedo ϖ , the elements of scattering matrix, the expansion coefficients of the elements of the scattering matrix, and asymmetry factor g) are obtained, see Fig. 2.3.

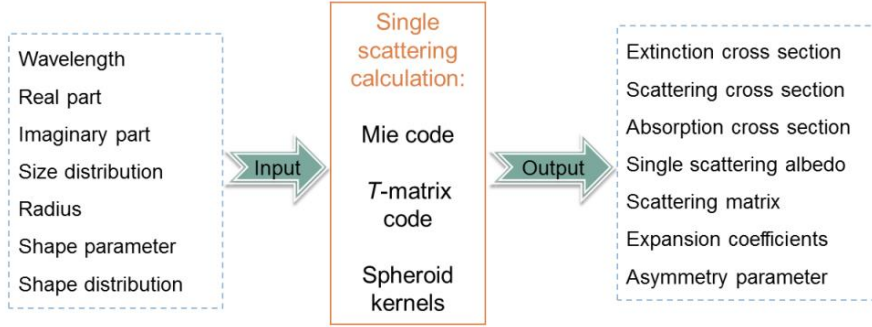


Figure 2.3: Input microphysical parameters and output optical parameters of the single scattering calculation.

To further compute the Stokes vector of the scattered electromagnetic wave in radiative transfer model involving multiple scattering, the following quantities need to be calculated: the Stokes vector of the incident light with respect to the scattering plane; the product of the Stokes vector of the incident radiation and the scattering matrix, from which the Stokes vector of the scattered light with respect to the scattering plane is obtained; and the Stokes vector of the scattered light with respect to its meridian plane through transforming from scattering matrix to phase matrix (Mishchenko et al., 2002).

2.2.3 Optical parameters

The optical properties of particles which interact with incident light are described by the following optical parameters:

(A) optical depth

The optical cross sections (including extinction, scattering, and absorption cross sections) are measurements of how effective an individual particle interacts with incident EM radiation in extinction, scattering and absorption processes, respectively. They are given by (De Rooij and Van der Stap, 1984; Wendisch and Yang, 2012)

$$C_{\text{ext}} = \frac{\phi_{\text{ext}}}{F_{\text{inc}}}, \quad C_{\text{sca}} = \frac{\phi_{\text{sca}}}{F_{\text{inc}}}, \quad C_{\text{abs}} = \frac{\phi_{\text{abs}}}{F_{\text{inc}}}, \quad (2.75)$$

where $C_{\text{ext}} = C_{\text{sca}} + C_{\text{abs}}$. C_{ext} , C_{sca} , and C_{abs} are extinction, scattering and absorption cross sections (in units of m^2). ϕ_{ext} , ϕ_{sca} , and ϕ_{abs} are extinction, scattering, and absorption radiant energy fluxes (in units of W). F_{inc} is the incident radiant flux density or irradiance (in units of W m^{-2}). With the definition of scattering function $f(\vartheta)$ in Subsection 2.2.1, the scattering cross section C_{sca} is expressed as (Wendisch and Yang, 2012):

$$C_{\text{sca}} = \frac{1}{k^2} \iint_{4\pi} f(\vartheta) d^2\Omega, \quad (2.76)$$

where the differential solid angle $d^2\Omega = \sin\theta d\theta d\varphi$. θ and φ are the zenith and azimuthal angles, respectively.

When normalizing the optical cross sections with the geometric cross section of particle, the efficiency factors are obtained:

$$Q_{\text{ext}} = \frac{C_{\text{ext}}}{A_{\text{proj}}}, \quad Q_{\text{sca}} = \frac{C_{\text{sca}}}{A_{\text{proj}}}, \quad Q_{\text{abs}} = \frac{C_{\text{abs}}}{A_{\text{proj}}}, \quad (2.77)$$

where Q_{ext} , Q_{sca} , and Q_{abs} are extinction, scattering and absorption efficiency factors (dimensionless). A_{proj} is the geometric cross section of the particle projected onto a plane perpendicular to the incident direction with $A_{\text{proj}} = \pi \cdot r^2$ for spherical particles (Wendisch and Yang, 2012).

If an ensemble of particles with different size, chemical compositions and shapes is contained within a volume (that is defined such that no multiple interactions between the EM radiation and particles occurs), the volumetric extinction, scattering, and absorption coefficients are derived by size distribution-weighted averaging of the single scattering optical properties of individual particles. They are calculated by (Wendisch and Yang, 2012)

$$\langle b_{\text{ext}}(\lambda) \rangle = \int_0^\infty C_{\text{ext}}(\lambda, r') \cdot \frac{dN}{d \ln r}(r') d \ln r', \quad (2.78)$$

$$\langle b_{\text{sca}}(\lambda) \rangle = \int_0^\infty C_{\text{sca}}(\lambda, r') \cdot \frac{dN}{d \ln r}(r') d \ln r', \quad (2.79)$$

$$\langle b_{\text{abs}}(\lambda) \rangle = \langle b_{\text{ext}} \rangle - \langle b_{\text{sca}} \rangle = \int_0^\infty C_{\text{abs}}(\lambda, r') \cdot \frac{dN}{d \ln r}(r') d \ln r', \quad (2.80)$$

where b_{ext} , b_{sca} , and b_{abs} are extinction, scattering, and absorption coefficients (in units of m^{-1}). The symbol $\langle \dots \rangle$ denotes the volumetric optical properties averaging over individual particles. $dN/d \ln r$ is the number size distribution of particles with N representing particle number and r indicating particle radius. Considering that the optical effects of atmospheric aerosol particles are more closely related to their volume than their number, the particle size distribution is more conveniently described as volume size distribution $dV/d \ln r$ (Schuster et al., 2006). It relates to the distribution of particle number as

$$\frac{dN(r)}{d \ln r} = \frac{3}{4\pi r^3} \frac{dV(r)}{d \ln r}. \quad (2.81)$$

The optical depth, also called the optical thickness, is defined as the integrated extinction coefficient over a vertical column of unit cross section. That is,

$$\tau(\lambda, z) = \int_z^\infty \langle b_{\text{ext}}(\lambda, z') \rangle dz', \quad (2.82)$$

where τ is a function of altitude (dimensionless). z indicates altitude above ground. At the TOA, $z \rightarrow \infty$, and $\tau \rightarrow 0$ (Wendisch and Yang, 2012).

For atmospheric aerosol particles, the bimodal lognormal distribution is usually employed to approximately describe real polydisperse aerosol particle

size distribution (Schuster et al., 2006; Dubovik et al., 2006; Li et al., 2006). That is,

$$\frac{dV(r)}{d \ln r} = \sum_{i=1}^2 \frac{C_{V,i}}{\sqrt{2\pi}\sigma_i} \exp\left[-\frac{(\ln r - \ln r_{V,i})^2}{2\sigma_i^2}\right], \quad (2.83)$$

where $C_{V,i}$ represents the particle volume concentration; $r_{V,i}$ is the volume median radius; and σ_i denotes the standard deviation. These parameters are retrieved by the AERosol RObotic NETwork (AERONET) for total, fine, and coarse aerosol modes, separately. The AERONET retrievals also provide discrete volume size distribution in 22 logarithmically equidistant bins in the range of particle sizes $0.05 \mu\text{m} \leq r \leq 15 \mu\text{m}$. That matches with input of the spheroid kernels software package, see Subsection 2.2.2.

(B) single scattering albedo

The Single Scattering Albedo (SSA) quantifies the percentage of light being scattered. It represents the ratio of the scattering and extinction cross sections, the ratio of the scattering and extinction efficiency factors, or the ratio of scattering and extinction coefficients, that is

$$\varpi = \frac{C_{\text{sca}}}{C_{\text{ext}}} = \frac{Q_{\text{sca}}}{Q_{\text{ext}}} = \frac{\langle b_{\text{sca}} \rangle}{\langle b_{\text{ext}} \rangle}, 0 \leq \varpi \leq 1. \quad (2.84)$$

The SSA relates to imaginary part of the complex refractive index and indicates the strength of absorption for aerosol particles. The stronger the absorption, the smaller ϖ and the larger the imaginary part of refractive index and vice versa. In the extreme case of total scattering and no absorption, $\varpi = 1$; while in the other extreme case of total absorption with no scattering, $\varpi = 0$ (Wendisch and Yang, 2012).

(C) phase matrix and asymmetry factor

The normalized form of the scattering matrix $\mathbf{F}^{\text{nor}}(\vartheta)$ (also called the scattering phase matrix) is commonly adopted in literatures (Liou, 2002; Wendisch and Yang, 2012), with the first element satisfying the following normalization condition:

$$\frac{1}{4\pi} \iint_{4\pi} F_{11}^{\text{nor}}(\vartheta) d^2\Omega = 1. \quad (2.85)$$

According to Eqs. (2.76) and (2.85), we obtain

$$F_{11}^{\text{nor}}(\vartheta) = \frac{4\pi}{k^2 \cdot C_{\text{sca}}} \cdot f(\vartheta). \quad (2.86)$$

Similarly, we have

$$\mathbf{F}^{\text{nor}}(\vartheta) = \frac{4\pi}{k^2 \cdot C_{\text{sca}}} \cdot \mathbf{F}(\vartheta), \quad (2.87)$$

along with Eq. (2.23),

$$\vec{S}' = \frac{C_{\text{sca}}}{4\pi R^2} \cdot \mathbf{F}^{\text{nor}}(\vartheta) \cdot \vec{S}. \quad (2.88)$$

As discussed in Subsection 2.2.1, the scattering matrix is defined with respect to the scattering plane. This plane transforms for different scattering events. Thus, the corresponding coordinate systems describing the incident and the scattered light are also not fixed. In order to represent interactions of light and particles in a uniform reference coordinate system, the scattering matrix should be transformed into the phase matrix that is defined relative to the local meridian plane. For a macroscopically isotropic and mirror-symmetric scattering medium, the phase matrix $\mathbf{P}(\vartheta)$ is calculated from the scattering matrix as (Hovenier and van der Mee, 1988; Liou, 2002; Mishchenko et al., 2002):

$$\mathbf{P}(\vartheta) = \mathbf{P}(\mu, \varphi; \mu', \varphi') = \mathbf{L}(\pi - \sigma_2) \mathbf{F}^{\text{nor}}(\vartheta) \mathbf{L}(-\sigma_1). \quad (2.89)$$

$\mathbf{L}(\sigma)$ is a 4×4 rotation matrix, that is given by

$$\mathbf{L}(\sigma) = \begin{bmatrix} 1 & 0 & 0 & 0 \\ 0 & \cos 2\sigma & \sin 2\sigma & 0 \\ 0 & -\sin 2\sigma & \cos 2\sigma & 0 \\ 0 & 0 & 0 & 1 \end{bmatrix}, \quad (2.90)$$

where the argument $\sigma = \pi - \sigma_2$ or $\sigma = -\sigma_1$. The rotation angle σ_1 is the angle between the scattering and the meridian planes containing the incident

light (θ, φ) ; while the rotation angle σ_2 is the angle between the scattering and the meridian planes containing the scattered light (θ', φ') . $\mu = \cos\theta$, and $\mu' = \cos\theta'$. ϑ is the scattering angle defined above. For randomly-oriented nonspherical particle with a plane of symmetry, the phase matrix is given by

$$\begin{aligned}
 \mathbf{P} &= \begin{bmatrix} P_{11} & P_{12} & P_{13} & P_{14} \\ P_{21} & P_{22} & P_{23} & P_{24} \\ P_{31} & P_{32} & P_{33} & P_{34} \\ P_{41} & P_{42} & P_{43} & P_{44} \end{bmatrix} \\
 &= \begin{bmatrix} 1 & 0 & 0 & 0 \\ 0 & X_2 & -S_2 & 0 \\ 0 & S_2 & X_2 & 0 \\ 0 & 0 & 0 & 1 \end{bmatrix} \cdot \begin{bmatrix} F_{11}^{\text{nor}} & F_{12}^{\text{nor}} & 0 & 0 \\ F_{12}^{\text{nor}} & F_{22}^{\text{nor}} & 0 & 0 \\ 0 & 0 & F_{33}^{\text{nor}} & F_{34}^{\text{nor}} \\ 0 & 0 & -F_{34}^{\text{nor}} & F_{44}^{\text{nor}} \end{bmatrix} \cdot \begin{bmatrix} 1 & 0 & 0 & 0 \\ 0 & X_1 & -S_1 & 0 \\ 0 & S_1 & X_1 & 0 \\ 0 & 0 & 0 & 1 \end{bmatrix} \\
 &= \begin{bmatrix} F_{11}^{\text{nor}} & F_{12}^{\text{nor}} X_1 & -F_{12}^{\text{nor}} S_1 & 0 \\ F_{12}^{\text{nor}} X_2 & X_2 F_{22}^{\text{nor}} X_1 - S_2 F_{33}^{\text{nor}} S_1 & -X_2 F_{22}^{\text{nor}} S_1 - S_2 F_{33}^{\text{nor}} X_1 & -F_{34}^{\text{nor}} S_2 \\ F_{12}^{\text{nor}} S_2 & S_2 F_{22}^{\text{nor}} X_1 + X_2 F_{33}^{\text{nor}} S_1 & -S_2 F_{22}^{\text{nor}} S_1 + X_2 F_{33}^{\text{nor}} X_1 & F_{34}^{\text{nor}} X_2 \\ 0 & -F_{34}^{\text{nor}} S_1 & -F_{34}^{\text{nor}} X_1 & F_{44}^{\text{nor}} \end{bmatrix}, \tag{2.91}
 \end{aligned}$$

where $X_1 = \cos 2\sigma_1$, $X_2 = \cos 2\sigma_2$, $S_1 = \sin 2\sigma_1$, and $S_2 = \sin 2\sigma_2$.

Like the scattering function, $p(\vartheta) = P_{11}(\vartheta)$ is the phase function in scalar radiative transfer equation, also satisfying the following normalization condition:

$$\frac{1}{4\pi} \iint_{4\pi} p(\vartheta) d^2\Omega = \frac{1}{4\pi} \iint_{4\pi} F_{11}^{\text{nor}}(\vartheta) d^2\Omega = 1. \tag{2.92}$$

The asymmetry factor g is an approximate measure of angular distribution of the radiation scattered by an individual particle. It is defined as

$$g = \frac{1}{4\pi} \iint_{4\pi} p(\vartheta) \cdot \cos\vartheta d^2\Omega. \tag{2.93}$$

g is positive for particles which scatter predominantly in the forward direction; negative for backscattering particles; and zero for symmetric phase functions with $p(\pi - \vartheta) = p(\vartheta)$ (Wendisch and Yang, 2012).

2.3 Radiative transfer of polarized light in the atmosphere

2.3.1 Theory of polarized radiative transfer

Light propagating in the atmosphere is discussed in this section. The atmosphere can be considered as an absorbing, emitting, and scattering medium. Interaction of light with a disperse medium of an arbitrary thickness is described in the framework of the radiative transfer theory (Liou, 2002; Kokhanovsky, 2003; Wendisch and Yang, 2012). If only the scalar radiance of the light is considered, radiative transfer in plane-parallel random media is described by the scalar radiative transfer theory. The radiance I of the light changes with propagating distance in disperse media. Variation of the radiance dI is given by the scalar radiative transfer equation (Wendisch and Yang, 2012):

$$\begin{aligned} \mu \frac{dI_\lambda(\tau, \mu, \varphi)}{d\tau} = & I_\lambda(\tau, \mu, \varphi) \\ & - \varpi \cdot \int_0^{2\pi} \int_{-1}^1 \frac{p(\mu', \varphi'; \mu, \varphi)}{4\pi} \cdot I_\lambda(\tau, \mu', \varphi') d\mu' d\varphi' \\ & - \varpi \cdot \frac{p(-\mu_0, \varphi_0; \mu, \varphi)}{4\pi} \cdot F_{0,\lambda} \cdot \exp(-\tau/\mu_0) \\ & - (1 - \varpi) \cdot B_\lambda(T), \end{aligned} \quad (2.94)$$

where ϖ is the single scattering albedo; τ is the optical depth; and p is the phase function, see Subsection 2.2.3. λ represents the wavelength, which indicates that the corresponding variables being spectral measurements. $\mu = \cos\theta$, θ is the zenith angle, and φ is the azimuthal angle. (θ, φ) indicates the direction of the outgoing radiation; $\mu' = \cos\theta'$, and (θ', φ') denotes the direction of the incoming radiation; $\mu_0 = \cos\theta_0$, and $(-\theta_0, \varphi_0)$ indicates the direction of the incident solar beam. The coordinate system is defined that τ increases downward and μ is negative for downward direction. F_0 is the unpolarized solar flux density or irradiance at the TOA. $B_\lambda(T)$ is the

Planck's function. That is given by

$$B_\lambda(T) = \frac{2h \cdot c^2 \cdot \lambda^{-5}}{\exp[h \cdot c / (k_B \cdot \lambda \cdot T)] - 1}, \quad (2.95)$$

where $h = 6.6262 \times 10^{-34}$ J s is the Planck's constant; $k_B = 1.3805 \times 10^{-23}$ J K⁻¹ is the Boltzmann's constant; and $c = 2.997925 \times 10^8$ m s⁻¹ is the speed of light in a vacuum. λ is wavelength. T is absolute temperature.

Taking the polarization characteristics of light into account, scalar radiative transfer equation should be extended to vector radiative transfer equation. Then, the scalar radiance I is substituted by the Stokes vector \vec{S} , and the phase function p is replaced by the phase matrix \mathbf{P} . The plane-parallel vector radiative transfer equation for randomly-oriented particles is written as (Evans and Stephens, 1991; Liou, 2002; Kokhanovsky, 2003)

$$\begin{aligned} \mu \frac{d\vec{S}_\lambda(\tau, \mu, \varphi)}{d\tau} &= \vec{S}_\lambda(\tau, \mu, \varphi) \\ &- \varpi \cdot \int_0^{2\pi} \int_{-1}^1 \frac{\mathbf{P}(\mu', \varphi'; \mu, \varphi)}{4\pi} \cdot \vec{S}_\lambda(\tau, \mu', \varphi') d\mu' d\varphi' \\ &- \varpi \cdot \frac{\mathbf{P}(-\mu_0, \varphi_0; \mu, \varphi)}{4\pi} \cdot \vec{S}_{0,\lambda} \cdot \exp(-\tau/\mu_0) \\ &- (1 - \varpi) \cdot \vec{B}_\lambda(T), \end{aligned} \quad (2.96)$$

where $\vec{S} = (I, Q, U, V)^T$ is the diffuse radiance field expressed as a Stokes vector. $\vec{S}_0 = (F_0, 0, 0, 0)^T$ indicates the solar irradiance Stokes vector, and F_0 is the extraterrestrial solar flux density in the scalar equation. The downward solar radiation \vec{S}_0 is regarded unpolarized at the TOA. $\vec{B}(T) = [B(T), 0, 0, 0]^T$ is the thermal emission Stokes vector, and $B(T)$ also denotes the Planck's function in the scalar equation. \mathbf{P} is the phase matrix to which the following processes contribute: Rayleigh scattering of very small air molecules, spherical particle scattering of atmospheric aerosol and/or cloud particles (e.g., soot, sulfate, sea-salt, and water droplet), nonspherical particle scattering of atmospheric aerosol and/or cloud particles (e.g., dust and ice crystal), and multiple scattering.

Fig. 2.4 illustrates the scattering contributors from scattering path to the ground-based polarimetric radiometer measurements in a clear, cloudless

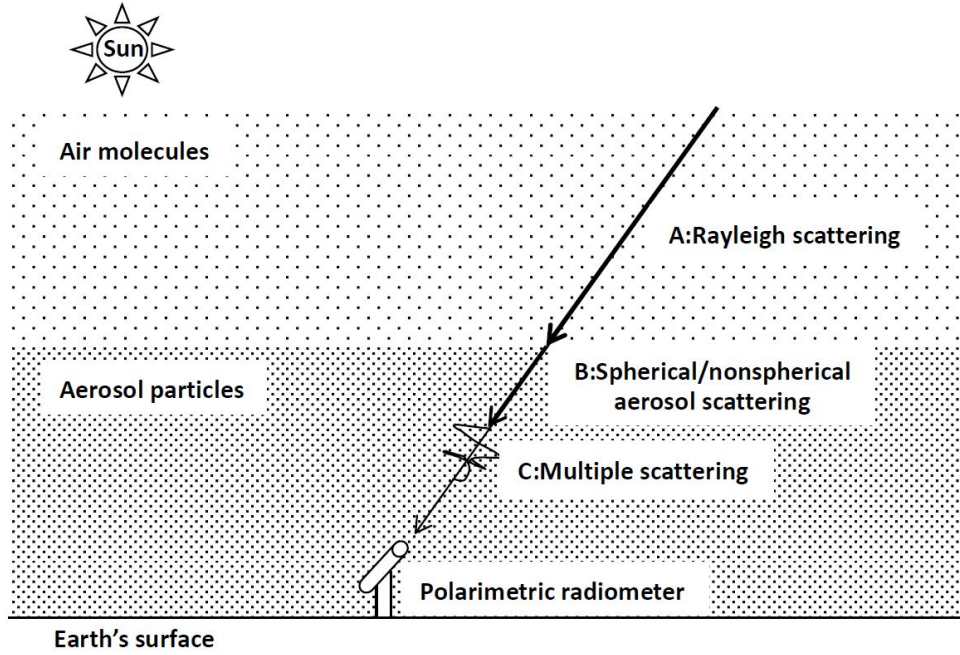


Figure 2.4: Simplified schematic diagram of scattering contributors to the ground-based polarimetric radiometer measurements in a clear, cloudless sky. The plane of the paper is the scattering plane. Redrawn according to Pust and Shaw (2008) with modification.

sky. The direct incident sunlight at the TOA is assumed unpolarized. The polarimetric radiometer on the ground measures the scattered light after a range of interactions of the incident unpolarized light with atmospheric particles (i.e., air molecules, spherical/nonspherical aerosol particles). According to Fig. 2.4 and Subsection 2.2.1, contributors on the scattering path, including Rayleigh scattering, spherical or nonspherical particle single scattering, and multiple scattering, may contribute to the polarization measurements as follow:

First, Rayleigh scattering of the air molecules introduces partly polarized light into the path (denoted A in Fig. 2.4). The scattered light contains an unpolarized component and a polarized component which is always perpendicular to the scattering plane, see Subsection 2.2.1.

Second, single scattering of the spherical or nonspherical aerosol particles occurs in the scattering path (denoted B in Fig. 2.4). The incident light can be unpolarized (i.e., the direct sunlight or the Rayleigh unpolarized component) or the perpendicular linearly polarized (i.e., the Rayleigh polarized component). For unpolarized incident light, scattering by spherical or nonspherical particles generate partly polarized light, and the polarized portions contain both the perpendicular and parallel polarized components. For perpendicular linearly polarized incident light, the spherical particle scattering does not change the polarization state. The scattered light is still perpendicular linearly polarized light with the same degree of linear polarization and angle of polarization as the incident light. However, the nonspherical particle scattering in this situation changes the polarization state, resulting in a decrease in the incident polarization and an increase in polarization perpendicular to the incident polarization. The scattered light is partly polarized light, see Subsection 2.2.1.

Finally, the multiple scattering among aerosol particles and air molecules contributes to the polarized measurements (denoted C in Fig. 2.4). Regarding each single scattering process, the incident light could be unpolarized, perpendicular polarized, or parallel polarized. For unpolarized incident light, scattering by air molecules, spherical or nonspherical aerosol particles generate partially polarized light. The polarized component of the partially polarized scattered light is only perpendicular polarized for air molecules, whereas it could be either perpendicular or parallel polarized at different scattering angles for spherical or nonspherical aerosol particles. For perpendicular or parallel linearly polarized incident light, the air molecular Rayleigh scattering and the spherical particle scattering do not change the polarization state. The scattered light is still perpendicular or parallel linearly polarized light. However, the nonspherical particle scattering may change the polarization state. The scattered light becomes partially polarized, see Subsection 2.2.1. Although the processes of multiple scattering are complicated, the combined effects depolarize the light. That also means a decrease in the original incident polarized component, an increase in polarized component perpendicular to the original polarization, and reduction in the degree of linear polarization.

As a result, the polarization state of skylight measured by ground-based instruments could be unpolarized, polarized perpendicular or parallel to the scattering plane in the following situations, depending upon the relative magnitudes of each unpolarized and polarized components in the processes discussed above (Pust and Shaw, 2008):

i) in clear sky conditions, polarization of skylight is dominated by the Rayleigh scattering ($I_{r,\text{Ray}} > I_{l,\text{Ray}}$, where $I_{r,\text{Ray}}$ and $I_{l,\text{Ray}}$ are the components of radiance of the Rayleigh scattered light perpendicular and parallel to the scattering plane). The polarized component of the Rayleigh scattering is perpendicular to the scattering plane. Then, $AoP = 90^\circ$.

ii) if the polarized component of the spherical or nonspherical aerosol particle scattering is perpendicular to the scattering plane ($I_{r,\text{aer}} > I_{l,\text{aer}}$, where $I_{r,\text{aer}}$ and $I_{l,\text{aer}}$ are the components of radiance of the aerosol scattered light perpendicular and parallel to the scattering plane), along with the Rayleigh scattering ($I_{r,\text{Ray}} > I_{l,\text{Ray}}$), the combined polarized components will still be oriented perpendicular to the scattering plane, and the AoP will be the same as the clear-sky AoP (i.e., $AoP = 90^\circ$).

iii) if the polarized component of the spherical or nonspherical aerosol particle scattering is parallel to the scattering plane ($I_{r,\text{aer}} < I_{l,\text{aer}}$), but smaller than the perpendicular polarized component of the Rayleigh scattering ($|I_{l,\text{aer}} - I_{r,\text{aer}}| < |I_{r,\text{Ray}} - I_{l,\text{Ray}}|$), then the combined polarized components will also be oriented perpendicular to the scattering plane. Then, $AoP = 90^\circ$.

iv) if the polarized component of the spherical or nonspherical aerosol particle scattering is parallel to the scattering plane ($I_{l,\text{aer}} > I_{r,\text{aer}}$), and equals to the perpendicular polarized component of the Rayleigh scattering ($|I_{l,\text{aer}} - I_{r,\text{aer}}| = |I_{r,\text{Ray}} - I_{l,\text{Ray}}|$), then the combined effect generates unpolarized scattered light, and the AoP in this case will be undefined.

v) if the polarized component of the spherical or nonspherical aerosol particle scattering is parallel to the scattering plane ($I_{l,\text{aer}} > I_{r,\text{aer}}$), but larger than the perpendicular polarized component of the Rayleigh scattering

($|I_{l,\text{aer}} - I_{r,\text{aer}}| > |I_{r,\text{Ray}} - I_{l,\text{Ray}}|$), then the combined polarized components will be oriented parallel to the scattering plane, and the *AoP* will be in the direction of 90° from the clear-sky *AoP* (i.e., $AoP = 0^\circ$ or 180°).

The polarization state of actual skylight is calculated by solving the vector radiative transfer equation, in which the Stokes vector is characterized by the optical depth τ , the single scattering albedo ϖ , and the phase matrix \mathbf{P} . These optical parameters of atmospheric particles are determined by their microphysical properties and chemical compositions (e.g., the particle size, size distribution, shape, shape distribution, real and imaginary parts of the complex refractive index, and mixture of different compositions).

2.3.2 Vector radiative transfer models

To analyze the influences of different aerosol microphysical properties on polarized skylight, vector radiative transfer models with a variety of alternative aerosol inputs are employed. In this study, the Successive Order of Scattering (SOS) radiative transfer code and the SCIATRAN radiative transfer software package are applied to simulate the polarized skylight observed by the ground-based multi-spectral multi-angle sun/sky radiometer, and to analyze sensitivities of the observed polarized skylight to different aerosol properties.

The SOS radiative transfer code is developed initially at the Laboratoire d'Optique Atmosphérique (LOA), Université Lille 1 (Deuzé et al., 1989; Lenoble et al., 2007). It simulates polarized radiance of the surface-atmosphere system under cloudless sky and neglecting gaseous absorption. Only scattering processes by air molecules and aerosol particles are considered outside the absorption bands. The Earth's atmosphere is assumed to be plane-parallel, then the concentration profiles of aerosol particles and air molecules are modeled in layers of optical thickness. The properties of particles in the atmosphere vary along the vertical direction (Lenoble et al., 2007; Lafrance and Hagolle, 2010). The SOS method is adopted to solve the vector radiative transfer equation in this code. According to the method of SOS, radiation

is decomposed into the contributions from consecutive orders of scattering events. Convergence of the solution depends on the single scattering albedo and optical depth. Thus, a huge number of computational efforts are required under hazy sky conditions (Lafrance and Hagolle, 2010; Wendisch and Yang, 2012). The input parameters of aerosol particles for SOS code include the aerosol optical depth, real and imaginary parts of the complex refractive index, and the volume particle size distribution expressed as 22 logarithmically equidistant discrete points in the range of sizes $0.05 \mu\text{m} \leq r \leq 15 \mu\text{m}$. These parameters are obtained directly from CE318 inversions. That is particularly convenient for simulation of the sun/sky radiometer measurements in this study. The outputs of Stokes vector \vec{S} at viewing direction (μ, φ) are given in the form of dimensionless normalized radiance $\pi\vec{S}/F_0$, where F_0 is the extraterrestrial solar flux density or irradiance (Lenoble et al., 2007; Lafrance and Hagolle, 2010). The *DoLP* and *AoP* are derived from linearly polarized parameters I , Q , and U based on Eqs.(2.3), (2.7), and (2.12).

The SCIATRAN software package is a typical compositive vector radiative transfer model, which is developed at the Institute of Remote Sensing, University of Bremen (Rozanov et al., 2002; Buchwitz et al., 2004; Rozanov and Kokhanovsky, 2006; Kokhanovsky et al., 2010; Rozanov et al., 2014). It aims at calculating the Stokes parameters of reflected, transmitted, and internal radiations in the Earth's atmosphere from UltraViolet (UV) to thermal infrared spectral regions (i.e., from 175.44 nm to 40 μm). The Discrete Ordinate Method (DOM) is applied to solve the vector radiative transfer equation in SCIATRAN. The SCIATRAN software package is capable of simulating measurements of the scattered radiations for various observation geometries (e.g., nadir, off-nadir, zenith, limb, or off-axis) and for diversified locations of the instruments (e.g., spaceborne, airborne, balloonborne, or ground-based). The atmospheric models in SCIATRAN include trace gases absorption, Rayleigh scattering, absorption and scattering by aerosol and cloud particles. This study mainly concerns atmospheric optics outside the absorption bands and without cloud. The input files controlling aerosol and Rayleigh scattering parameters need to be considered in detail. For Rayleigh scattering, the Rayleigh optical depth is set manually according to accurate

calculation (Bodhaine et al., 1999). For aerosol scattering, there are four kinds of control files, including the LOWTRAN aerosol setup, the SCIA-TRAN database aerosol setup, the WMO database aerosol setup, and the manual aerosol setting. Among them, the WMO and manual aerosol settings can be used in the vector cases only. Compared with the WMO database that contains some predefined aerosol types for different layers, it is more flexible to use the user-defined aerosol parameterization (i.e., the manual aerosol setting) to characterize a variety of aerosol particles. Expansion coefficients of the scattering matrix, which are the output of the Mie and T -matrix single scattering codes introduced in Subsection 2.2.2, are directly used as input for the SCIATRAN model as manual aerosol setting. However, for the spheroid kernels, it has to calculate the expansion coefficients of scattering matrix and then put them into the SCIATRAN model.

The SOS radiative transfer code is convenient for input of the CE318 derived aerosol parameters, including the aerosol optical depth, real and imaginary parts of the complex refractive index, and the discrete form of the volume particle size distribution. Therefore, in this study the SOS code is applied to simulate polarized skylight measurements of the ground-based CE318-DP in different observation geometries and to validate the results of the Stokes parameters I , Q , U , $DoLP$, and AoP calculated from the CE318-DP measurements. The SCIATRAN radiative transfer software package is easy to use together with the Mie and T -matrix single scattering codes, as well as the spheroid kernels. The outputs of optical parameters and expansion coefficients of the scattering matrix from the single scattering codes are linked to the SCIATRAN manual aerosol setting. Thus, it is flexible to utilize the SCIATRAN software package to simulate the sensitivities of polarization parameters of skylight to different aerosol properties.

Chapter 3

Measurement of skylight polarization

3.1 Instrument description

The ground-based polarimetric instrument used to measure skylight polarization in this study is the CIMEL Dual-Polar sun/sky radiometer (CE318-DP). Similar to the design of other CE318 radiometers, the CE318-DP consists of three main parts: the optical sensor head, the automated mount, and the electronic box, see Fig. 3.1.

The optical sensor head is the unit for measuring radiance. It is equipped with two rotating wheels assembling nine filters (no polarization detection in 936 nm channel) and nine polarizers, respectively. The linear polarization parameters of skylight (including the Stokes vector components I , Q , and U , $DoLP$, and AoP) in principle can be determined from three radiance measurements by using a rotating linear polarizer in front of a rotating filter. The nine polarizers work as the key polarization measuring elements. As depicted schematically in Fig. 3.2, they are fixed on the polarizers' wheel. The nine polarizers constitute three sets of triplets. Each triplet consists of three polarizers maintaining the same polarization orientations, see the double-headed arrows in Fig. 3.2. The adjacent polarizers on the wheel

3 Measurement of skylight polarization



Figure 3.1: The new ground-based CIMEL Dual-Polar sun/sky radiometer (left: CE318-DP#962; top-right: the optical sensor head fixed on the automated mount; bottom-right: the electronic box).

keep 40° from each other. Thus, the polarizers from the same set of triplets maintain an interval of 120° . For example, the polarizers P1, P2, and P3 belong to a set of triplet. The wheel rotates 120° from P1 to P2, and then from P2 to P3 for a group of polarization observations at each wavelength, see Fig. 3.2. Hence the orientations of the transmittance axes of three polarizers within one set of triplet maintain 60° from each other (e.g., 0° , 60° , and 120°).

By combining rotations of the polarizers' and the filters' wheels, the CE318-DP has polarization observation capability in eight channels with center wavelengths at 340, 380, 440, 500, 675, 870, 1020, and 1640 nm, see Tab. 3.1. Among them, the latter six bands are utilized frequently, whereas measurements at 340 and 380 nm are not commonly used because of difficulties in absolute calibration of the polarized radiances. For CE318-DP, some

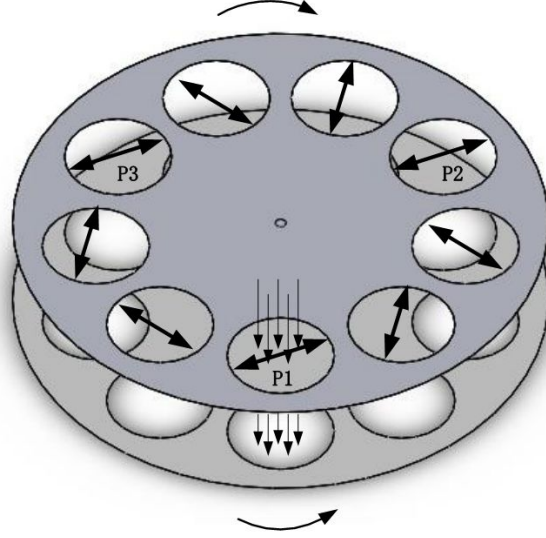


Figure 3.2: Schematic diagram of mechanism of the Dual-Polar sun/sky radiometer. Upper layer represents the polarizers' wheel and lower layer is the filters' wheel. The downward rays indicate incidence of the radiation. The double-headed arrows indicate the orientations of polarizers' transmittance axes. With rotations of these two wheels and combinations of different polarizers and filters, the CE318-DP conducts multi-wavelength polarization measurements. Drawn originally by Kaitao Li with modification.

wavelength channels share the same set of polarizer triplets. For example, CE318-DP labeled #954, #962, and #969 with 340 and 380 nm; 440, 500, and 675 nm; 870, 1020 and 1640 nm sharing the three set of polarizer triplets, respectively. However, the combinations may be different for different instruments, such as CE318-DP labeled #350 with 340, 380, 440, and 500 nm; 675 and 870 nm; 1020 and 1640 nm bands sharing the three sets of polarizer triplets, separately.

The automated mount of CE318-DP is a two-axis motorized system which rotates around two orthogonal axes (i.e., vertical axis and horizontal axis) and carries the optical sensor head to specific measuring angles (CE318Manual, 2014). The connecting line of two collimators should be perpendicular to the arm of the automated mount when assembling the optical sensor head

3 Measurement of skylight polarization

Table 3.1: Center wavelengths, bandwidths (FWHM), polarization detection capabilities and detectors for different channels of CE318-DP (Li et al., 2015).

Channel(nm)	FWHM(nm)	Polarization(Y/N)	Detector
340	2	Y	silicon
380	4	Y	silicon
440	10	Y	silicon
500	10	Y	silicon
675	10	Y	silicon
870	10	Y	silicon
936	10	N	silicon
1020	10	Y	silicon
1640	25	Y	InGaS

to the automated mount of CE318-DP, see Fig. 3.3. The electronic box is a unit that controls and memorizes the measurements as well as the positions of the two axes of the automated mount (CE318Manual, 2014). Originally, there are two non-polarization and one polarization scenarios to measure sky radiances, see Fig. 3.4. Among them, the unpolarized ALMucantar (ALM) scenario measures sky radiances in the azimuthal plane with a zenith angle of view equal to the solar zenith angle; the unpolarized Solar Principle Plane (SPP) scenario measures sky radiances in the solar principal plane; the Polarized Principle Plane (PPP) scenario measures polarization distribution of skylight also in the solar principal plane. For this observation geometry, the Relative Azimuthal Angle (RAA) equals to 0° or 180° , and the scanning angles vary from $+95^\circ$ to $+265^\circ$ with increments of 5° , see Tab. 3.2. Here, 180° represents zenith observation. Scanning angles exceeding 180° indicate the anti-solar direction, otherwise, the solar direction.

In the solar principal plane, measurements of U equal to 0 for most of scanning angles deviated from the solar direction in ideal condition (Emde et al., 2010). Then Q varies for different scanning angles. Thus, the available information on skylight polarization is limited for this observation geometry. In view of this limitation, the polarization observation geometry of CE318-DP

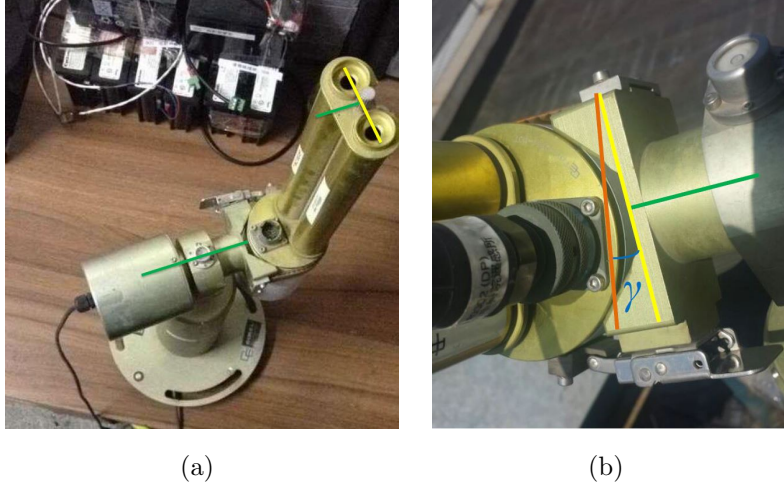


Figure 3.3: Installation of the optical sensor head and arm of the automated mount of CE318-DP. (a) ideal installation with the optical sensor head perpendicular to the arm of the automated mount; (b) non-ideal installation with an initial error angle between the orange line and the yellow line, where γ indicates the initial angle with respect to the orientation of ideal installation.

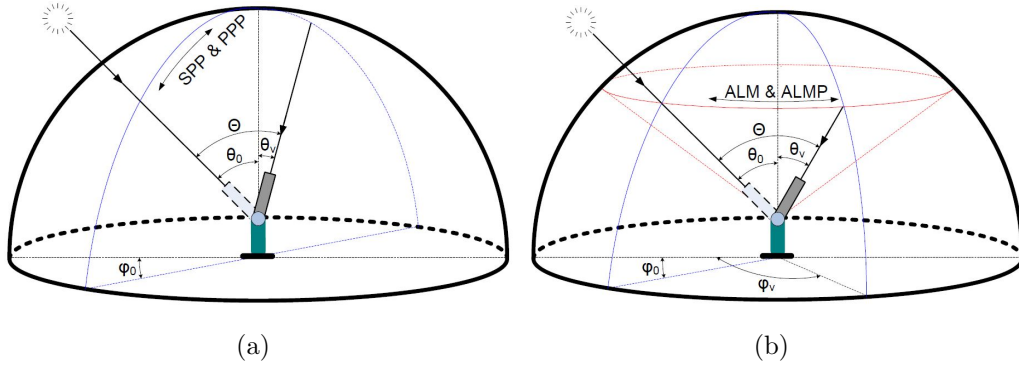


Figure 3.4: Observation geometries of the CE318-DP. (a) “SPP” denotes the Solar Principal Plane scenario (non-polarization); “PPP” indicates the Polarized Principal Plane scenario. (b) “ALM” represents the ALMucantar scenario (non-polarization); “ALMP” denotes the Polarized ALMucantar scenario (Li et al., 2015).

are extended. Polarization measurements in the almucantar plane, namely the Polarized ALMucantar (ALMP), are additionally conducted. ALMP is the observation geometry with viewing zenith angle equal to solar zenith angle while varying azimuthal angles from the sun, see Fig. 3.4 (b) (Voss and Liu, 1997). The relative azimuthal angles observed in the ALMP scenario are listed in Tab. 3.2.

Table 3.2: Observation angles for different polarization scenarios of the CE318-DP (Li et al., 2015).

Scenarios	Observation angles ($^{\circ}$)
PPP (Scanning angles)	95, 100, 105, 110, 115, 120, 125, 130, 135, 140, 145, 150, 155, 160, 165, 170, 175, 180, 185, 190, 195, 200, 205, 210, 215, 220, 225, 230, 235, 240, 245, 250, 255, 260, 265
ALMP (Relative azimuthal angles)	30, 35, 40, 45, 50, 60, 70, 80, 90, 100, 120, 140, 160, and 180 in the right half-circle; 330, 325, 320, 315, 310, 300, 290, 280, 270, 260, 240, 220, 200, and 180 in the left half-circle

The CE318-DP instrument preforms polarization measurements at 35 scanning angles in the solar principal plane and at 28 relative azimuthal angles in the almucantar geometry per hour. At each observing angle, three radiance measurements are made one by one with each linear polarizer keeping 60° between every two orientations of the polarizer-preferred transmittance axes (called the polarizer axes in the subsequent text for short).

3.2 Calibration of the polarized radiances

A reference polarized light source with known polarization state is required for calibration of the degree of linear polarization measurements (Li et al.,

3 Measurement of skylight polarization

2010). The POLBOX system, a device applying parallel glasses using an integrating sphere as light source, generates linearly polarized light with *DoLP* from 0 to ~ 0.6 in a spectral range from visible to near infrared, but without UV capability. The accuracy of calibration depends on the Lambertian light source and the polarization device, which should be kept in good condition. Dirty glass blades may introduce a polarization by the device itself (Pietras et al., 2000). Unfortunately, that is inevitable in realistic environments. Instead of the POLBOX, a polarimetric reference for *DoLP* calibration based on the direct and reflected solar light has been introduced (Li et al., 2010). However, it also has a strict requirement of very smooth water surface. That is hard to realize in real circumstances as well.

For CE318-DP, only calibration of *DoLP* is not sufficient to get the Stokes parameters Q and U . The calibration coefficients of absolute polarized radiances are necessary. As discussed above, the CE318-DP measures three radiances of the polarized skylight with a set of triplet linear polarizers in each wavelength channel. The Stokes parameters I , Q , and U are calculated from three radiance measurements. The measurements are saved as digital numbers in a raw data file. Similar to the radiometric calibration in unpolarized channels, the radiance of each measurement is calculated by

$$I_{i,j} = C_{i,j} \cdot N_{i,j}, \quad (3.1)$$

where I is the polarized radiance that incidents into the instrument (in $\text{W m}^{-2} \text{ nm}^{-1} \text{ sr}^{-1}$). C represents the calibration coefficient of radiance for the polarized channels. N is the measured digital number. i indicates three polarizers, and $i = 1, 2, 3$; j denotes the channel index corresponding to eight wavelengths with polarization measurements, and $j = 1, 2, 3, 4, 5, 6, 7, 8$.

Polarization calibration coefficients are vital to obtain the measured radiances and then to calculate the Stokes components and other polarization parameters. For the new instruments, calibration coefficients C in the instrument's documentation supplied by the manufacture are adopted. However, the instrument's working state will be changed after running a long period. Then, a recalibration is required, at least after one-year operation in SONET. Like absolute radiance calibration for non-polarized channels, the absolute

calibration coefficients for polarized channels are obtained by measuring unpolarized light from an integrating sphere, see Fig. 3.5. The polarization calibration is more complicated than the calibration of non-polarized radiance in general (Goloub et al., 2007; Li et al., 2010). However, the calibration of absolute polarized radiance is easier to implement in comparison with the calibration of the degree of linear polarization, because no special device of reference polarized light (e.g., the POLBOX system) is required.

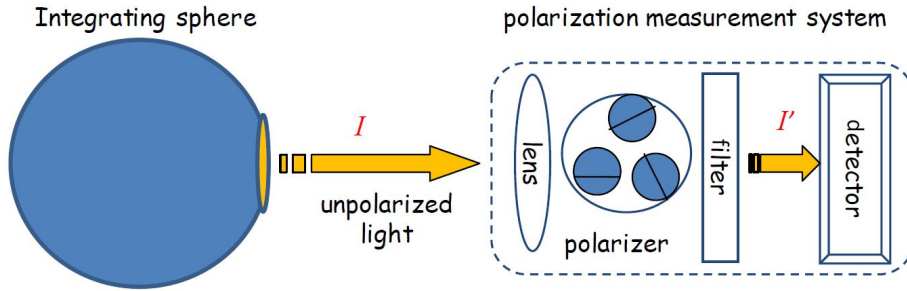


Figure 3.5: Schematic diagram of calibration of the polarized radiances for the polarized channels of CE318-DP.

The polarized channels of CE318-DP are calibrated by using an integrating sphere with stable radiance in laboratory. The light emitted from an integrating sphere is regarded as unpolarized (i.e., $DoLP = 1$). For a perfect linear polarizer, transmittance along the preferred axis $k_1 = 1$, and transmittance along an axis 90° to the preferred axis $k_2 = 0$. Since incident light is unpolarized with a total radiance of I , effect of the unpolarized incident light passing through a perfect linear polarizer is to provide linear polarized light with half of the radiance. That is,

$$I'_{i,j} = \frac{1}{2} I_{i,j}. \quad (3.2)$$

The polarizing efficiency is introduced to describe a real, imperfect polarizer. It is defined as

$$\eta = \sqrt{\frac{k_1 - k_2}{k_1 + k_2}} \times 100 \%. \quad (3.3)$$

Considering that one set of three polarizers are from the same product batch with identical quality, it is supposed that the polarizing efficiencies for the three polarizers are equal (Li et al., 2010). For most of the CE318-DP instruments, the polarizing efficiencies equal to 1 for short wave channels (e.g., 440, 500, 675, 870, 1020 nm), and almost equal to 1 for long wave channels (such as 1640 nm) according to the instrument’s documentation. Then, we can consider $k_1 = 1$ and $k_2 = 0$ here. Those are also widely adopted in literatures (Voss and Liu, 1997; Stam et al., 2002; Li et al., 2010). Thus, the polarized radiance of each measurement is calculated by

$$I'_{i,j} = \frac{1}{2} C_{i,j} \cdot N_{i,j}. \quad (3.4)$$

3.3 Measurement sites

The ground-based automatic CIMEL sun/sky radiometer (CE318) has been introduced into some global and regional aerosol observation networks several decades ago, for example, the AERosol RObotic NETwork (AERONET), and the PHOtométrie pour le Traitement Opérationnel de Normalisation Satellitaire (PHOTONS) (Holben et al., 1998; Li et al., 2010). As a global ground-based aerosol remote sensing network, the AERONET provides measurements of columnar aerosol properties at more than 1100 sites. However, only a few sites are equipped with the extension of multi-wavelength polarization version CE318-DP.

The SONET, established by the Institute of Remote Sensing and Digital Earth (RADI), Chinese Academy of Sciences in 2010, includes 17 long-term observation stations and ~ 40 temporary observation sites around China (by the end of 2015), see Fig. 3.6. Most of them are equipped with the new Dual-Polar version CE318-DP (Li et al., 2015). Tab. 3.3 provides some general information (including serial numbers of the optical heads, latitudes, longitudes, altitudes and beginnings of the measurements) on the 12 long-term polarization observation stations within SONET. All of the stations have continuously measured for more than one year. The site with the longest data record is “Beijing-RADI”, which is a joint site of AERONET and SONET

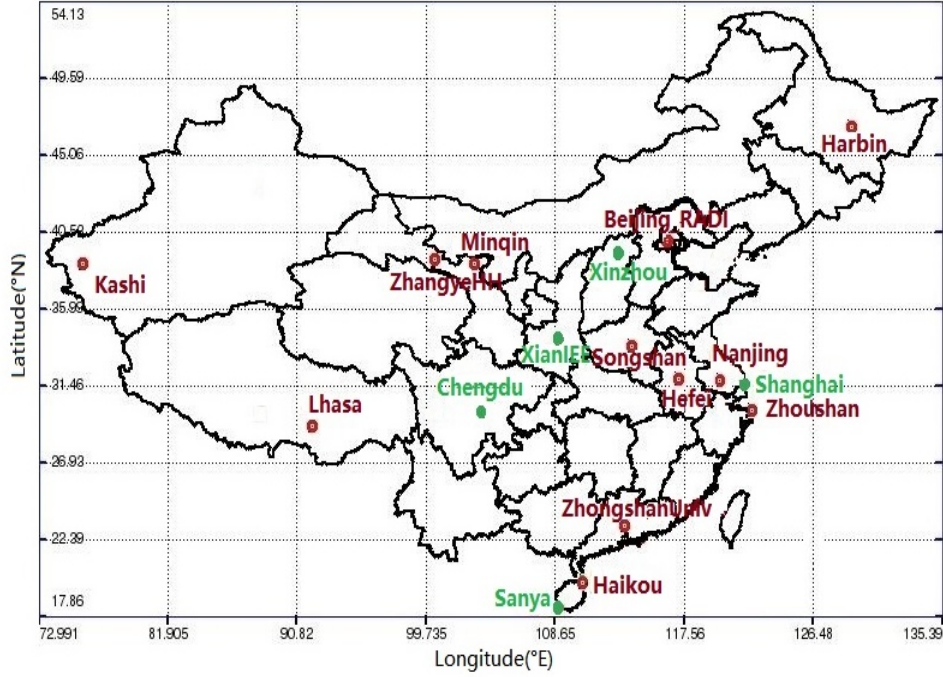


Figure 3.6: The SONET long-term site map (red dots denote 12 polarization observation sites, and green dots represent 5 non-polarization observation sites).

and the only site with polarized almucantar observations. This station has polarization observations lasting for six years in the solar principal plane geometry and for more than two years in the almucantar geometry by the end of 2015. The SONET aerosol observation network is regarded as “the 5th network (others are the AERONET, SKYNET, PHOTONS, GAW) in the world owing systematical atmospheric radiation properties observation function integrating calibration, retrieval, and quality control capabilities” (by Philippe Goloub, 2014). With reliable and continuous measurements in key areas of China, SONET provides multi-angle multi-spectral polarimetric measurements to study detailed properties of different types of aerosol particles. Furthermore, the data are going to be used for validating polarization measurements and aerosol products of new spaceborne and airborne polarization instruments.

Table 3.3: Information on polarization observation sites of SONET (listed in chronological order of site establishments).

Site	Instrument #	Latitude($^{\circ}$ N), Longitude($^{\circ}$ E), Altitude(m)	Beginning of measurement
Beijing-RADI	350	40.0, 116.4, 59	23/12/2009
ZhongshanUniv	964	23.1, 113.4, 28	27/10/2011
Zhoushan	954	29.9, 122.2, 29	08/02/2012
Minqin	969	38.6, 103.1, 1364	22/02/2012
ZhangyeHH	962	38.9, 100.4, 1589	24/07/2012
Kashi	973	39.5, 75.9, 1320	29/06/2013
Hefei	967	31.9, 117.2, 36	10/07/2013
Harbin	1105	45.7, 126.6, 223	08/08/2013
Lhasa	966	29.7, 91.0, 3690	29/09/2013
Songshan	971	34.5, 113.1, 475	03/11/2013
Haikou	1118	19.9, 110.3, 22	06/03/2014
NanjingUniv	959	32.1, 118.9, 52	30/06/2014

In this study, only typical cases for different aerosol types are selected from sufficiently long observations, including a haze polluted urban case at the “Beijing-RADI” site, a rural case at the “ZhangyeHH” site, a clean continental case at the “Lhasa” site, a mineral dust case at the “Minqin” site, and a Maritime case at the “Zhoushan” site. Skylight polarization in a haze polluted case with that in a clear case at the “Beijing-RADI” site observed in the new polarized almucantar geometry are also discussed in the following.

Chapter 4

Method of Stokes parameter derivation

4.1 Definitions of the reference frames

As discussed above, the Stokes vector and derived polarization parameters need to be described with respect to specific reference planes and corresponding coordinate systems. According to the definitions, the total radiance I and the $DoLP$ are independent of the reference plane, while the Stokes parameters Q , U , and the AoP vary with the choice of reference plane. Although the reference plane can be arbitrarily chosen, observational or theoretical circumstances may make a certain plane preferable over others (Hovenier et al., 2004). When considering polarization involving a single scattering process, we normally choose the scattering plane which contains the propagation directions of the incident and scattered light as a reference. Instead when considering polarization due to multiple-scattering processes in the atmosphere, the local meridian plane that contains the viewing and local zenith directions is usually chosen as a reference, see Fig. 2.1 (Schutgens et al., 2004; Boesche et al., 2006; Bhandari et al., 2011; Rozanov et al., 2014). For a general coordinate system associated with a reference plane, we define a right-handed Cartesian coordinate system $(\hat{l}, \hat{r}, \hat{z})$ where the unit vectors

\hat{l} , \hat{r} , and \hat{z} are used to denote the directions of three axes of the Cartesian coordinate system. In this coordinate frame, \hat{z} -axis is along the direction of the scattered light propagation, \hat{l} -axis is within the reference plane and is perpendicular to the \hat{z} -axis, and \hat{r} -axis is perpendicular to both the \hat{z} -axis and the reference plane (Tilstra et al., 2003).

To keep consistent with vector radiative transfer models and other polarization measurements, the coordinate system based on the sky frame should be adopted to describe the Stokes parameters (Bhandari et al., 2011). In this frame, the local meridian plane is defined as the reference plane. The corresponding coordinate system $(\hat{l}_{\text{sky}}, \hat{r}_{\text{sky}}, \hat{z}_{\text{sky}})$ is a right-handed Cartesian coordinate system with \hat{l}_{sky} - and \hat{r}_{sky} -axes parallel and perpendicular to the reference plane, respectively. Light propagates along the $\hat{z}_{\text{sky}} = \hat{r}_{\text{sky}} \times \hat{l}_{\text{sky}}$ direction, see Fig. 4.1. Note that only one coordinate system (i.e., for the viewing direction of 180°) is illustrated here. The coordinate system is changed for different viewing directions in the solar principal and the almucantar planes. As a convention, signs of the Stokes parameters Q and U in this frame are defined such that $+Q$ is aligned with \hat{l} -axis; $-Q$ is aligned with \hat{r} -axis; $+U$ is aligned with the bisectrix of $+\hat{l}$ and $+\hat{r}$, or $-\hat{l}$ and $-\hat{r}$; and $-U$ is aligned with the bisectrix of $+\hat{l}$ and $-\hat{r}$, or $-\hat{l}$ and $+\hat{r}$, see Fig. 4.2. As mentioned in Chapter 3, the CE318-DP originally observes polarization only in the solar principal plane geometry (i.e., PPP). In this study, the observing capability of CE318-DP is extended. Polarization measurements in the Polarized ALMucantar (ALMP) geometry are additionally conducted, which also contains a solar principal plane observation with RAA equal to 180° . For the solar principal plane observations, incident direction of sunlight, the local zenith, and the instrument's viewing direction are in the same plane. That means, the solar principal plane corresponds to the meridian plane. Thus, the solar principal plane is also the reference plane in this situation, see Fig. 2.1.

Regarding to actual observing processes of the CE318-DP, radiance measurements by a set of triplet linear polarizers are related to the Stokes parameters I , Q , and U for every spectral filter at each observing angle. Orientations of the three polarizers are separated by 60° , see Section 3.1. For simplicity, we can assume the polarizer axes are 0° , 60° , and 120° , respectively. The

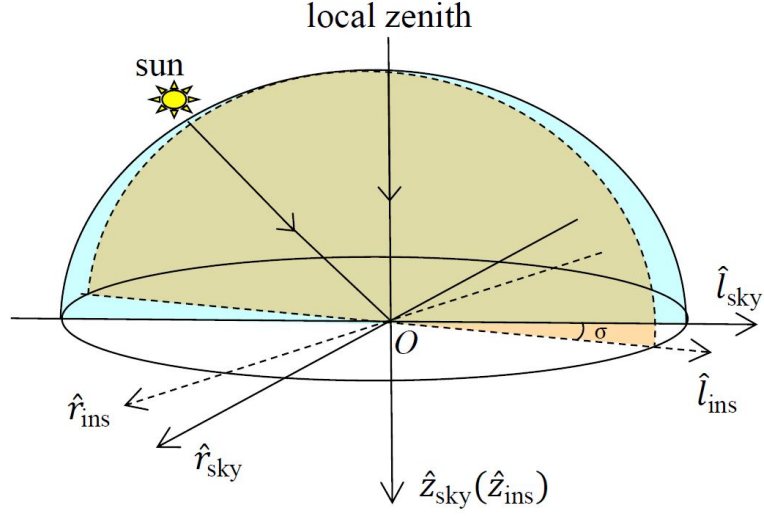


Figure 4.1: Schematic diagram of the reference coordinate systems in the sky frame ($\hat{l}_{\text{sky}}, \hat{r}_{\text{sky}}, \hat{z}_{\text{sky}}$) and in the instrument frame ($\hat{l}_{\text{ins}}, \hat{r}_{\text{ins}}, \hat{z}_{\text{ins}}$) for the viewing direction of 180° . The instrument is placed at the origin of the reference coordinate systems O . \hat{l}_{sky} -axis is in the meridian plane (i.e., the principal plane in this situation). \hat{l}_{ins} -axis is along the 0° polarizer axis of the instrument. \hat{z}_{sky} - and \hat{z}_{ins} - axes are coincident, along the direction of the light propagation. \hat{r}_{sky} -axis is perpendicular to the meridian plane. \hat{r}_{ins} -axis is perpendicular to both \hat{l}_{ins} - and \hat{z}_{ins} -axes. σ is a rotation angle for transforming of the reference coordinate systems.

initial position of the 0° polarizer axis is generally not in the reference plane of the sky frame. And the angle between them is unknown due to the uncontrolled installation angle of the optical sensor with respect to the reference plane, see Fig. 3.3(b). Therefore, we have to define the Stokes parameters in a new instrument frame with the plane containing the direction of 0° polarizer axis and the direction of propagation of light as a reference. In the instrument frame, the corresponding coordinate system is $(\hat{l}_{\text{ins}}, \hat{r}_{\text{ins}}, \hat{z}_{\text{ins}})$, where the \hat{l}_{ins} -axis is along the 0° polarizer-preferred transmittance axis; \hat{z}_{ins} -axis is along the direction of the scattered light propagation; and \hat{r}_{ins} -axis is perpendicular to both \hat{l}_{ins} - and \hat{z}_{ins} -axes, satisfying the right-hand rule, see Fig. 4.1. With this definition, the Stokes parameters are calculated in the

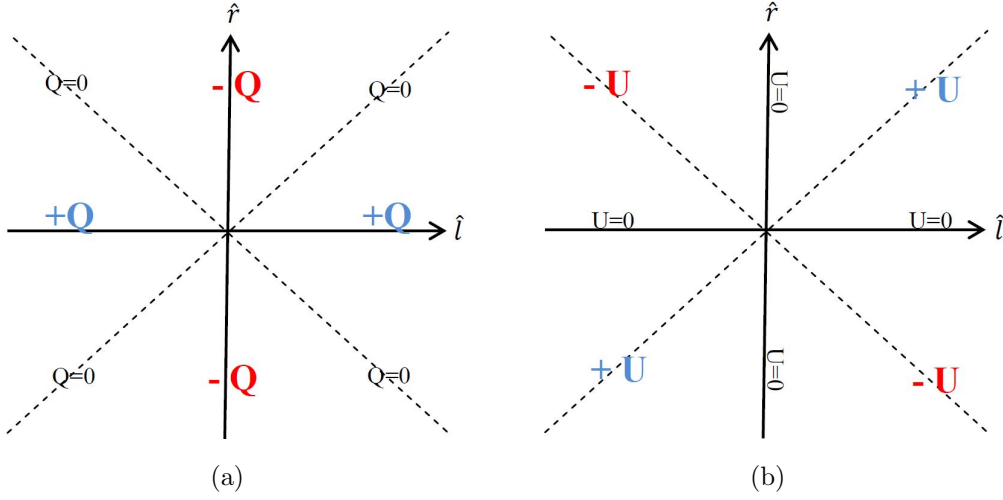


Figure 4.2: The signs of the Stokes parameters Q (a) and U (b). Redrawn from <http://en.wikipedia.org> with modification.

instrument coordinate system from three radiance measurements (Boesche et al., 2006). To further obtain the Stokes parameters in the sky frame, we need to transform the reference coordinate system from the instrument frame $(\hat{l}_{\text{ins}}, \hat{r}_{\text{ins}}, \hat{z}_{\text{ins}})$ to the sky frame $(\hat{l}_{\text{sky}}, \hat{r}_{\text{sky}}, \hat{z}_{\text{sky}})$.

4.2 Calculation of the polarization parameters

Interactions of polarized light with atmospheric particles (i.e., air molecules, aerosol particles and cloud droplets) and land surfaces are described by a series of scattering or phase matrices, see Chapter 2. Similar to atmospheric particles, any optical instrument may also cause absorption, scattering, reflection, and refraction of light. Likewise, these actions can be described by the instrument's Mueller matrix \mathbf{M}_p (Kokhanovsky, 2003). The polarized channels of CE318-DP detect radiances as the measurement quantities, which depend on the instrument's Mueller matrix and the Stokes vector of the light incident on the system (Voss and Liu, 1997). If the instrument's

Mueller matrix is known, the Stokes parameters I , Q , and U of the incident light are calculated from the three radiance measurements through a set of triplet polarizers, see Fig. 4.3. The processes can be described by

$$\begin{aligned}
 \begin{pmatrix} I \\ Q \\ U \end{pmatrix} &= \mathbf{M}_m \mathbf{M}_a \cdots \mathbf{M}_{ms} \begin{pmatrix} I_0 \\ 0 \\ 0 \end{pmatrix} \\
 &= \mathbf{M}_p^{-1}(\Psi) \begin{pmatrix} I'(\Psi_1) \\ I'(\Psi_2) \\ I'(\Psi_3) \end{pmatrix} \\
 &= \frac{1}{2} \begin{pmatrix} C_1 \\ C_2 \\ C_3 \end{pmatrix} \begin{pmatrix} N(\Psi_1) \\ N(\Psi_2) \\ N(\Psi_3) \end{pmatrix}
 \end{aligned} \tag{4.1}$$

where $(I_0, 0, 0)^T$ is the Stokes vector of sunlight directly incident at the TOA. $\mathbf{M}_m, \mathbf{M}_a, \dots, \mathbf{M}_{ms}$ indicate the Mueller matrices describing interactions of sunlight with air molecules, aerosol particles, and cloud droplets in the atmosphere, the land surface, as well as the multiple scattering processes, respectively. The Stokes vector $(I, Q, U)^T$ depicts partially polarized light incident into the instrument. \mathbf{M}_p^{-1} is the inverse Mueller matrix of the instrument's system. I' represent the radiances and N represent the digital numbers, which are detected by the instrument with three orientations of the polarizer axes Ψ_1, Ψ_2 , and Ψ_3 , separately. C_1, C_2 , and C_3 are corresponding calibration coefficients of radiances for the polarized channels of CE318-DP, see Section 3.2.

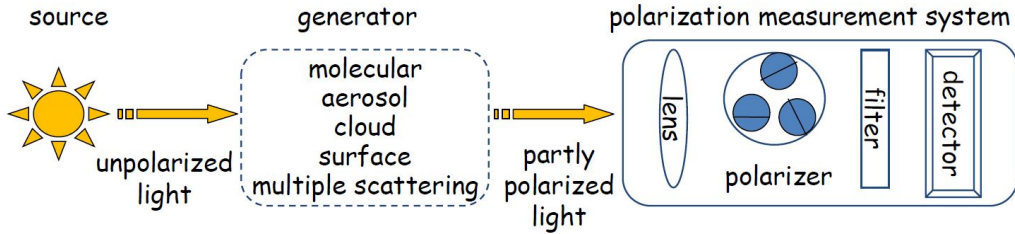


Figure 4.3: Schematic diagram of the processes of skylight polarization detected by the CE318-DP.

4 Method of Stokes parameter derivation

The CE318-DP uses linear polarizers as main polarization optical elements. The interactions of optical elements with incident light can be expressed by (Voss and Liu, 1997)

$$\begin{pmatrix} I' \\ Q' \\ U' \\ V' \end{pmatrix} = \mathbf{M}_p(\Psi) \begin{pmatrix} I \\ Q \\ U \\ V \end{pmatrix}, \quad (4.2)$$

$$\begin{pmatrix} I' \\ Q' \\ U' \\ V' \end{pmatrix} = \frac{1}{2} \begin{bmatrix} k_1 + k_2 & (k_1 - k_2) \cdot \cos 2\Psi & & \\ (k_1 - k_2) \cdot \cos 2\Psi & (k_1 + k_2) \cdot \cos^2 2\Psi + 2\sqrt{k_1 k_2} \cdot \sin^2 2\Psi & & \\ (k_1 - k_2) \cdot \sin 2\Psi & (k_1 + k_2 - 2\sqrt{k_1 k_2}) \cdot \cos 2\Psi \cdot \sin 2\Psi & & \\ 0 & 0 & & \end{bmatrix} \begin{pmatrix} I \\ Q \\ U \\ V \end{pmatrix}, \quad (4.3)$$

where $(I, Q, U, V)^T$ is the Stokes vector of incoming light, and $(I', Q', U', V')^T$ is the Stokes vector of light detected by CE318-DP. $\Psi = \psi + \gamma$, and ψ is the orientation angle of the polarizer axis for perfect installation, that can be measured by facing to the direction of light propagation and rotating counterclockwise from the reference plane to the linear polarizer-preferred transmission plane. γ is the initial angle of the polarizer axis with respect to the orientation of perfect installation indicated by the connecting line of two collimators perpendicular perfectly to the arm of automated mount for the CE318-DP, see Fig. 3.3 (b). Previous studies have shown that the initial installation angle of polarizer is an important element affecting measurement accuracy of polarization (Chen et al., 2008). k_1 is transmittance of the linear polarizer along the preferred axis, and k_2 is transmittance of the linear polarizer along an axis 90° to the preferred axis. $k_1 = 1$ and $k_2 = 0$ are

adopted in this study, see also Section 3.2. Then, we have

$$\begin{pmatrix} I' \\ Q' \\ U' \\ V' \end{pmatrix} = \frac{1}{2} \begin{bmatrix} 1 & \cos 2\Psi & \sin 2\Psi & 0 \\ \cos 2\Psi & \cos^2 2\Psi & \cos 2\Psi \cdot \sin 2\Psi & 0 \\ \sin 2\Psi & \cos 2\Psi \cdot \sin 2\Psi & \sin^2 2\Psi & 0 \\ 0 & 0 & 0 & 0 \end{bmatrix} \begin{pmatrix} I \\ Q \\ U \\ V \end{pmatrix}. \quad (4.4)$$

The total radiances at three orientation angles of linear polarizer axes (i.e., Ψ_1 , Ψ_2 , and Ψ_3) are measured by the CE318-DP at each observing position. According to Eq.(4.4), we have

$$\begin{pmatrix} I'(\Psi_1) \\ I'(\Psi_2) \\ I'(\Psi_3) \end{pmatrix} = \frac{1}{2} \begin{bmatrix} 1 & \cos 2\Psi_1 & \sin 2\Psi_1 \\ 1 & \cos 2\Psi_2 & \sin 2\Psi_2 \\ 1 & \cos 2\Psi_3 & \sin 2\Psi_3 \end{bmatrix} \begin{pmatrix} I \\ Q \\ U \end{pmatrix}. \quad (4.5)$$

Then, the Stokes parameters I , Q , and U of an incoming polarized light is determined by inversion of Eq.(4.5). That is (Aben et al., 1997; Stam et al., 2002)

$$\begin{aligned} \begin{pmatrix} I \\ Q \\ U \end{pmatrix} &= \mathbf{M}_p^{-1} \begin{pmatrix} I'(\Psi_1) \\ I'(\Psi_2) \\ I'(\Psi_3) \end{pmatrix} \\ &= \begin{bmatrix} \sin (2\Psi_3 - 2\Psi_2) & \sin (2\Psi_1 - 2\Psi_3) & \sin (2\Psi_2 - 2\Psi_1) \\ \sin 2\Psi_2 - \sin 2\Psi_3 & \sin 2\Psi_3 - \sin 2\Psi_1 & \sin 2\Psi_1 - \sin 2\Psi_2 \\ \cos 2\Psi_3 - \cos 2\Psi_2 & \cos 2\Psi_1 - \cos 2\Psi_3 & \cos 2\Psi_2 - \cos 2\Psi_1 \end{bmatrix} \\ &\quad \times \frac{1}{2 \sin (\Psi_1 - \Psi_2) \cdot \sin (\Psi_2 - \Psi_3) \cdot \sin (\Psi_3 - \Psi_1)} \begin{pmatrix} I'(\Psi_1) \\ I'(\Psi_2) \\ I'(\Psi_3) \end{pmatrix}. \end{aligned} \quad (4.6)$$

When choosing the instrument coordinate system as reference, the 0° polarizer axis is within the reference plane. Then, the polarizer orientation angles can be determined following $\Psi_1 = 0^\circ$, $\Psi_2 = 60^\circ$, and $\Psi_3 = 120^\circ$. Substitute them into Eq.(4.6), the Stokes parameters in the instrument frame

is obtained. Namely,

$$\begin{pmatrix} I \\ Q \\ U \end{pmatrix} = \frac{2}{3} \begin{bmatrix} 1 & 1 & 1 \\ 2 & -1 & -1 \\ 0 & \sqrt{3} & -\sqrt{3} \end{bmatrix} \begin{pmatrix} I'_{0^\circ} \\ I'_{60^\circ} \\ I'_{120^\circ} \end{pmatrix}. \quad (4.7)$$

Then, the degree of linear polarization is calculated as

$$DoLP = \frac{2\sqrt{I_{0^\circ}^2 + I_{60^\circ}^2 + I_{120^\circ}^2 - I'_{0^\circ} \cdot I'_{60^\circ} - I'_{60^\circ} \cdot I'_{120^\circ} - I'_{120^\circ} \cdot I'_{0^\circ}}}{I'_{0^\circ} + I'_{60^\circ} + I'_{120^\circ}}, \quad (4.8)$$

and the angle of polarization is

$$\chi = \frac{1}{2} \arctan \left(\frac{U}{Q} \right) = \frac{1}{2} \arctan \sqrt{3} \left(\frac{I'_{120^\circ} - I'_{60^\circ}}{I'_{120^\circ} + I'_{60^\circ} - 2I'_{0^\circ}} \right). \quad (4.9)$$

In above calculations, we adopt the instrument frame with the 0° polarizer-preferred transmittance plane as a reference. For the three sets of triplet polarizers on the polarizer's wheel of CE318-DP (see Section 3.1), which correspond to different wavelengths, the orientations of the three 0° polarizer-preferred transmittance axes are different and there are no fixed relationships among them. Thus, the polarization parameters calculated in the instrument frame are based on three different instrument coordination systems. That means, the results at different wavelengths can not be compared with each other. Furthermore, the initial angle of the polarizer axis will be changed if the optical sensor head and the arm of automated mount are reassembled. Then, the instrument coordinate system for the same wavelength are also not fixed.

Hence, to analyze polarization properties measured by different wavelength bands of CE318-DP and to compare them with the results of radiative transfer simulations and other polarization measurements, we need to transform the reference frame from the instrument frame $(\hat{l}_{\text{ins}}, \hat{r}_{\text{ins}}, \hat{z}_{\text{ins}})$ to the sky frame $(\hat{l}_{\text{sky}}, \hat{r}_{\text{sky}}, \hat{z}_{\text{sky}})$. The transformation is through rotation of the coordinate systems. When choosing the meridian plane as reference in the sky frame, the orientation angles of polarizers' axes are $\psi_1 = 0^\circ + \delta$, $\psi_2 = 60^\circ + \delta$, and $\psi_3 = 120^\circ + \delta$, where δ is the orientation angle of the 0° polarizer axis of perfect installation with respect to the reference plane, see

Fig. 4.4. However, the initial angle γ of the polarizer axis with respect to the orientation of perfect installation should be considered for actual installation. γ is uncertain due to non-ideal installation of the optical sensor head to the automated mount of CE318-DP, see Fig. 3.3 (b) and Fig. 4.4. Once installed, this angle is constant for all polarizers on the same polarizer's wheel. Therefore, we can assume $\Psi_1 = \psi_1 + \gamma = 0^\circ + \delta + \gamma$, $\Psi_2 = \psi_2 + \gamma = 60^\circ + \delta + \gamma$, and $\Psi_3 = \psi_3 + \gamma = 120^\circ + \delta + \gamma$, see Fig. 4.4. For three radiance measurements based on one set of triplet polarizers, δ and γ are invariable. Then we obtain a counterclockwise rotation angle $\sigma = \delta + \gamma$.

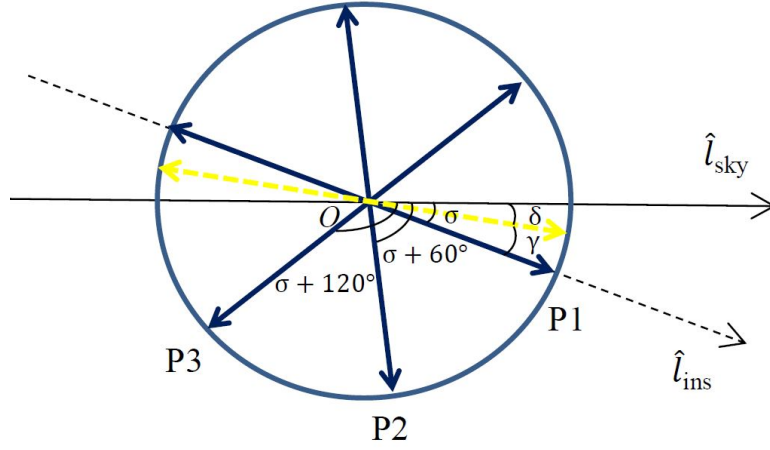


Figure 4.4: Illustration of the orientation angles of a set of triplet linear polarizer axes in the sky frame for the viewing direction of 180° . The instrument is located at the origin O . The light is traveling perpendicular into the paper. \hat{l}_{sky} -axis is in the meridian plane (i.e., the principal plane in this situation). \hat{l}_{ins} -axis is along the 0° polarizer axis of the instrument. They are corresponding to \hat{l}_{sky} - and \hat{l}_{ins} -axes in Fig. 4.1. σ is the rotation angle for transforming of the reference coordinate systems. “P1”, “P2”, and “P3” denote the 0° , 60° , and 120° polarizers, respectively. The blue double-headed arrows indicate the orientations of polarizers’ transmittance axes. The yellow double-headed arrow indicates the orientation of the 0° polarizer axis for ideal installation. The orientation angles of the three polarizer axes are $\sigma + 0^\circ$, $\sigma + 60^\circ$, and $\sigma + 120^\circ$.

The rotation process of the two coordinate systems can be expressed as a rotation matrix. The relation of electric field vectors before and after coordinate system rotation are given by

$$\begin{pmatrix} E_{\text{corr},l} \\ E_{\text{corr},r} \end{pmatrix} = \mathbf{R}(\sigma) \cdot \begin{pmatrix} E_l \\ E_r \end{pmatrix} = \begin{bmatrix} \cos \sigma & \sin \sigma \\ -\sin \sigma & \cos \sigma \end{bmatrix} \begin{pmatrix} E_l \\ E_r \end{pmatrix}, \quad (4.10)$$

where $(E_l, E_r)^T$ is the electric field vector in the original instrument frame; $(E_{\text{corr},l}, E_{\text{corr},r})^T$ is the electric field vector after reference coordinate system correction, namely, in the new uniform sky frame. $\mathbf{R}(\sigma)$ is the 2×2 rotation matrix, and σ is a counterclockwise rotation angle between the instrument frame and the sky frame. Then, we have

$$\begin{pmatrix} E_l \\ E_r \end{pmatrix} = \mathbf{R}^{-1}(\sigma) \cdot \begin{pmatrix} E_{\text{corr},l} \\ E_{\text{corr},r} \end{pmatrix} = \begin{bmatrix} \cos \sigma & -\sin \sigma \\ \sin \sigma & \cos \sigma \end{bmatrix} \begin{pmatrix} E_{\text{corr},l} \\ E_{\text{corr},r} \end{pmatrix}, \quad (4.11)$$

$$E_l = \cos \sigma \cdot E_{\text{corr},l} - \sin \sigma \cdot E_{\text{corr},r}, \quad (4.12)$$

$$E_r = \sin \sigma \cdot E_{\text{corr},l} + \cos \sigma \cdot E_{\text{corr},r}. \quad (4.13)$$

The complex conjugate of electric field vector (superscript $*$) can be expressed in the same way:

$$E_l^* = \cos \sigma \cdot E_{\text{corr},l}^* - \sin \sigma \cdot E_{\text{corr},r}^*, \quad (4.14)$$

$$E_r^* = \sin \sigma \cdot E_{\text{corr},l}^* + \cos \sigma \cdot E_{\text{corr},r}^*. \quad (4.15)$$

According to the definition in Eq.(2.1), the Stokes parameters of polarized light are given by the components of electric field vector. Then, we have

$$\begin{aligned} I &= E_l \cdot E_l^* + E_r \cdot E_r^* \\ &= (\cos \sigma \cdot E_{\text{corr},l} - \sin \sigma \cdot E_{\text{corr},r}) \cdot (\cos \sigma \cdot E_{\text{corr},l}^* - \sin \sigma \cdot E_{\text{corr},r}^*) \\ &\quad + (\sin \sigma \cdot E_{\text{corr},l} + \cos \sigma \cdot E_{\text{corr},r}) \cdot (\sin \sigma \cdot E_{\text{corr},l}^* + \cos \sigma \cdot E_{\text{corr},r}^*) \quad (4.16) \\ &= E_{\text{corr},l} \cdot E_{\text{corr},l}^* + E_{\text{corr},r} \cdot E_{\text{corr},r}^* \\ &= I_{\text{corr}}, \end{aligned}$$

4 Method of Stokes parameter derivation

$$\begin{aligned}
Q &= E_l \cdot E_l^* - E_r \cdot E_r^* \\
&= (\cos \sigma \cdot E_{\text{corr},l} - \sin \sigma \cdot E_{\text{corr},r}) \cdot (\cos \sigma \cdot E_{\text{corr},l}^* - \sin \sigma \cdot E_{\text{corr},r}^*) \\
&\quad - (\sin \sigma \cdot E_{\text{corr},l} + \cos \sigma \cdot E_{\text{corr},r}) \cdot (\sin \sigma \cdot E_{\text{corr},l}^* + \cos \sigma \cdot E_{\text{corr},r}^*) \\
&= (\cos^2 \sigma - \sin^2 \sigma) \cdot E_{\text{corr},l} \cdot E_{\text{corr},l}^* - 2 \sin \sigma \cdot \cos \sigma \cdot E_{\text{corr},l} \cdot E_{\text{corr},r}^* \\
&\quad + (\sin^2 \sigma - \cos^2 \sigma) \cdot E_{\text{corr},r} \cdot E_{\text{corr},r}^* - 2 \sin \sigma \cdot \cos \sigma \cdot E_{\text{corr},l}^* \cdot E_{\text{corr},r} \\
&= \cos 2\sigma \cdot (E_{\text{corr},l} \cdot E_{\text{corr},l}^* - E_{\text{corr},r} \cdot E_{\text{corr},r}^*) \\
&\quad - \sin 2\sigma \cdot (E_{\text{corr},l} \cdot E_{\text{corr},r}^* + E_{\text{corr},l}^* \cdot E_{\text{corr},r}) \\
&= \cos 2\sigma \cdot Q_{\text{corr}} - \sin 2\sigma \cdot U_{\text{corr}},
\end{aligned} \tag{4.17}$$

$$\begin{aligned}
U &= E_l \cdot E_r^* + E_r \cdot E_l^* \\
&= (\cos \sigma \cdot E_{\text{corr},l} - \sin \sigma \cdot E_{\text{corr},r}) \cdot (\sin \sigma \cdot E_{\text{corr},l}^* + \cos \sigma \cdot E_{\text{corr},r}^*) \\
&\quad + (\sin \sigma \cdot E_{\text{corr},l} + \cos \sigma \cdot E_{\text{corr},r}) \cdot (\cos \sigma \cdot E_{\text{corr},l}^* - \sin \sigma \cdot E_{\text{corr},r}^*) \\
&= (\cos^2 \sigma - \sin^2 \sigma) \cdot E_{\text{corr},l} \cdot E_{\text{corr},r}^* + (\cos^2 \sigma - \sin^2 \sigma) \cdot E_{\text{corr},l}^* \cdot E_{\text{corr},r} \\
&\quad + 2 \sin \sigma \cdot \cos \sigma \cdot E_{\text{corr},l} \cdot E_{\text{corr},l}^* - 2 \sin \sigma \cdot \cos \sigma \cdot E_{\text{corr},r} \cdot E_{\text{corr},r}^* \\
&= \sin 2\sigma \cdot (E_{\text{corr},l} \cdot E_{\text{corr},l}^* - E_{\text{corr},r} \cdot E_{\text{corr},r}^*) \\
&\quad + \cos 2\sigma \cdot (E_{\text{corr},l} \cdot E_{\text{corr},r}^* + E_{\text{corr},l}^* \cdot E_{\text{corr},r}) \\
&= \sin 2\sigma \cdot Q_{\text{corr}} + \cos 2\sigma \cdot U_{\text{corr}},
\end{aligned} \tag{4.18}$$

$$\begin{aligned}
V &= i \cdot (E_l \cdot E_r^* - E_r \cdot E_l^*) \\
&= i \cdot [(\cos \sigma \cdot E_{\text{corr},l} - \sin \sigma \cdot E_{\text{corr},r}) \cdot (\sin \sigma \cdot E_{\text{corr},l}^* + \cos \sigma \cdot E_{\text{corr},r}^*) \\
&\quad - (\sin \sigma \cdot E_{\text{corr},l} + \cos \sigma \cdot E_{\text{corr},r}) \cdot (\cos \sigma \cdot E_{\text{corr},l}^* - \sin \sigma \cdot E_{\text{corr},r}^*)] \\
&= i \cdot [(\cos^2 \sigma + \sin^2 \sigma) \cdot E_{\text{corr},l} \cdot E_{\text{corr},r}^* - (\cos^2 \sigma + \sin^2 \sigma) \cdot E_{\text{corr},l}^* \cdot E_{\text{corr},r}] \\
&= i \cdot (E_{\text{corr},l} \cdot E_{\text{corr},r}^* - E_{\text{corr},l}^* \cdot E_{\text{corr},r}) \\
&= V_{\text{corr}}.
\end{aligned} \tag{4.19}$$

These yields

$$\begin{pmatrix} I \\ Q \\ U \\ V \end{pmatrix} = \mathbf{L}^{-1}(\sigma) \cdot \begin{pmatrix} I_{\text{corr}} \\ Q_{\text{corr}} \\ U_{\text{corr}} \\ V_{\text{corr}} \end{pmatrix} = \begin{bmatrix} 1 & 0 & 0 & 0 \\ 0 & \cos 2\sigma & -\sin 2\sigma & 0 \\ 0 & \sin 2\sigma & \cos 2\sigma & 0 \\ 0 & 0 & 0 & 1 \end{bmatrix} \cdot \begin{pmatrix} I_{\text{corr}} \\ Q_{\text{corr}} \\ U_{\text{corr}} \\ V_{\text{corr}} \end{pmatrix}, \quad (4.20)$$

and then,

$$\begin{pmatrix} I_{\text{corr}} \\ Q_{\text{corr}} \\ U_{\text{corr}} \\ V_{\text{corr}} \end{pmatrix} = \mathbf{L}(\sigma) \cdot \begin{pmatrix} I \\ Q \\ U \\ V \end{pmatrix} = \begin{bmatrix} 1 & 0 & 0 & 0 \\ 0 & \cos 2\sigma & \sin 2\sigma & 0 \\ 0 & -\sin 2\sigma & \cos 2\sigma & 0 \\ 0 & 0 & 0 & 1 \end{bmatrix} \cdot \begin{pmatrix} I \\ Q \\ U \\ V \end{pmatrix}, \quad (4.21)$$

where $(I, Q, U, V)^T$ is the Stokes vector in the original coordinate system $(\hat{l}_{\text{ins}}, \hat{r}_{\text{ins}}, \hat{z}_{\text{ins}})$ based on the instrument frame; $(I_{\text{corr}}, Q_{\text{corr}}, U_{\text{corr}}, V_{\text{corr}})^T$ is the transformed Stokes vector in the new coordinate system $(\hat{l}_{\text{sky}}, \hat{r}_{\text{sky}}, \hat{z}_{\text{sky}})$ based on the sky frame. $\mathbf{L}(\sigma)$ is the 4×4 rotation matrix of coordinate systems, and the rotation angle σ is a counterclockwise angle rotated from the original system to the new system. Considering that the total radiance I are constant with rotation of the reference coordinate systems and omitting the circularly polarized component, we can utilize above equation to recalculate the Stokes parameters Q_{corr} and U_{corr} in the sky frame, namely

$$\begin{pmatrix} Q_{\text{corr}} \\ U_{\text{corr}} \end{pmatrix} = \begin{bmatrix} \cos 2\sigma & \sin 2\sigma \\ -\sin 2\sigma & \cos 2\sigma \end{bmatrix} \cdot \begin{pmatrix} Q \\ U \end{pmatrix}. \quad (4.22)$$

The rotation matrix is a function of rotation angle σ . When transforming the reference coordinate systems, we have to know this angle. As discussed above, σ consists of two parts: δ and γ . For CE318-DP, it is hard to know the exact value of σ due to an unknown initial error angle γ which is brought in during the installation process, see Fig. 3.3 and Fig. 4.4. γ need to be considered when calculating the Stokes parameters Q and U . For different instruments, γ are different. Even for the same instrument and same operator, it may also be changed during different installation processes.

To obtain the rotation angle, we can take advantage of the polarization pattern of skylight. In the past decades, there have been significant stud-

4 Method of Stokes parameter derivation

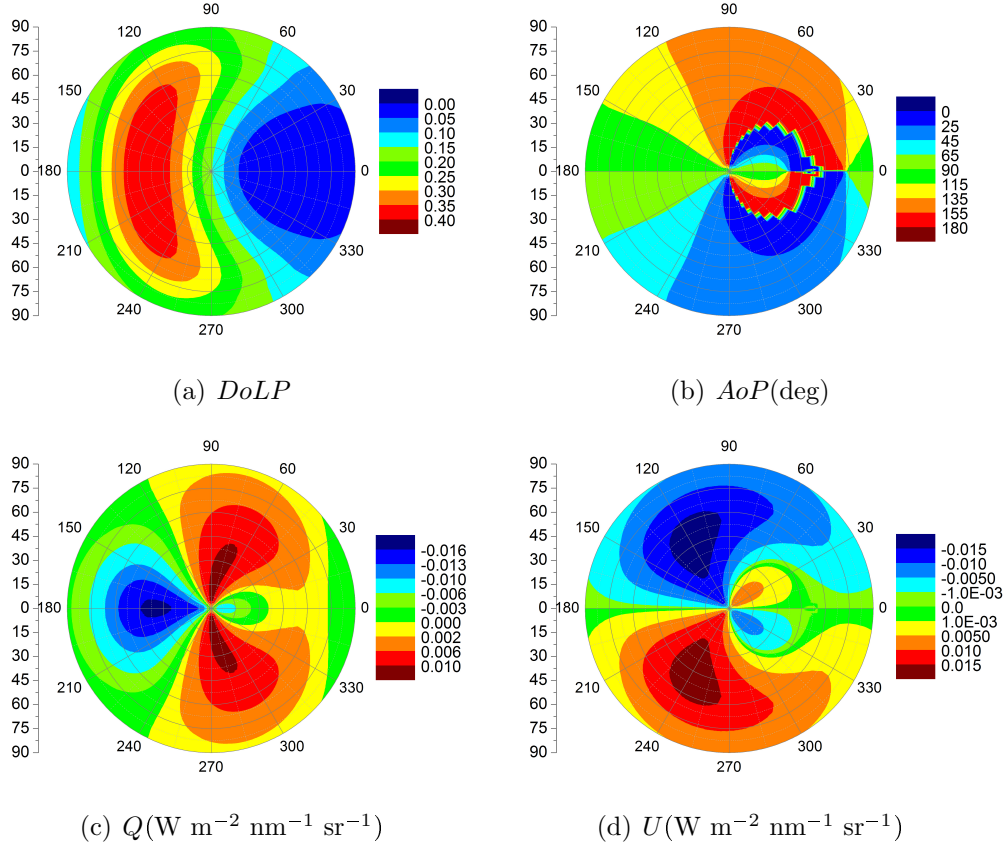


Figure 4.5: Counter plots of the polarization patterns of entire sky at 440 nm (simulated by SCIATRAN, where the aerosol type is “WMO-urban”; aerosol optical depth=1.0923; Rayleigh optical depth=0.24261; solar zenith angle=50.1293°; and the relative azimuthal angles of 0° and 180° indicate the solar and anti-solar directions of the principal plane, respectively).

ies on the polarization pattern of skylight in nature (Liu and Voss, 1997; Horváth and Varjú, 2004; Smith, 2007). Fig. 4.5 gives an example of the simulated polarization patterns of entire sky at 440 nm. According to the polarization pattern, the degree and direction of polarization of skylight are both related to location of the sun: i) The degree of linear polarization is maximum when the scattering angle is 90°. For other orientations, the degrees of linear polarization are less. The minimum occurs when the scattering angle is equal to 0° or 180°. The light from the anti-solar half of the sky is more polarized than that from the solar half, see Fig. 4.5 (a). ii) The di-

rection of polarization (i.e., the direction of electric field vector of EM wave oscillating) of the scattered light, by definition, is in the polarization plane which should be perpendicular to the scattering plane. For the solar principal plane observation geometry, it is also perpendicular to the principal plane. Correspondingly, the angle of polarization χ should be equal to 90° for the principal plane observations, see Fig. 4.5 (b).

Previous studies have shown that this polarization pattern of skylight is true in different atmospheric conditions, even in case the sun is obscured by clouds or below the horizon (Smith, 2007). This fact has been widely used in navigation. For example, some insects utilize polarization of skylight to infer position of the sun when it can not be observed directly (Horváth and Varjú, 2004). Likewise, we can also make use of the polarization pattern of skylight around the maximum polarization in the anti-solar half of sky. For solar principal plane observation, the principal plane is the same as the scattering plane. So, the angle of polarization is theoretically equal to 90° in the principal plane. In other words, the theoretical angle of 90° can be a reasonable value for the *AoP* of skylight in the solar principal plane, especially around the scanning angles of strongly polarized directions (e.g., around 90° angle from the sun). Therefore, the difference in *AoP* is equal to the angle between coordinate systems based on the instrument frame and the sky frame. That is, $\sigma = \chi - \chi' = \chi - 90^\circ$. Then, we can use Eq.(4.22) to recalculate the Stokes parameters Q and U , and deduce the angle of polarization *AoP*, the parallel and perpendicular polarized radiances I_l and I_r , as well as the linear depolarization ratio ρ in the sky frame.

4.3 Results

Results of the polarization parameters of skylight (including I , Q , U , *DoLP*, *AoP*, I_l , I_r , and ρ) are illustrated in this section. Only typical cloudless cases for different aerosol types are selected from sufficiently long observations within SONET, see Section 3.3. Results in the solar principal plane geometry are discussed in the Subsection 4.3.1. Results in the almucantar geometry

are presented in the Subsection 4.3.2.

4.3.1 Solar principal plane geometry

Five typical cases affected by haze polluted urban aerosol, rural aerosol, clean continental aerosol, mineral dust aerosol, and maritime aerosol are selected from some long-term observations in key areas of China within the SONET (i.e., at the “Beijing-RADI”, “ZhangyeHH”, “Lhasa”, “Minqin”, and “Zhoushan” sites, respectively). The instruments and locations of these sites have been listed in Tab. 3.3. Results of the polarization parameters measured in the solar principal plane geometry are given in Figs. 4.6-4.15. Tab. 4.1 provides information of the observing time and AOD on these five cases.

Table 4.1: Information on the cases of CE318-DP polarized principal plane observations in Figs. 4.6-4.15.

Cases	Stations	Instr.	Time (UTC)	AOD @440 nm
Haze polluted urban	Beijing-RADI	#350	07/12/2013 02:57	1.615
Rural	ZhangyeHH	#962	21/10/2012 02:18	0.217
Clean Continental	Lhasa	#966	18/12/2013 07:03	0.073
Mineral Dust	Minqin	#969	28/02/2012 04:18	2.929
Maritime	Zhoushan	#954	15/10/2012 01:52	0.946

Results of I , $DoLP$, I_l , I_r , and ρ observed in the solar principal plane in the five cases are illustrated in Figs. 4.6, 4.8, 4.10, 4.12, and 4.14. They are plotted as functions of scanning angles both in the solar and anti-solar directions. The scanning angles are from 95° to 265° with increments of 5° , see Tab. 3.2. Here, 180° represents zenith observation. Scanning angles exceeding 180° indicate the anti-solar direction, otherwise, the solar direction. I , I_l and I_r are plotted on a logarithmic scale. In general, $DoLP$ increase

4 Method of Stokes parameter derivation

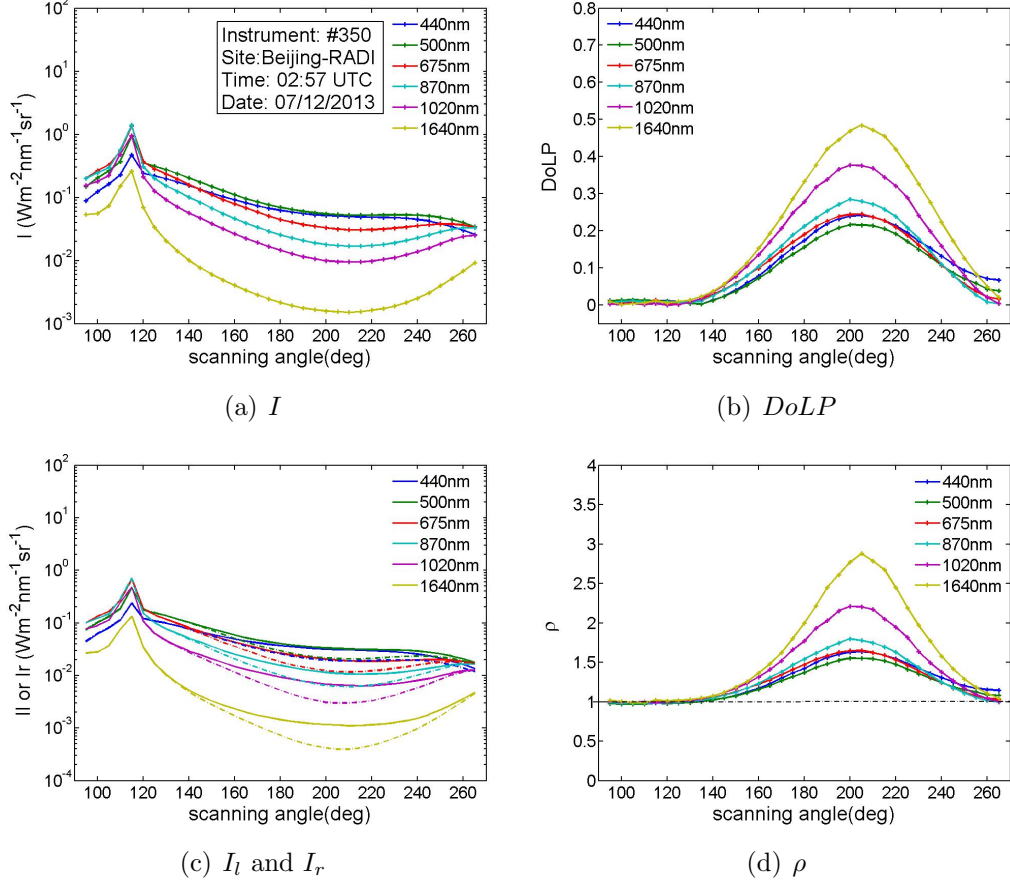


Figure 4.6: Results of the total radiance I (a), $DoLP$ (b), the parallel and perpendicular polarized radiances I_l (dash line) and I_r (solid line) (c), and the depolarization ratio ρ (d) for the haze polluted urban case in the solar principal plane geometry at the “Beijing-RADI” site.

4 Method of Stokes parameter derivation

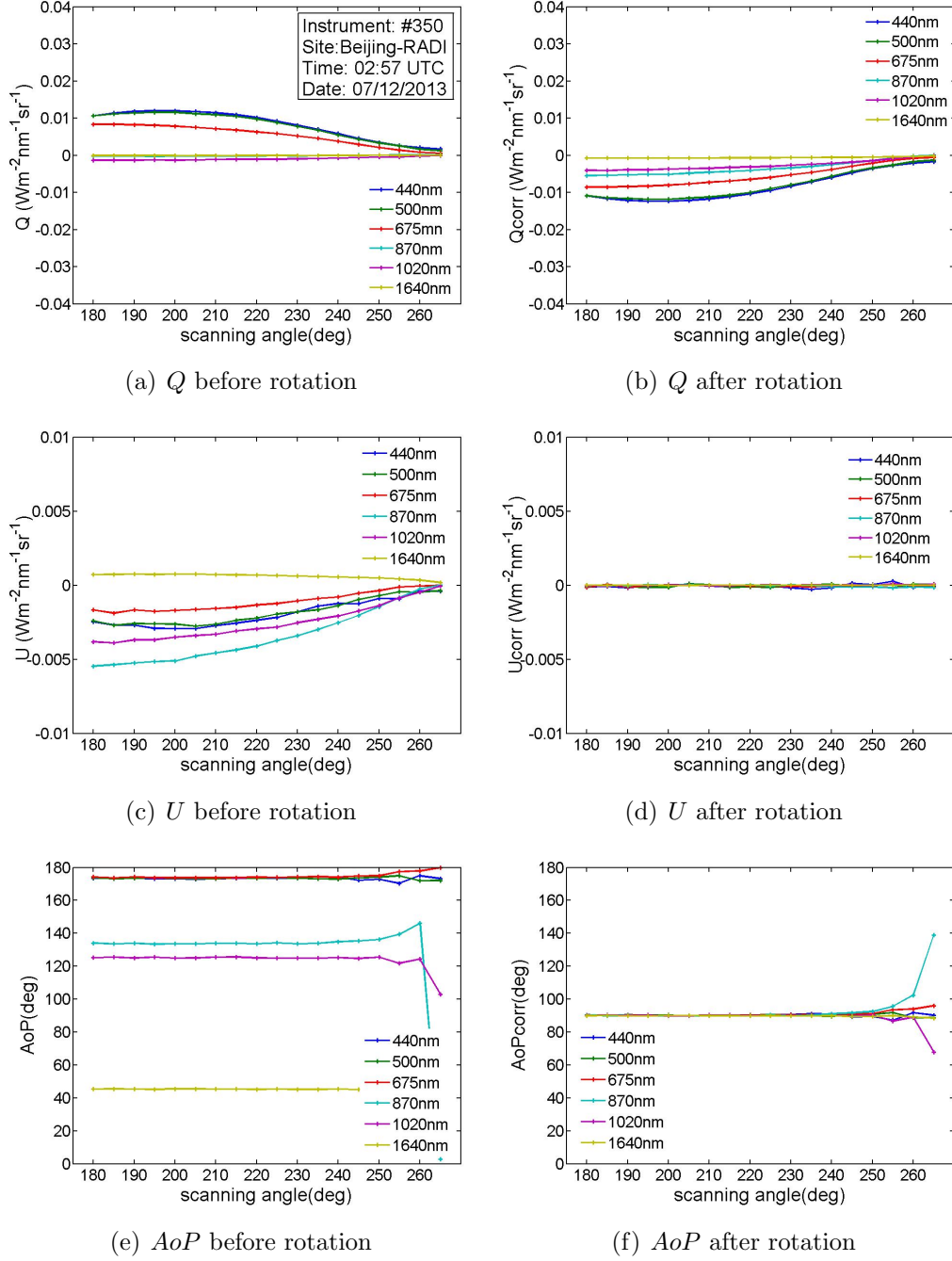


Figure 4.7: Results of the Stokes parameters Q (a,b), U (c,d), and AoP (e,f) for the haze polluted urban case in the solar principal plane geometry at the “Beijing-RADI” site.

4 Method of Stokes parameter derivation

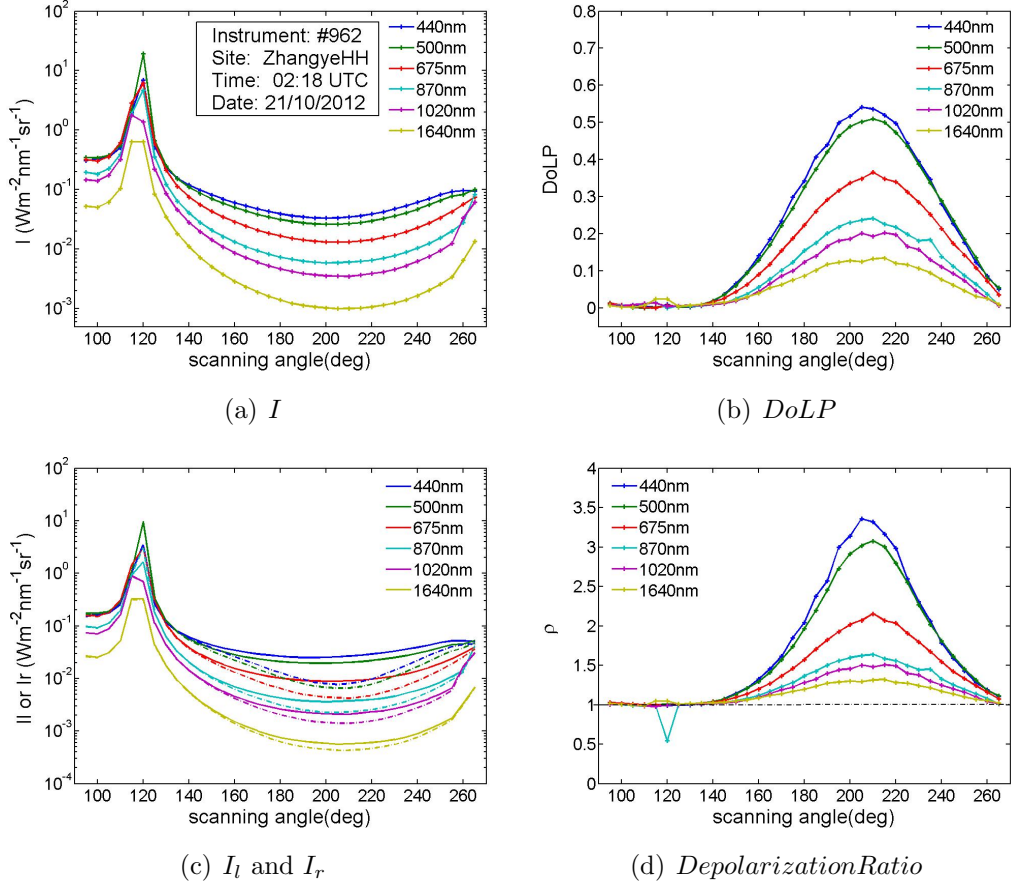


Figure 4.8: Results of the total radiance I (a), $DoLP$ (b), the parallel and perpendicular polarized radiances I_l (dash line) and I_r (solid line) (c), and the depolarization ratio ρ (d) for the rural case in the solar principal plane geometry at the "ZhangyeHH" site.

4 Method of Stokes parameter derivation

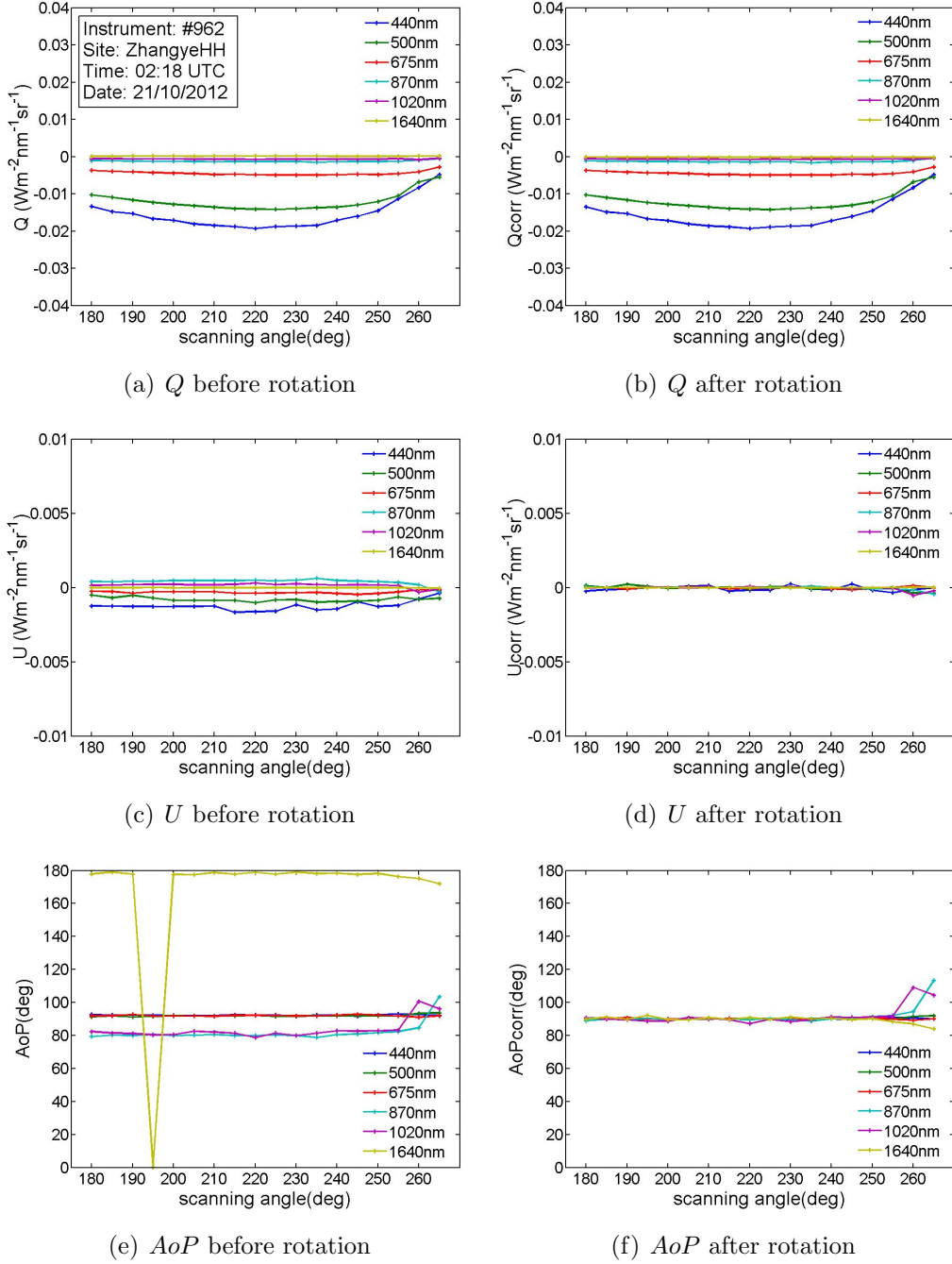


Figure 4.9: Results of the Stokes parameters Q (a,b), U (c,d), and AoP (e,f) for the rural case in the solar principal plane geometry at the “ZhangyeHH” site.

4 Method of Stokes parameter derivation

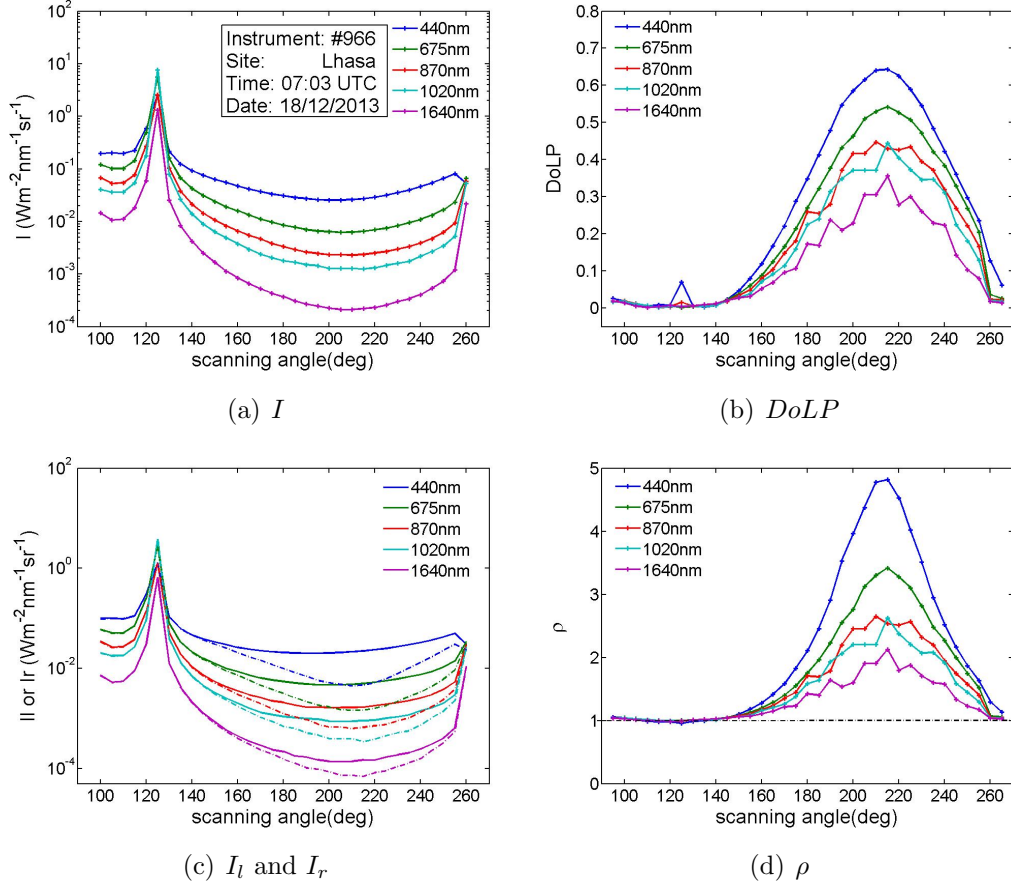


Figure 4.10: Results of the total radiance I (a), $DoLP$ (b), the parallel and perpendicular polarized radiances I_l (dash line) and I_r (solid line) (c), and the depolarization ratio ρ (d) for the clean continental case in the solar principal plane geometry at the “Lhasa” site.

4 Method of Stokes parameter derivation

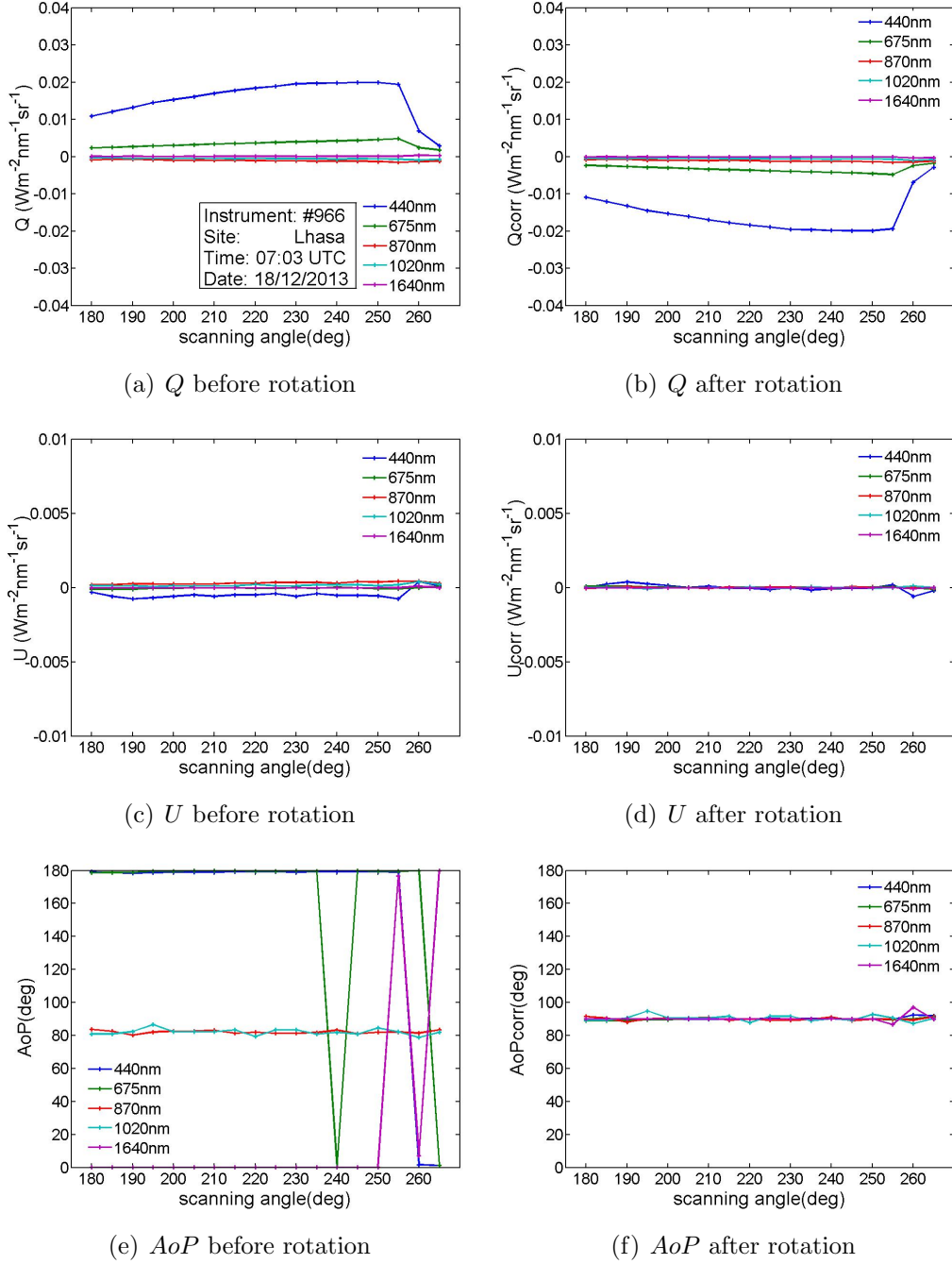


Figure 4.11: Results of the Stokes parameters Q (a,b), U (c,d), and AoP (e,f) for the clean continental case in the solar principal plane geometry at the “Lhasa” site.

4 Method of Stokes parameter derivation

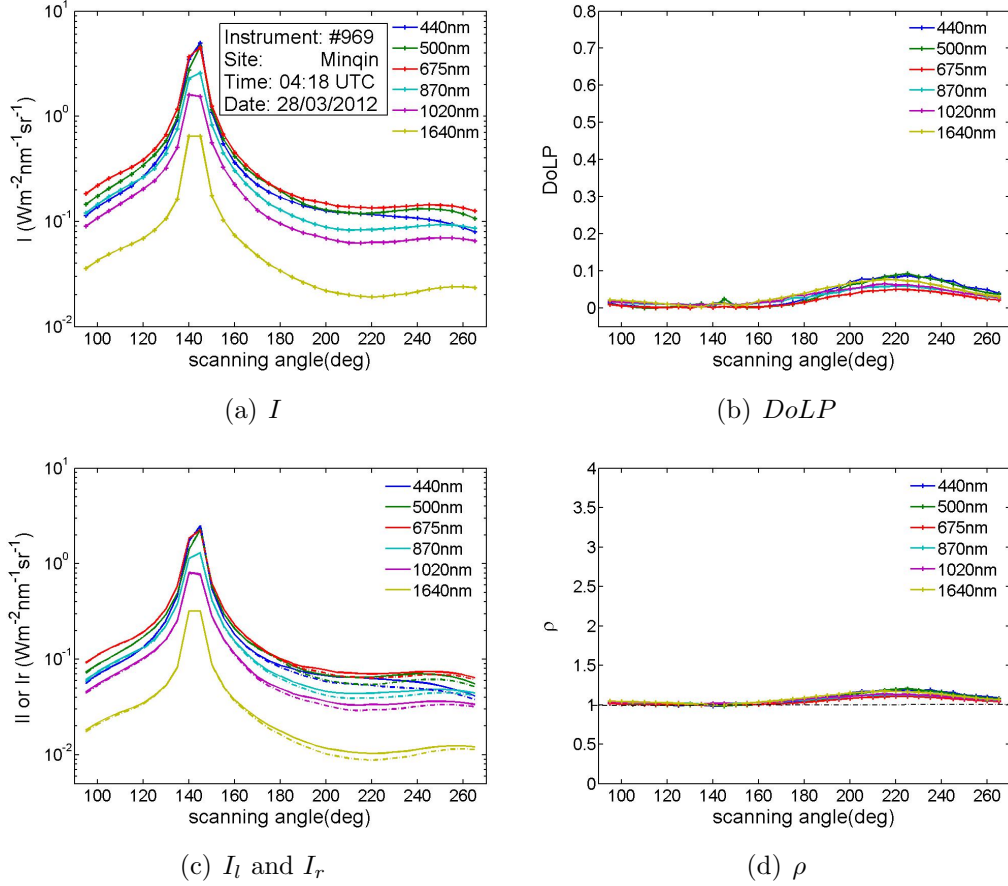


Figure 4.12: Results of the total radiance I (a), $DoLP$ (b), the parallel and perpendicular polarized radiances I_l (dash line) and I_r (solid line) (c), and the depolarization ratio ρ (d) for the mineral dust case in the solar principal plane geometry at the “Minqin” site.

4 Method of Stokes parameter derivation

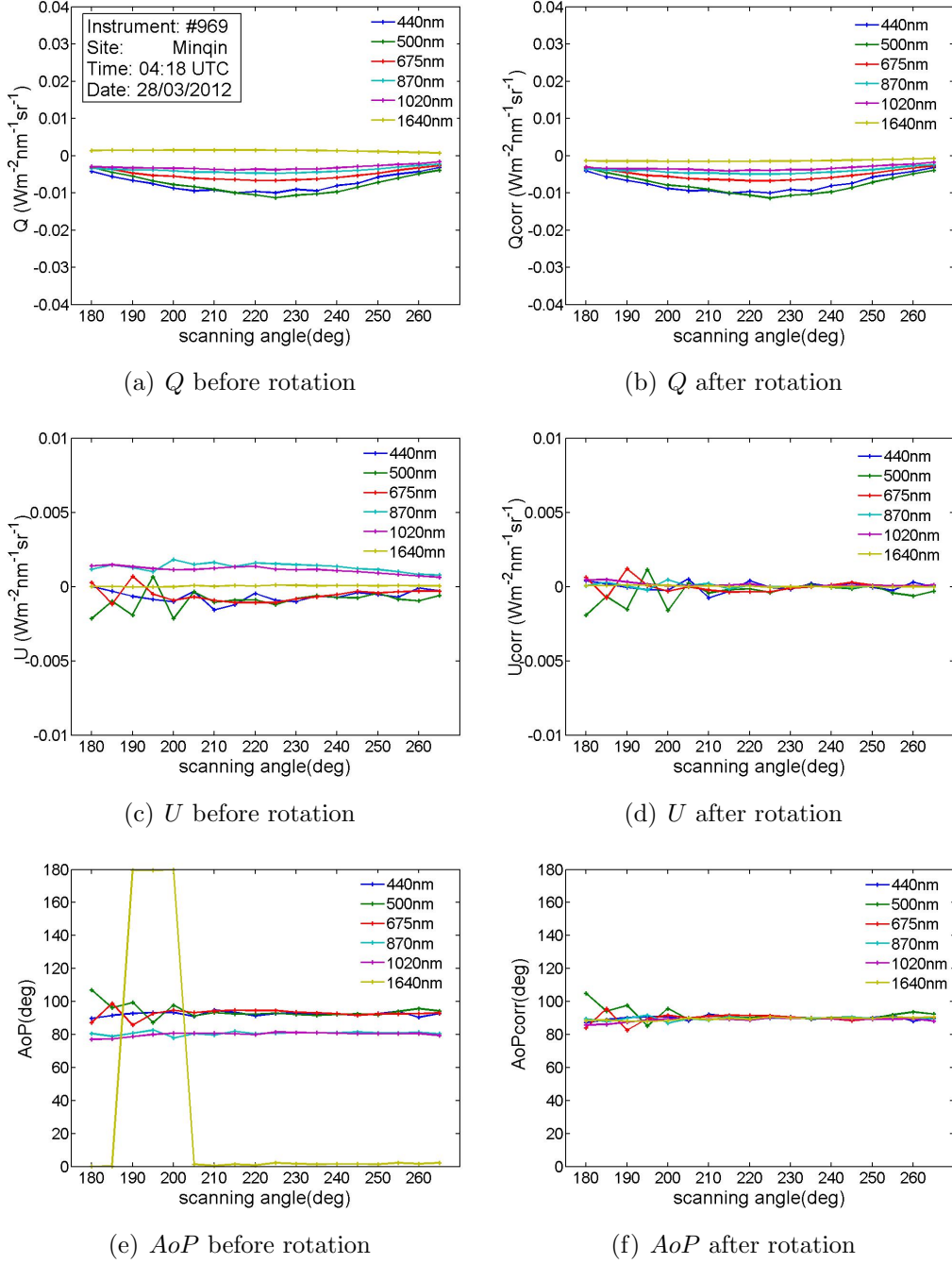


Figure 4.13: Results of the Stokes parameters Q (a,b), U (c,d), and AoP (e,f) for the mineral dust case in the solar principal plane geometry at the “Minqin” site.

4 Method of Stokes parameter derivation

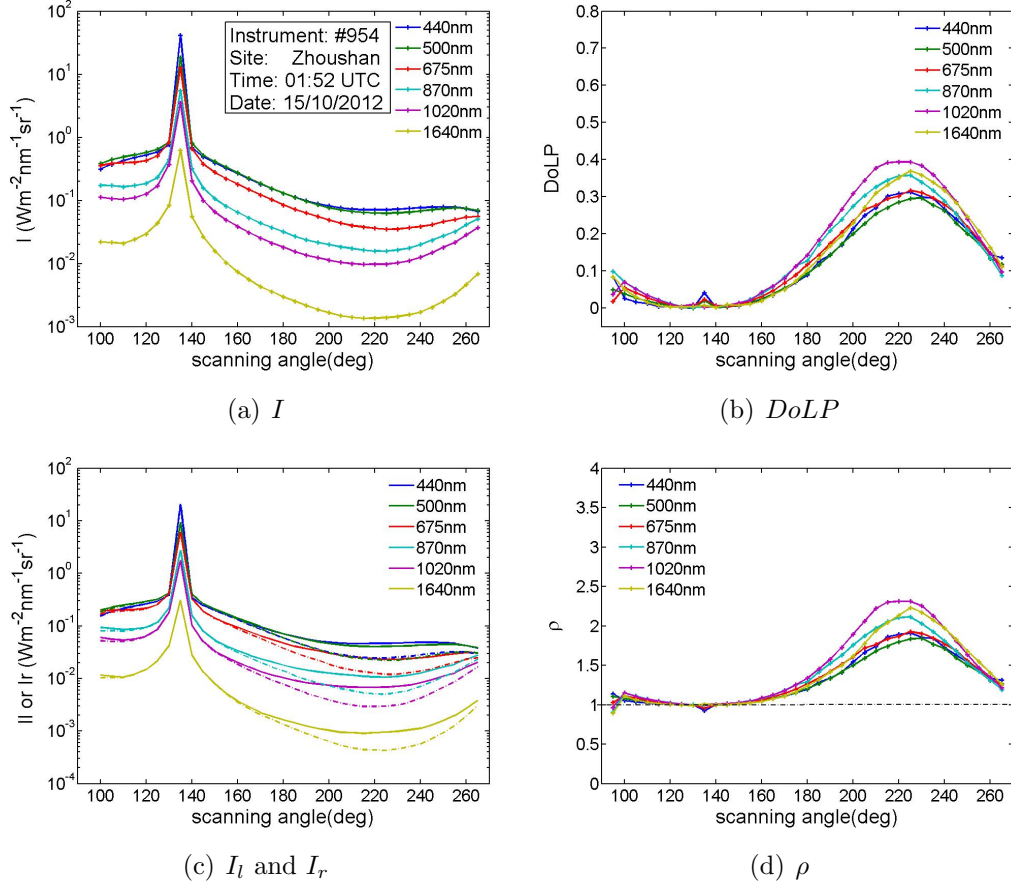


Figure 4.14: Results of the total radiance I (a), $DoLP$ (b), the parallel and perpendicular polarized radiances I_l (dash line) and I_r (solid line) (c), and the depolarization ratio ρ (d) for the Maritime case in the solar principal plane geometry at the "Zhoushan" site.

4 Method of Stokes parameter derivation

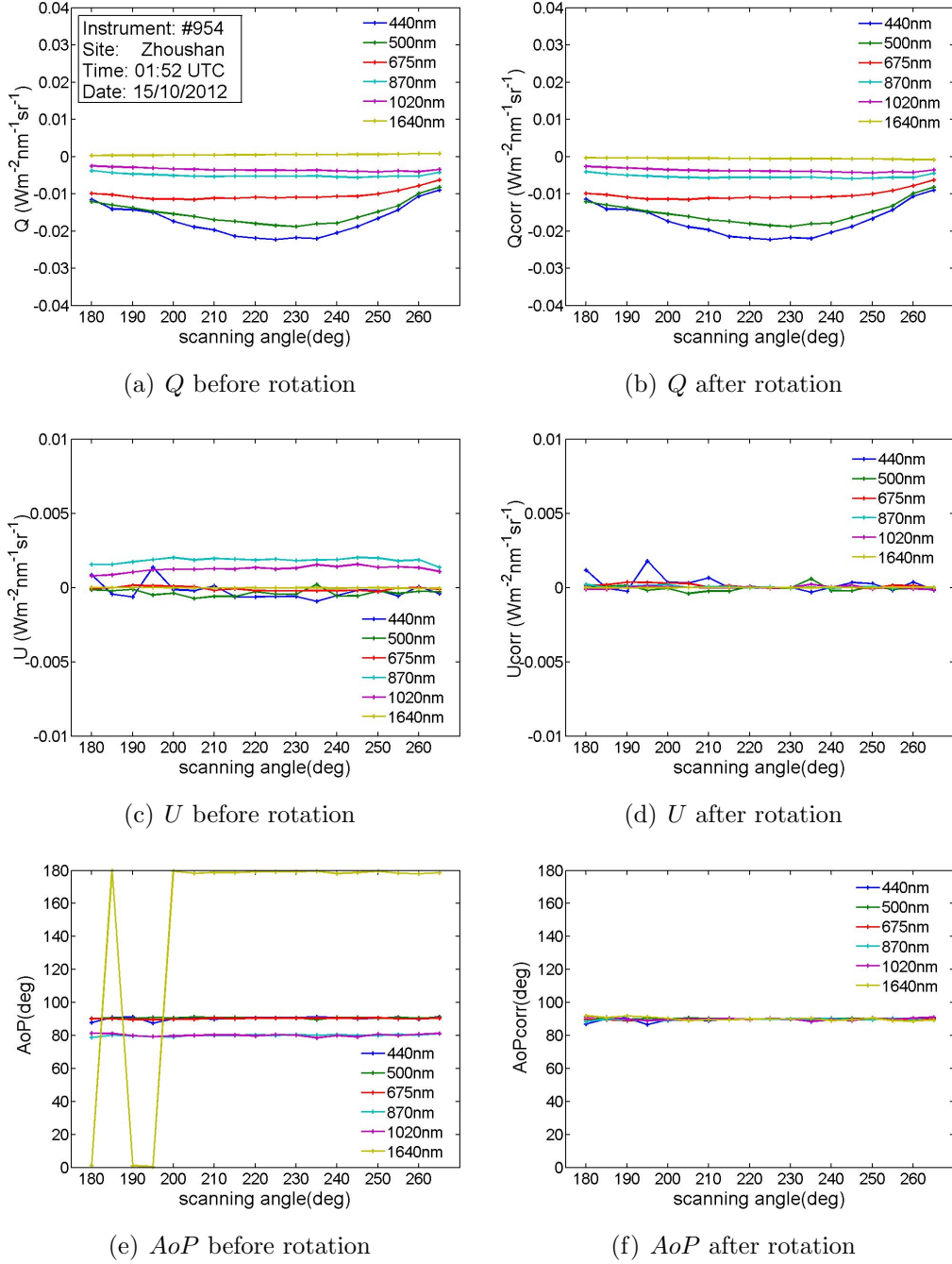


Figure 4.15: Results of the Stokes parameters Q (a,b), U (c,d), and AoP (e,f) for the Maritime case in the solar principal plane geometry at the “Zhoushan” site.

but I decrease with increasing scattering angles in the forward direction for all wavelengths, see panels (a) and (b) in Figs. 4.6, 4.8, 4.10, 4.12, and 4.14. Around the solar direction, we can get the maximum I and minor $DoLP$. The $DoLP$ reach maximum when scattering angles close to 90° for all wavelengths. $DoLP$ also change with wavelength, however, their spectral dependencies are inconsistent for different cases.

As discussed in Chapter 2, the parallel and perpendicular polarized radiances I_l and I_r are separated from the total radiance I knowing the Stokes parameter Q . ρ is derived from I_l and I_r . The results of them are depicted together with I and $DoLP$ for comparison. From panels (c) in Figs. 4.6, 4.8, 4.10, 4.12, and 4.14, it is obvious that I_l and I_r reveal similar features as the total radiances I . There are obvious differences between I_l and I_r . I_r is typically larger than I_l , especially at scattering angles close to 90° . That means, the skylight is rather perpendicular polarized in the solar principal planes for these cases. ρ in the solar principal plane show similar variations with wavelengths as $DoLP$, see panels (d) in these figures. Nevertheless, they have different meanings: $DoLP$ represents the ratio of the linear polarized radiance to the total radiance; while ρ denotes the ratio of the parallel polarized to the perpendicular polarized radiances.

Furthermore, it becomes visible that the degree of linear polarization in the anti-solar direction is generally larger than that in the solar direction, see panels (b) in Figs. 4.6, 4.8, 4.10, 4.12, and 4.14. That means skylight from the anti-solar half of sky is more polarized than that from the solar half. There are some outliers on $DoLP$ curves around the solar direction because of contamination of the direct sunlight that leads to complex linear polarizing in the solar direction. The orientation of polarization is more complex around this direction. Considering that Q , U , and AoP contain information not only on the degree but also on orientation of polarization of skylight, we only discuss results of Q , U , and AoP in the anti-solar direction, see Figs. 4.7, 4.9, 4.11, 4.13, and 4.15. The scanning angles change from 180° to 265° . Unlike $DoLP$ and I , the values of Q , U , and AoP depend on the reference plane and corresponding reference coordinate system. In these figures, results of Q , U , and AoP in the original coordinate system (\hat{l}_{ins} , \hat{r}_{ins} ,

\hat{z}_{ins}) based on the instrument frame (i.e., “before rotation”) are depicted in left three panels (a), (c), and (e), while those in the new coordinate system ($\hat{l}_{\text{sky}}, \hat{r}_{\text{sky}}, \hat{z}_{\text{sky}}$) based on the sky frame (i.e., “after rotation”) are shown in right three panels (b), (d), and (f).

From these figures, the Stokes parameter Q before rotation are larger or less than zero for different bands and sites. The results of U before rotation obviously deviate from zero for most wavelengths at all sites. AoP before rotation can imply relations between the band combinations and different sets of polarizer triplets. For instance, results of AoP at the “ZhangyeHH” site in Fig. 4.9 (e) imply that the bands of 440, 500, and 675 nm share one set of polarizer triplets, while the bands of 870, 1020, and 1640 nm share another set of polarizer triplets. Unlike the bands of 870 and 1020 nm which use silicon detectors, the band of 1640 nm employs an InGas detector. These two types of detectors correspond to two collimators and different parallel optical paths (Li et al., 2009). It leads to a 80° difference between the angles of polarization at 870, 1020 nm and that at 1640 nm, see Fig. 4.16. The values of AoP may be changed with installation of the optical sensor head to the arm of automated of CE318-DP. However, the relationships of different wavelength combinations are stable for the same instrument.

Comparing the left and right columns in Figs. 4.7, 4.9, 4.11, 4.13, and 4.15, it is evident that differences exist in the curves of Q , U and AoP before and after rotations. As discussed above, the right-handed Cartesian reference coordinate system ($\hat{l}_{\text{sky}}, \hat{r}_{\text{sky}}, \hat{z}_{\text{sky}}$) based on the sky frame adopts the meridian plane as reference plane, which is the same as the principal plane for the solar principal plane observation geometry. The direction of skylight polarization in nature should be perpendicular to the principal plane and along the \hat{r}_{sky} -axis. According to convention, the sign of Q is negative, U is equal to zero, and AoP is equal to 90° within the sky frame, see Fig. 4.5. From panels (b), (d), and (f) in Figs. 4.7, 4.9, 4.11, 4.13, and 4.15, it is obvious that Q are less than zero after reference coordinate system rotations; the absolute values of U are very small and close to zero; and AoP are almost all equal to 90° for different wavelengths. These features are consistent with the polarization pattern of skylight in nature (Liu and Voss, 1997; Smith, 2007).

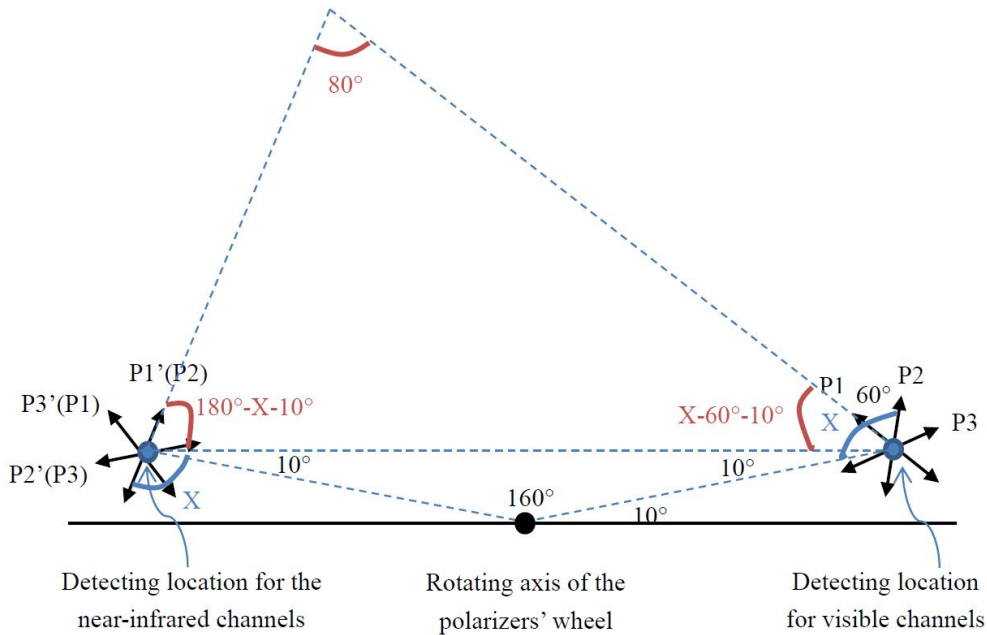


Figure 4.16: Schematic diagram of a 80° difference between the angles of polarization at 870, 1020 nm and at 1640 nm. Black point represents the rotating axis of the CE318-DP polarizers' wheel; Blue points denote the detecting location for the UV-visible channels (e.g., 340, 380, 440, 500, 675, 870, and 1020 nm) and the detecting location for the near-infrared channels (e.g., 1640 nm). Note that the channels at 870, 1020, and 1640 nm employ the same set of polarizer triplets, but the sequence of measurements for the channels at 870 and 1020 nm (P1 to P2 to P3) differs from that for the channel at 1640 nm (P2 to P3 to P1).

In the following, results of skylight polarization in these five cases are discussed in detail:

(A) haze polluted urban case at the “Beijing-RADI” site

The polarized skylight observation on 7 December, 2013 is discussed as a first case. It was a typical haze polluted day in Beijing with AOD at 440 nm steadily increasing from 1 in the morning (00:35 UTC) to 2.24 in the evening (06:59 UTC), see Fig. 4.17. At the observation time (02:57 UTC), the AOD at 440 nm was about 1.62. According to the SONET retrieval (corresponding

to the level 1.5 of the AERONET), this case was dominated by fine spherical aerosol particles with the total effective radius of $0.313 \mu\text{m}$ and the sphericity parameter (i.e., the fraction of spherical particles) of 99 % .

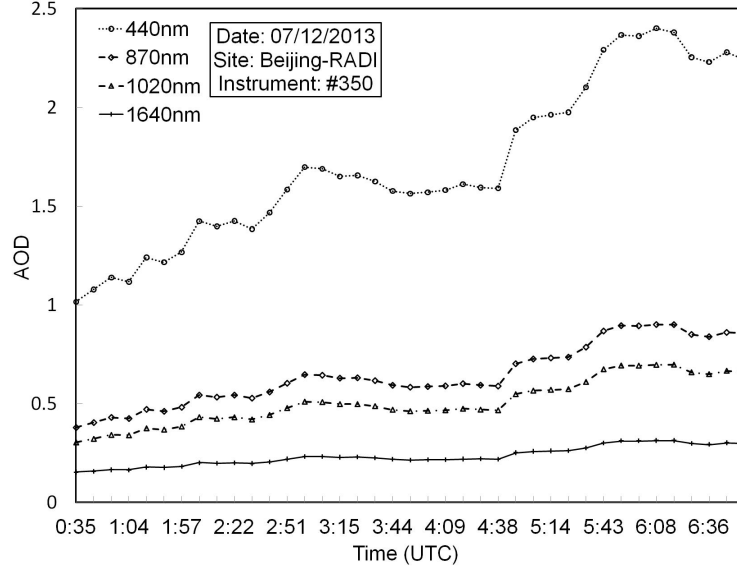


Figure 4.17: Aerosol optical depth derived from the CE318-DP#350 sun measurements on December 7, 2013 following AERONET level 1.0 data criteria (Li et al., 2014a).

From Fig. 4.6, the angle of incident light is about 115° . The maximum I and minor $DoLP$ are measured around this direction for all wavelengths. The neutral point where $DoLP$ is equal to zero can be found around 130° . The $DoLP$ increases as the scattering angle increases in the forward direction and reaches a peak at the scanning angle around 205° (i.e., the scattering angle is around 90°). The maximum $DoLP$ is 0.48 at 1640 nm. In contrary, I decreases as the scattering angle increases in the forward direction. Both $DoLP$ and I are wavelength-dependent, but they generally show opposite tendencies. The longer the wavelengths, the higher the maximum $DoLP$ values and the lower the minimum I values. $DoLP$ at long wavelengths (such as 1640 nm) are larger than at short wavelengths (such as 440 nm). This feature can frequently be found in hazy sky conditions. That could be due to different depolarizing effects of multiple scattering for different wavelengths. The relationship between the wavelength-variations of these parameters and

the aerosol properties should be studied in further investigations.

I_l and I_r in Fig. 4.6 have similar wavelength-dependence as the total radiance I . The longer the wavelengths, the lower the minimum I_l and I_r values. Exceptions at 440 and 500 nm are likely due to inaccurate polarization calibration coefficients for these two short wavelengths. Around the solar direction (i.e., the scanning angles from 95° to 135°), the parallel polarized radiance I_l is very close to the perpendicular polarized radiance I_r . However, I_r is much larger than I_l at scanning angles from 140° to 265° , especially around the scanning angle of 205° . It is evident that the polarized component of Mie scattering, which is dominated by fine spherical aerosol particles in this haze polluted urban case, is perpendicular to the scattering plane, see Section 2.2. From the results of depolarization ratio ρ , it is obvious that ρ for all wavelengths are larger than 1 in the principal plane. That means, the perpendicular polarized component are larger than the parallel one. The skylight in general is polarized perpendicular to the principal plane.

From panels (a), (c), and (e) in Fig. 4.7, Q is larger than zero at 440, 500, and 675 nm at the scanning angles from 180° to 265° . However, Q may be larger or less than zero at 870, 1020, and 1640 nm at different scanning angles. U is larger than zero at 1640 nm but less than zero at other wavelengths. AoP deviates from 90° at all wavelengths before the reference coordinate system rotation. After rotation, Q are less than zero; U are almost equal to zero; and AoP are close to 90° for all wavelengths, see panels (b), (d), and (f) in Fig. 4.7. The rotation angles are 83° , 44° , and 35° for the three sets of triplet polarizers. AoP deviates from 90° around the scanning angle of 265° in Fig. 4.7 (f), which indicates another neutral point in the anti-solar meridian (Horváth and Varjú, 2004).

(B) rural case at the “ZhangyeHH” site

The “ZhangyeHH” site is located in representative rural area of the Heihe river basin, Shaanxi, China. The polarized skylight observations performed on 21 October, 2012 are adopted in this study. The AOD at 440 nm was about 0.22 at the viewing time of 02:18 UTC. According to the SONET retrieval, it was a typical rural case dominated by nonspherical coarse mode particles

with total effective radius of 1.63 μm and sphericity parameter about 1 %.

From panels (a) and (b) in Fig. 4.8, the maximum I and minor $DoLP$ around the scanning angle of 117° (i.e., the solar direction) are derived in this case. The $DoLP$ reach maximum at scanning angle around 207° (i.e., 90° scattering angle) for all wavelengths. The maximum $DoLP$ is 0.54 at 440 nm which is larger than the maximum $DoLP$ in the haze polluted urban case (i.e., 0.48 at 1640 nm). This is likely due to depolarizing effects of multiple scattering for the skylight with abundant aerosol particles in the heavy haze polluted case. The wavelength-sensitivity of $DoLP$ is opposite to that in the hazy urban case. The longer the wavelengths, the lower the maximum $DoLP$ values. On the contrary, I show a similar wavelength-dependence as the hazy urban case. The longer the wavelengths, the lower the minimum I values. I_l and I_r in Fig. 4.8 (c) also show similar wavelength-dependence as the total radiance I . Unlike in the hazy urban case, the shorter the wavelengths, the larger the differences between I_l and I_r in this rural case. From Fig. 4.8 (d), it is obvious that ρ for all wavelengths are generally larger than 1 except around the solar direction. That means skylight scattered by nonspherical coarse aerosol particles in this rural case are more perpendicular polarized, especially for short wavelengths.

From panels (a) and (b) in Fig. 4.9, there is no significant change in Q after the reference coordinate system rotation because Q are almost all less than zero for different wavelengths in the instrument frame. Compared with the results before rotation, U are more close to zero after rotation for different wavelengths, see panels (c) and (d) in Fig. 4.9. Two sets of triplet polarizers (i.e., 440, 500, and 675 nm; 870, 1020, and 1640 nm) are found from AoP before rotation in Fig. 4.9 (e). The rotation angles are about 2° and -9° for the two sets of triplet polarizers. The 80° difference between AoP at 870, 1020 nm and that at 1640 nm has been discussed above. The results corresponding to another set of triplet polarizers for 340 and 380 nm are not illustrated here. A jump point at 195° in the AoP curve of 1640 nm is because U is exactly equal to zero at this angle but slightly less than zero at other scanning angles with Q being larger than zero at all scanning angles, see Tab. 2.1. AoP deviates from 90° around the scanning angle of

265° in Fig. 4.9 (f) also indicating the Arago neutral point in the anti-solar meridian.

(C) clean continental case at the “Lhasa” site

The “Lhasa” site plays an important role in the SONET because this site is located in the Tibet Plateau with altitude of 3690 m. It also fills in the blank of polarized observations in Southwest China. A typical clean continental case observed on 18 December, 2013 is chosen in this study. In this case, the AOD at 440 nm was only 0.073 at 07:03 UTC, which was obviously less than that in the rural case (i.e., the AOD at 440 nm was about 0.22). According to the SONET retrieval, the clean continental case was also dominated by coarse nonspherical aerosol particles with the total effective radius of 0.966 μm and the sphericity parameter of 0.12 %.

From Fig. 4.10, the angle of incident light is about 124°. Two neutral points can be found around the scanning angles of 115° and 130°. *DoLP* reaches maximum around the scanning angle of 214°. Comparing Fig. 4.10 with Fig. 4.8, the maximum values of *DoLP* in the clean continental case are all larger than those in the rural case for corresponding wavelengths since lower AOD value of the skylight in the clean continental case generating less depolarization effects by multiple scattering. However, *I* in the clean continental case are less than those in the rural case. Small digital numbers, which are corresponding to low radiances in the polarized channels at long wavelengths lead to the roughness of *DoLP* curves at 870, 1020, and 1640 nm in the clean continental case, see Fig. 4.10 (b). Compared with the rural case, differences between I_r and I_l at the 90° scattering angle are more dramatic in the clean continental case. Namely, the skylight is more perpendicular polarized. From Fig. 4.10 (d), it is obvious that the maximum I_r can even be 3.8 times higher than that of I_l at 440 nm.

From Fig. 4.11, *Q* and *U* at short wavelengths (e.g., 440 nm) have prominent changes after rotation. Two sets of triplet polarizers (i.e., 440 and 675 nm; 870, 1020, and 1640 nm) can be observed in Fig. 4.11 (e). The rotation angles are about 89.5° and −8° for these two sets of triplet polarizers. The results regarding to another set of triplet polarizers are not given here. The

jump points at 260° and 265° in the *AoP* curve of 440 nm, as well as at 240° and 265° in the *AoP* curve of 675 nm are because the values of Q and U before rotation are very close to zero at these angles. The jump points at 255° and 265° in the *AoP* curve of 1640 nm are caused by the positive Q and negative U at these angles (U at other scanning angles are all equal to zero), see Tab. 2.1.

(D) mineral dust case at the “Minqin” site

The “Minqin” site is surrounded by the Tengger desert and the Badain Jaran desert. A typical mineral dust case observed on 28 March, 2012 is analyzed. In this case, the AOD at 440 nm was up to 2.929 at 04:18 UTC. There was no retrieval of aerosol microphysical parameters because of the dust blowing. But it could be considered as dominated by coarse nonspherical particles.

From Fig. 4.12, *DoLP* is very low and have no obvious wavelength-variation behaviors in comparison with the clean continental and the rural cases. The maximum *DoLP* is only 0.09 around the scanning angle of 232.4° (i.e., the 90° scattering angle). The low *DoLP* in the mineral dust sky condition could be due to more depolarization effects of the multiple scattering by abundant dust particles in the atmosphere. There are no obvious differences between I_l and I_r , meanwhile, ρ are close to 1 for all wavelengths, see Fig. 4.12 (c) and (d). It means that the skylight in the solar principal plane is nearly unpolarized.

From Fig. 4.13, Q at 1640 nm changes from positive to negative after the reference coordinate system rotation. U is more close to zero after rotation than before. The rotation angles in this case are about 2.5° and -8.8° for the two sets of triplet polarizers separately corresponding to 440, 500, 675 nm, and 870, 1020, 1640 nm, see Fig. 4.13 (e). The jump points from 190° to 200° in the *AoP* curve of 1640 nm are caused by the negative U at these angles, see Tab. 2.1.

(E) maritime case at the “Zhoushan” site

The “Zhoushan” site is located in the Zhoushan archipelago, East China

sea. A typical maritime case observed on 15 October, 2012 is selected in this study. AOD at 440 nm was 0.946 at 01:52 UTC. It was a moderate AOD comparing with those in clear sky conditions (e.g., in the clean continental and the rural cases) and in unclear sky conditions (e.g., in the haze polluted urban and the mineral dust cases). According to the inversion results from almucantar measurements, the total effective radius was 0.361 μm and the sphericity parameter was about 69%. This case was dominated by the submicron fine spherical aerosol particles (Li et al., 2014b).

From Fig. 4.14, the angle of incident light is about 134° . *DoLP* in this case show different wavelength-dependence: neither monotonously increases nor decreases as wavelength increases. That could be caused by submicron size of the maritime aerosol particles. The maximum *DoLP* is 0.39 at 1020 nm. This value is also between the maximum values in the clear and unclear sky conditions. I_r is obviously larger than I_l , particularly around the scanning angle of 224° (i.e., the 90° scattering angle).

From the results of *AoP* before rotation, it is evident that the channels of 440, 500, 675 nm and 870, 1020, 1640 nm share two sets of triplet polarizers, see Fig. 4.15 (e). The rotation angles are about 0.6° and -9.8° , respectively. The jump points at 180° , 190° , and 195° in the *AoP* curve of 1640 nm (i.e., *AoP* are close to 0° at these scanning angles) are due to the positive U at these angles with positive Q at all scanning angle in this channel, see Tab. 2.1.

In summary, the Stokes parameter U and the angle of polarization after reference coordinate system rotation have no significant variation characteristics in the solar principal plane geometry, while results of the Stokes parameter Q after rotation change dramatically, see panels (b), (d), and (f) in Figs. 4.7, 4.9, 4.11, 4.13, and 4.15. Then, Q is recommended to analyze the influences of different aerosol microphysical properties and chemical components on the polarized skylight in the solar principal plane. When Q is known, the parallel and perpendicular polarized radiances I_l and I_r , as well as the depolarization ratio ρ are obtained. They can provide unique information on skylight polarization.

4.3.2 Almucantar geometry

The Polarized ALMucantar (ALMP) scenario is a test function for the CE318-DP at present. It is only available for the CE318-DP#350 at the “Beijing-RADI” site within SONET. Two typical cloudless polarized almucantar measurements in a heavy haze polluted sky (02:36 UTC on 7 December, 2013) and a clear sky (06:25 UTC on 9 December, 2013) are analyzed in this subsection. The atmospheric conditions for these two cases are summarized in Tab. 4.2. The AOD at 440 nm was 1.47 for the heavy haze polluted sky, while it was only 0.12 for the clear sky.

Table 4.2: Atmospheric conditions for the skylight polarization measurements in the polarized almucantar geometry in haze polluted urban and clear cases shown in Figs. 4.18 to 4.21.

Parameter	Haze polluted case (7 December, 2013 02:36 UTC)	Clear case (9 December, 2013 06:25 UTC)
Solar Zenith Angle ($^{\circ}$)	66	70.6
Temperature ($^{\circ}\text{C}$)	3.5	5.9
Humidity (%)	53.3	20.6
Barometric Pressure (hPa)	1013.3	1013.8
Wind Speed (m/s)	1	6
AOD@440 nm	1.47	0.12

Figs. 4.18 and 4.20 illustrate results of the total radiance I , $DoLP$, the parallel and perpendicular polarized radiances I_l and I_r , as well as the depolarization ratio ρ as functions of Relative Azimuthal Angle (RAA) in the heavy haze polluted sky and the clear sky, respectively. It is clear that all these results are symmetric with respect to the principal plane (i.e., $RAA = 180^{\circ}$). I , I_l and I_r reach peak values close to the solar direction (i.e., $RAA =$

4 Method of Stokes parameter derivation

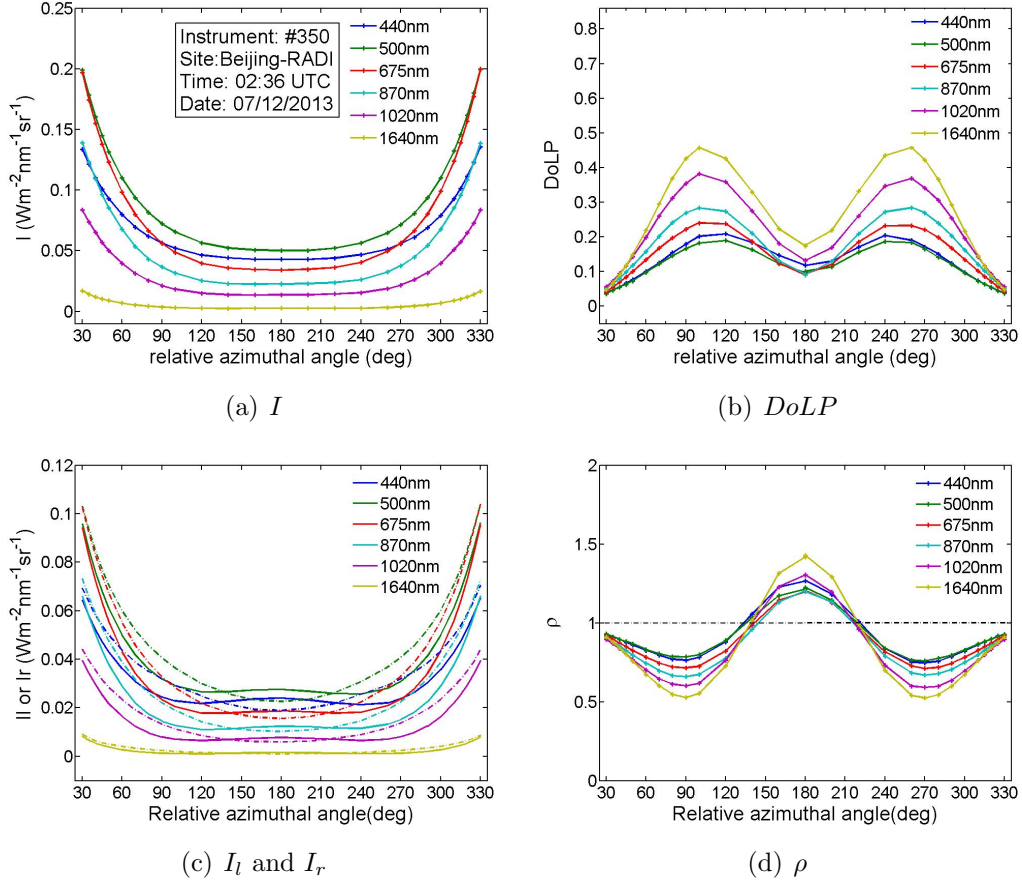


Figure 4.18: Results of the total radiance I (a), $DoLP$ (b), the parallel and perpendicular polarized radiances I_l (dash line) and I_r (solid line) (c), and the depolarization ratio ρ (d) for the haze polluted urban case in the polarized almucantar geometry at the "Beijing-RADI" site.

4 Method of Stokes parameter derivation

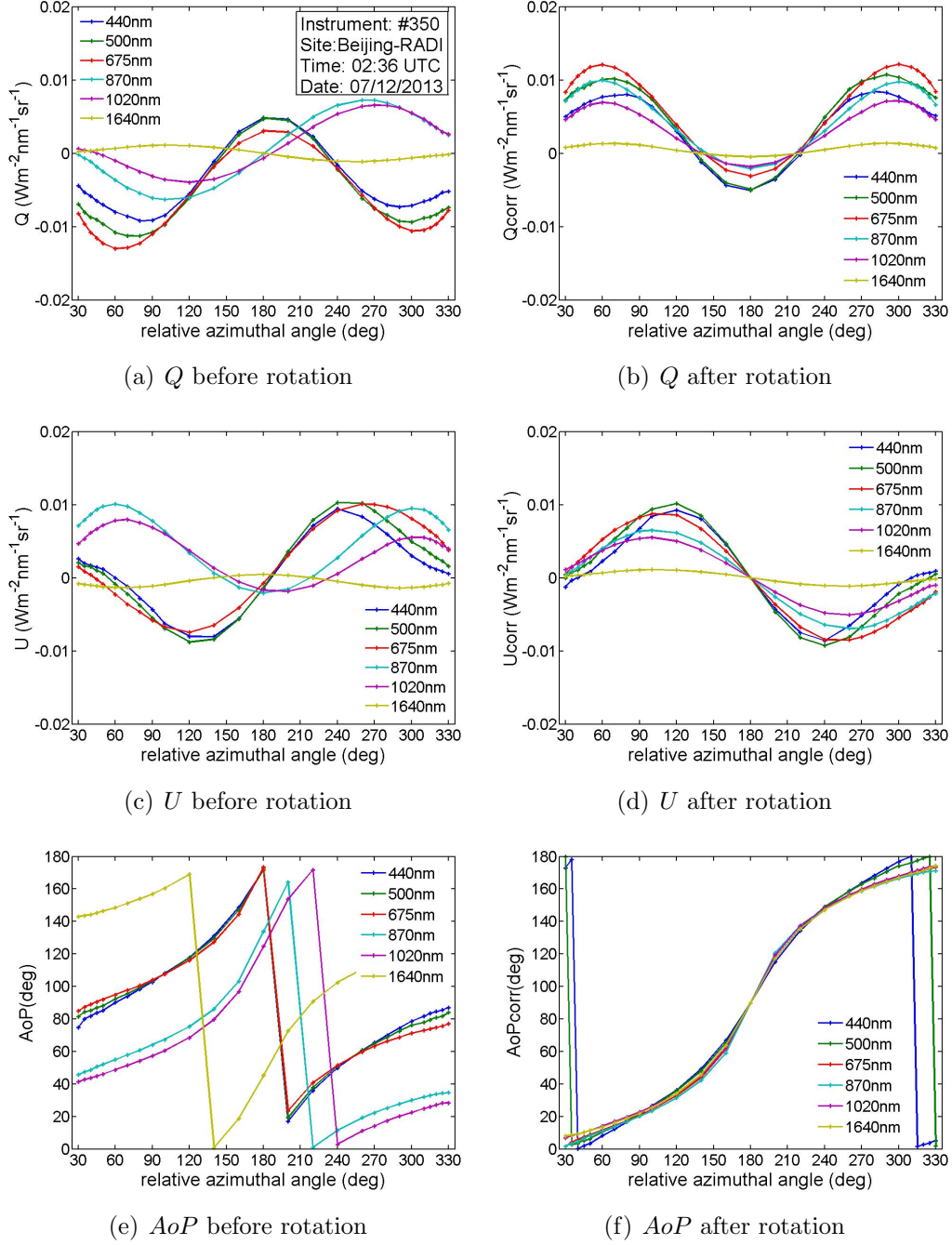


Figure 4.19: Results of the Stokes parameters Q (a,b), U (c,d), and AoP (e,f) for the haze polluted urban case in the polarized almucantar geometry at the “Beijing-RADI” site.

4 Method of Stokes parameter derivation

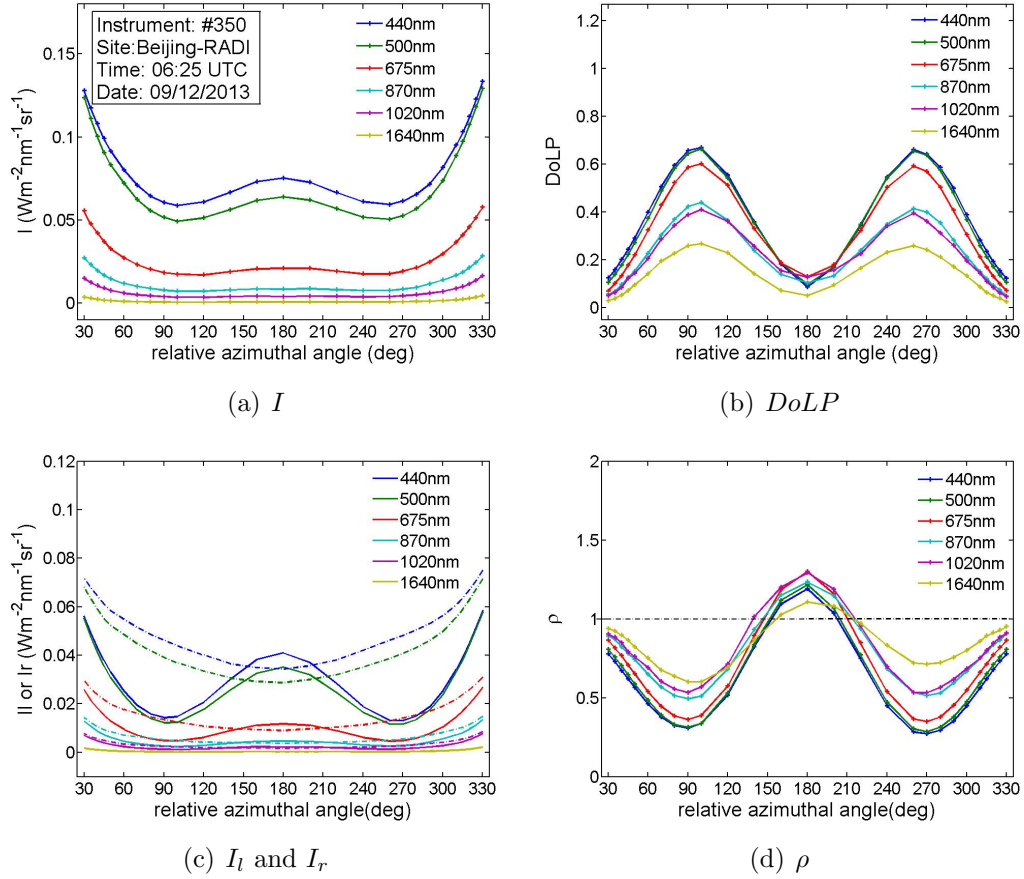


Figure 4.20: Results of the total radiance I (a), $DoLP$ (b), the parallel and perpendicular polarized radiances I_l (dash line) and I_r (solid line) (c), and the depolarization ratio ρ (d) for the clear case in the polarized almucantar geometry at the "Beijing-RADI" site.

4 Method of Stokes parameter derivation

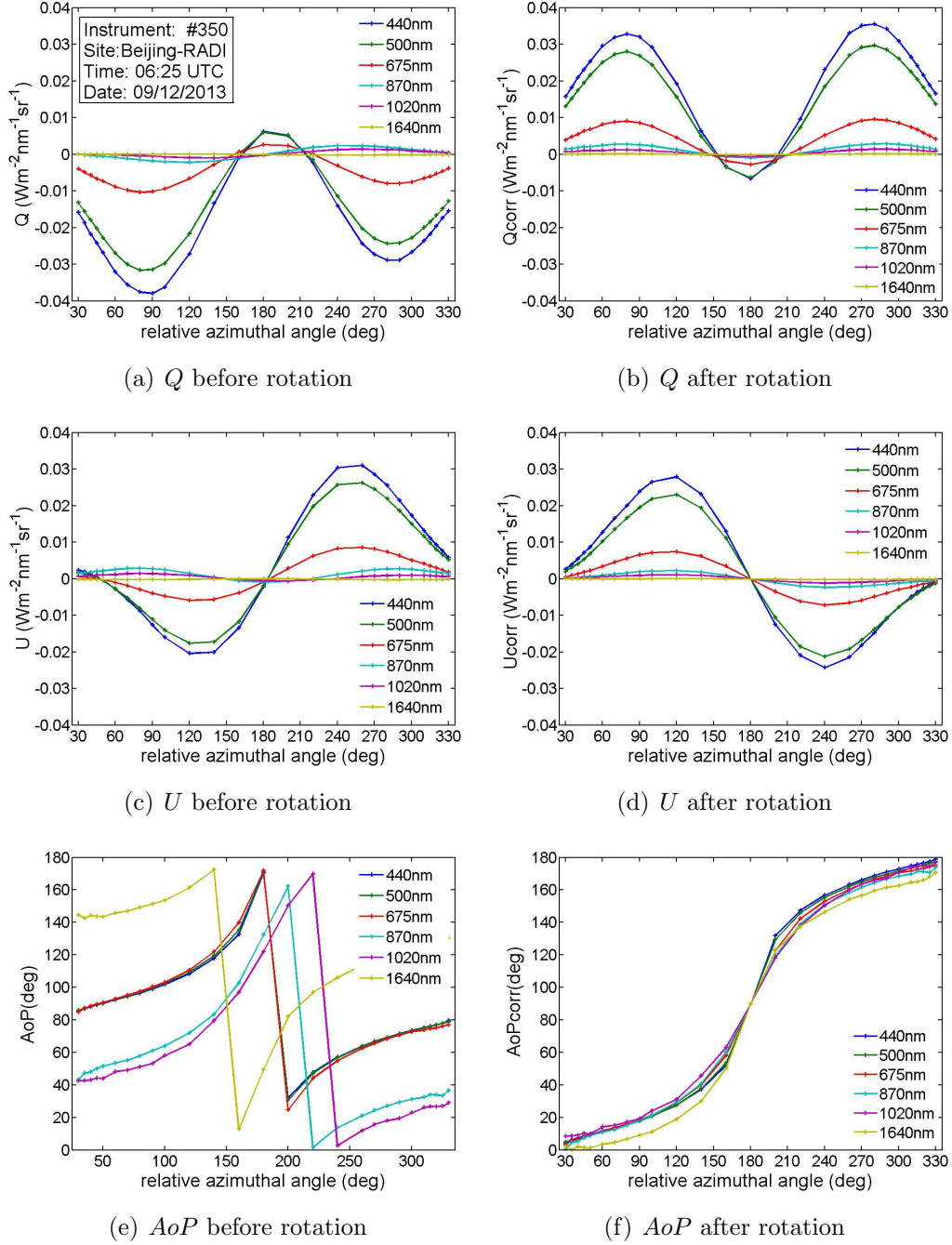


Figure 4.21: Results of the Stokes parameters Q (a,b), U (c,d), and AoP (e,f) for the clear case in the polarized almucantar geometry at the "Beijing-RADI" site.

30° , 330°). The variations of I and I_r with RAA are similar. Namely, I and I_r keep steady or fell slowly first and then rise rapidly with RAA away from 180° (i.e., the principal plane). But I_l shows different variation with RAA . It simply increases with RAA deviating from 180° . The results of $DoLP$ reach two peaks at scattering angle of 90° for all wavelengths in the left and right almucantar plane, respectively. They reach valleys in the principal plane (i.e., $RAA = 180^\circ$) or close to the solar direction (i.e., $RAA = 30^\circ$, 330°). Unlike ρ in the principal plane, which shows similar sensitivity with the scanning angle as the $DoLP$, ρ in the almucantar geometry shows opposite feature to the $DoLP$. ρ at all wavelengths are larger than 1 and reach maximum around the principal plane (i.e., $RAA = 180^\circ$). But they are less than 1 at most other relative azimuthal angles. That means, the skylight is perpendicular polarized around the principal plane, but is parallel polarized in other observing directions in the almucantar plane. ρ at all wavelengths are equal to 1 around the relative azimuthal angles of 140° and 220° in the haze polluted case, see Fig. 4.18. Namely, skylight is unpolarized around these two angles. Similarly, ρ are equal to 1 around the relative azimuthal angles of 150° and 210° in the clear case, but with more obvious differences among wavelengths, see Fig. 4.20.

Figs. 4.19 and 4.21 give results of the Stokes parameters Q , U , and AoP as functions of the relative azimuthal angle in the heavy haze polluted sky and the clear sky, respectively. Compared with the results in the solar principal plane geometry, Q , U , and AoP in the almucantar geometry can present more variation features of skylight. The relationships among AoP and signs of the Stokes parameters Q and U discussed in Subsection 2.1.2 can be clearly seen after rotation of the reference coordinate system from the instrument frame to the sky frame. For example, AoP is equal to 90° when $Q < 0$ and $U = 0$ at the RAA of 180° . After rotation, Q is symmetric but U is anti-symmetric with respect to the principal plane. AoP appears almost monotonous variation as RAA increases. When RAA is equal to 180° that indicates the solar principal plane, Q reaches the minimum; U is nearly equal to zero; and AoP is 90° .

Q reaches the maximum when RAA is around 70° or 290° , and U reaches

the maximum or the minimum when RAA is around 110° or 250° in the haze polluted urban case, see Fig. 4.19 (b) and (d). Q reaches the maximum when RAA is around 80° or 280° , while U reaches the maximum or the minimum when RAA is around 120° or 240° in the clear case, see Fig. 4.21 (b) and (d). In general, the peak values of Q and U vary with wavelength, and the spectral discrepancies of Q or U are larger at the angles where they reach higher values. Simulations have also shown that the extreme values of Q and U vary with different aerosol particle size, shape, real and imaginary parts of the complex refractive index. Nevertheless, the angles taking the extreme values are almost unchanged (Li et al., 2013). So it is recommended to utilize the polarization measurements at these angles in the almucantar geometry to get information on different aerosol properties. From Figs. 4.19 (f) and 4.21 (f), it is clear that AoP change little with wavelength at most relative azimuthal angles, especially in the solar principal plane (i.e., $RAA = 180^\circ$).

Furthermore, the discrepancies between results of the haze polluted and the clear urban cases in the almucantar geometry are discussed in this subsection. Comparing Figs. 4.18 (b) and 4.20 (b), it could be found that the maximum $DoLP$ in the haze polluted urban case is less than that in the clear case. This can be explained by more depolarization effects of the multiple scattering in the heavy haze polluted sky. There are also different wavelength-variation behaviors between the clear and haze polluted cases. In the clear sky, the values of $DoLP$ at long wavelengths are less than those at short wavelengths at most relative azimuthal angles, except around the principal plane (i.e., RAA around 180°). On the contrary, the values of $DoLP$ at long wavelengths are mostly larger than those at short wavelengths in the haze polluted sky. This is common for comparison between the clear and haze polluted cases (Chen et al., 2013). One reason could be sensitivities of different wavelengths to different particle sizes. Fig. 4.22 gives the aerosol volume size distributions retrieved from the CE318-DP#350 measurements in the unpolarized almucantar scenario. These two measurements were only 10 or 15 minutes earlier than the measurements in the polarized almucantar scenario. So the aerosol particle size distributions can be considered to be unchanged during this interval. From Fig. 4.22, one can see that the heavy

haze polluted case was dominated by fine mode particles while the clear case was dominated by coarse mode particles. Nevertheless, the volume concentrations of fine and coarse mode particles in the haze polluted case were all larger than those in the clear case. Thus, if only the depolarization effects of the multiple scattering are considered, all the values of $DoLP$ at short and long wavelengths in the haze polluted case should be lower than the corresponding values in the clear case. But the fact is that $DoLP$ at short wavelengths (e.g., 440 nm) in the haze polluted case are less than those in the clear case, while $DoLP$ at long wavelengths (e.g., 1640 nm) in the haze polluted case are larger than those in the clear case. Compared with long wavelengths, short wavelengths are more sensitive to the fine mode aerosol particles. So, $DoLP$ at 440 nm appears more obvious difference between these two cases than that at 1640 nm. In addition, different wavelength-variation behaviors of $DoLP$ in the clear and haze polluted cases also could be due to different sensitivities of short and long wavelengths to the fraction of spherical particles. It should be discussed in further study, see Chapter 6.

Comparing Figs. 4.18 (d) and 4.20 (d), it is evident that the depolarization ratios show different wavelength-variation behaviors in the haze polluted and clear cases. For the haze polluted case, the longer the wavelengths, the lower the valley values. That means, the skylight are more parallel polarized at long wavelengths at the valley positions. However, for the clear case, it shows that the longer the wavelengths, the higher the valley values. That indicates the proportions of the perpendicular polarized radiances at long wavelengths are larger than those at short wavelengths in this case. Moreover, results of ρ in the left and right almucantar planes show bad symmetry for the clear sky. It could be due to changes of the skylight polarization during two scanings in the left and right almucantar planes, which is significant for the clear sky but is negligible for the haze polluted sky.

From panels (b), (d), and (f) in Figs. 4.19 and 4.21, the maximum values of Q and U in the haze polluted case are generally less than those in the clear case. But the peak values of Q and U for different wavelengths in the haze polluted case may be higher or lower than those for corresponding wavelengths in the clear case. For example, the peak value of Q at 675 nm in

4 Method of Stokes parameter derivation

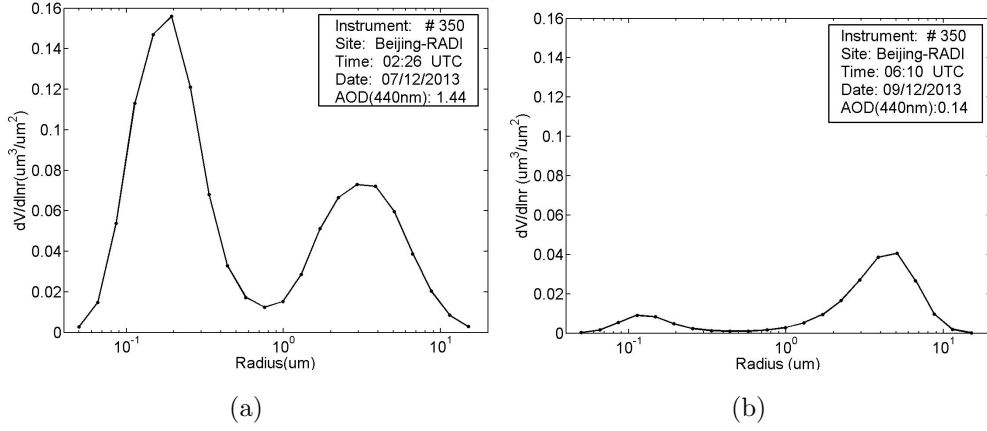


Figure 4.22: Aerosol volume size distributions retrieved from the CE318-DP#350 measurements in the almucantar geometry at the “Beijing-RADI” site. (a) haze polluted case, (b) clear case.

Fig. 4.19 (b) is higher than that in Fig. 4.21 (b); On the contrary, the peak value of Q at 440 nm in Fig. 4.19 (b) is lower than that in Fig. 4.21 (b). For the clear case, Q and U change regularly with wavelengths. The shorter the wavelengths, the higher the Q and U peak values, the lower the Q and U valley values. But in the haze polluted case, there are no regular wavelength-variation behaviors for Q and U . Moreover, unlike the haze polluted case, RAA corresponding to peak positions change little with wavelengths in the clear sky. From Fig. 4.19 (f), it can also be found that discontinuities exist in the monotone curves of AoP close to the solar direction (i.e., $RAA = 30^\circ, 330^\circ$) in the short wavelengths, such as 440 nm. This feature usually can be found in heavy haze polluted conditions. Its relation with atmospheric aerosol properties remains to further investigate.

Chapter 5

Validation and uncertainty assessment

5.1 Validation of the polarization parameters

5.1.1 Comparison with previous measurements of *DoLP* and *I*

By definition, the degree of linear polarization is deduced from the Stokes parameters *I*, *Q*, and *U*. When the Stokes parameters *Q* and *U* are unknown, *DoLP* can also be calculated directly from three polarized radiance observations, see Eq.(8) in Li et al. (2010). That is,

$$\begin{aligned} DoLP = \eta^{-2} \cdot & 2(N_1^2 + R_{12}^2 \cdot N_2^2 + R_{13}^2 \cdot N_3^2 \\ & - R_{12} \cdot N_1 \cdot N_2 - R_{13} \cdot N_1 \cdot N_3 - R_{12} \cdot R_{13} \cdot N_2 \cdot N_3)^{1/2} \quad (5.1) \\ & \cdot (N_1 + R_{12} \cdot N_2 + R_{13} \cdot N_3)^{-1}, \end{aligned}$$

where η is the polarizing efficiency that is introduced in Chapter 3. Note that the form of η is different from that in Eq.(8) in Li et al. (2010). N_1 , N_2 , and N_3 denote digital numbers detected by the instrument with three orientations of the polarizer axes (i.e., 0° , 60° , and 120°). $R_{12} = N_1^*/N_2^*$, and $R_{13} = N_1^*/N_3^*$, where N_1^* , N_2^* , and N_3^* represent the corresponding digital

numbers when the incident light is unpolarized. In this equation, R_{12} , R_{13} , and η are the calibration coefficients which are obtained by calibration of the degree of linear polarization measurement using the reflected solar light or light from the POLBOX system as polarimetric references (Li et al., 2010). Thus, $DoLP$ is calculated directly from three digital numbers other than from the Stokes parameters.

Fig. 5.1 (a) gives comparison between $DoLP$ calculated from the Stokes parameters I , Q , and U in this study and that obtained directly from three digital numbers in the past. It can be found that these two results are highly consistent for all wavelengths. The biggest difference around the maximum $DoLP$ at 870 nm is less than 0.005. Previous study has shown that total uncertainty in the $DoLP$ calibration is about 0.005 for CE318-DP (Li et al., 2010). So the differences of $DoLP$ between previous results and the results in this study are acceptable.

The Stokes parameters I calculated from measurements in polarization channels in the principal plane are also compared with the total radiances measured by the non-polarized channels of CE318-DP. Fig. 5.1 (b) gives the comparison of I obtained from the measurements of polarized and non-polarized principal plane modes. A time lag between these two measurements is about 5 minutes. The variation of skylight may not be ignored within 5 minutes, especially when the sun elevation is low. Even so, these two results are pretty close. From Fig. 5.1 (b), differences near the solar direction are bigger than which far from the solar direction. Meanwhile, the differences at 440 nm are more obvious than those for other wavelengths. The biggest difference is less than $0.007 \text{ W m}^{-2} \text{ nm}^{-1} \text{ sr}^{-1}$ in the anti-solar direction.

5.1.2 Comparison between measurements and model results

Considering that there was no results of Q , U , and the angle of polarization calculated from the CE318-DP measurements in the past, the polarization parameters simulated by the SOS vector radiative transfer model (see Chap-

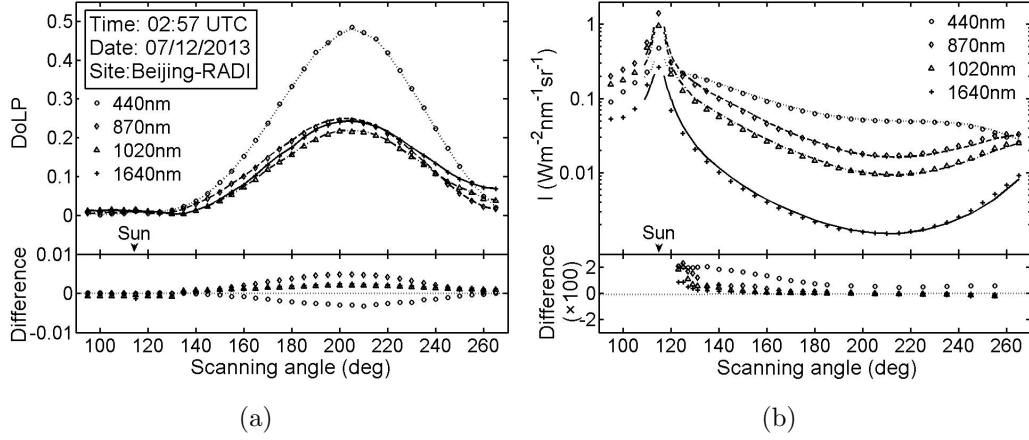


Figure 5.1: (a) Comparison between the degree of linear polarization deduced from the Stokes parameters I , Q , U in this paper (points) with that calculated directly from three polarized radiance measurements (curves) in the solar principal plane; (b) Comparison between the first Stokes component I from polarized channel measurement (points) with the total radiance from the non-polarized channel measurement (curves) in the solar principal plane. The point notations are as: circle for 440 nm; diamond for 870 nm; triangle for 1020 nm; and cross for 1640 nm. The curve notations are as: dotted line for 440 nm; dashed line for 870 nm; dash-dot line for 1020 nm; and solid line for 1640 nm (Li et al., 2014a).

ter 2) are also compared with corresponding calculated results in this study. For the SOS vector radiative transfer model simulations, the input parameters of aerosol particle size distribution, real and imaginary parts of the complex refractive index were retrieved from the CE318-DP non-polarized measurements in the almucantar geometry following the procedure described in Li et al. (2009). The AOD were obtained from the CE318-DP sun measurements following AERONET level 1.0 data criteria. As discussed in Chapter 2, the single scattering of sphere particle is calculated by the Mie code. The results are then put into the SOS radiative transfer model for multiple scattering calculations (Deuzé et al., 1989). The normalized Stokes parameters I , Q , and U are first simulated. Then, the $DoLP$ and AoP at the CE318-DP observation angles in the solar principal and the almucantar planes are deduced from them. Outputs of the scattered fields of radiances are normalized

5 Validation and uncertainty assessment

by the extraterrestrial solar irradiance.

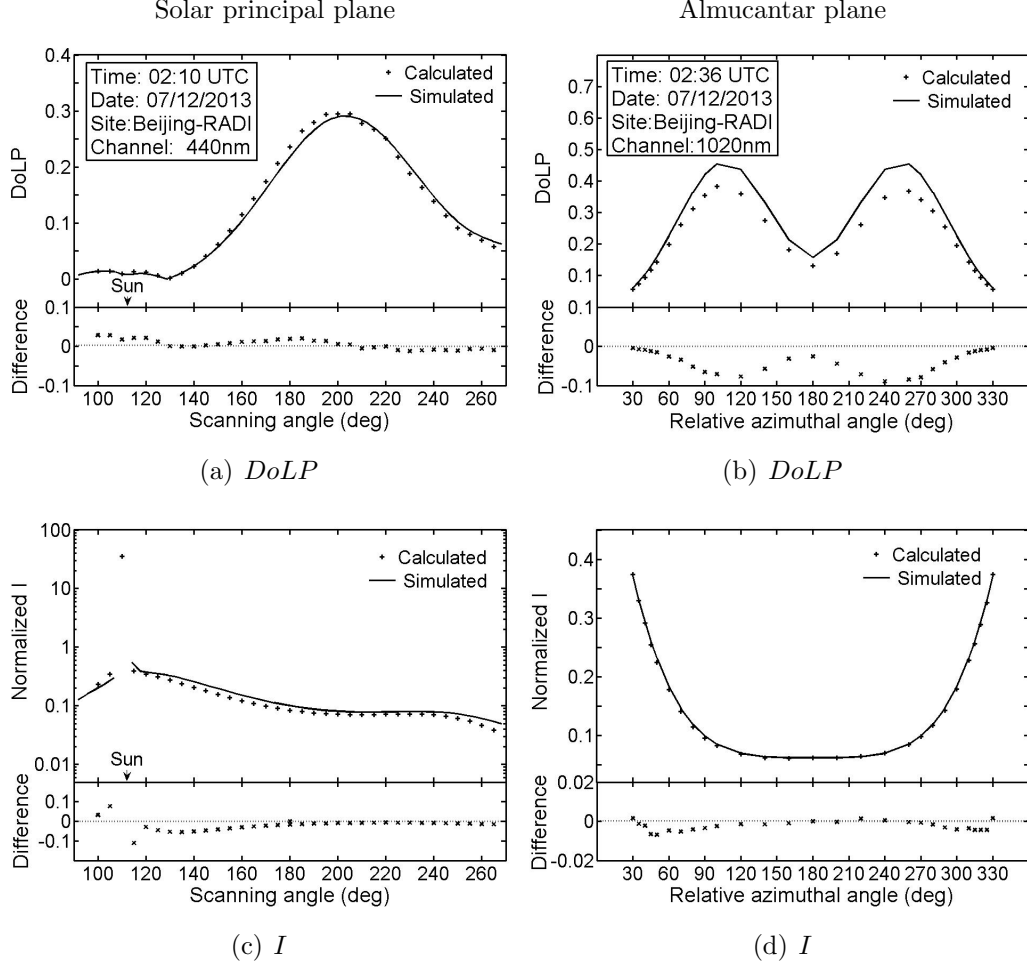


Figure 5.2: Comparisons between results of the $DoLP$ and the total radiance I calculated in this study and the SOS radiative transfer model simulations, where I is normalized by the extraterrestrial solar irradiance (Li et al., 2014a).

Figs. 5.2 and 5.3 give the comparisons between the calculated results of $DoLP$, I , Q , U , and AoP and corresponding radiative transfer model simulations. It can be seen that model simulated I and AoP agree well with the calculated results, especially for the almucantar observation geometry, see Figs. 5.2 (d) and 5.3 (f). That could be due to the input parameters derived from the almucantar observations. The absolute differences are less than 0.007 for the normalized I , and the angle differences are less than 2° for AoP in the almucantar geometry.

5 Validation and uncertainty assessment

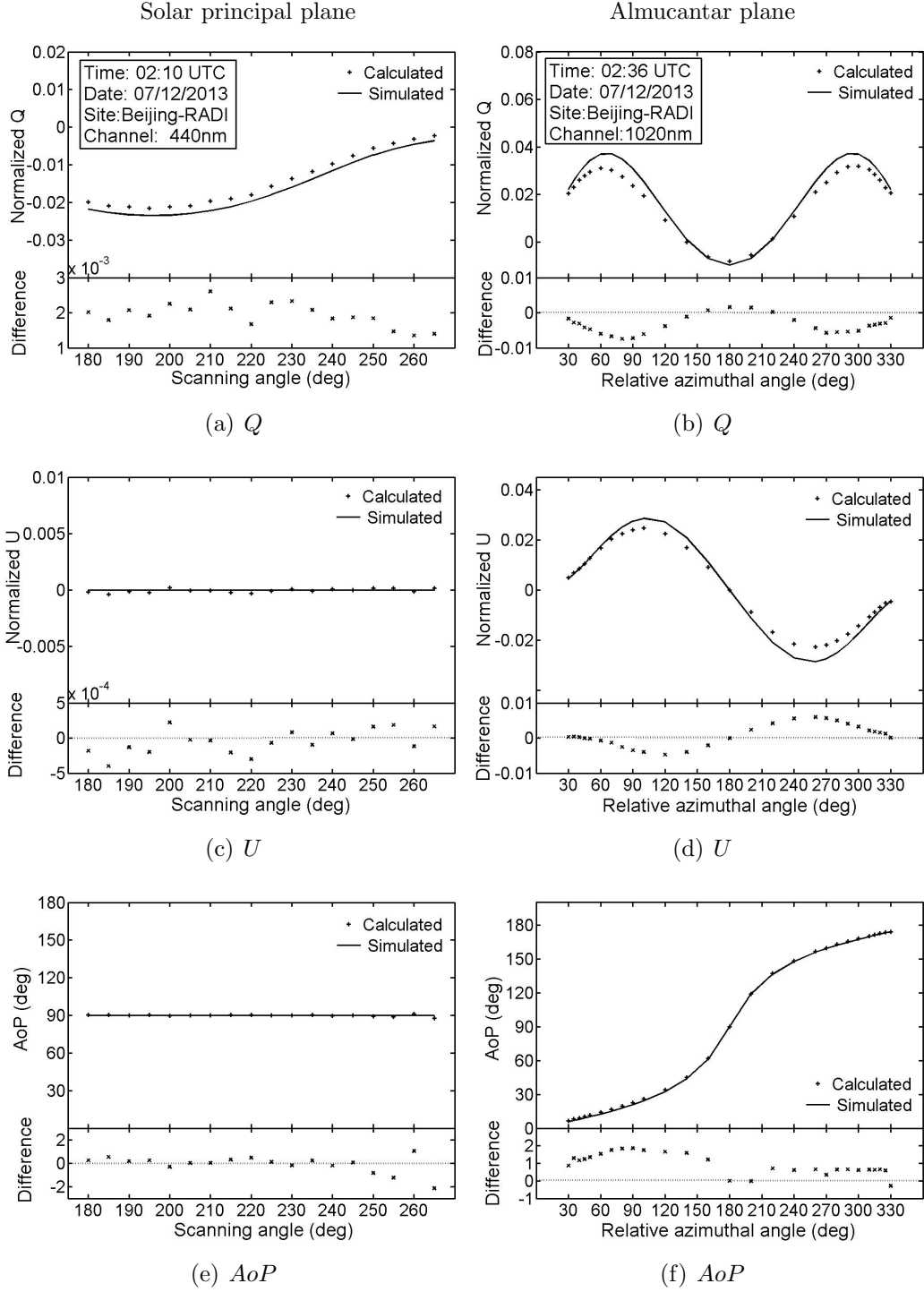


Figure 5.3: Comparisons between results of the Stokes parameters Q , U , and the AoP calculated in this study and the SOS radiative transfer model simulations, where Q and U are normalized by the extraterrestrial solar irradiance (Li et al., 2014a).

For the normalized Stokes parameters Q , U , and the $DoLP$ in Figs. 5.2 and 5.3, model simulations only qualitatively correspond with the results calculated in this study. From Fig. 5.3 (a), the simulated Q are distinctly less than corresponding measured results in the solar principal plane geometry. Obvious deviations for Q at all scanning angles in the anti-solar direction of the principal plane and deviations for the extreme values of Q , U , and $DoLP$ in the almucantar geometry are possibly attribute to unrealistic inputs adopted in model simulations. Previous study has shown that the Stokes parameters Q and U are very sensitive to aerosol particle shape, fine particle size, and real part of refractive index (Li et al., 2013). In these simulations, the aerosol particle shape is assumed as sphere. The input aerosol parameters are derived from unpolarized measurements by CE318-DP. The residual error of retrieval remains about 1.7%. There is also a short time lag between the polarized and unpolarized measurements during that the aerosol properties maybe change a little. So the input parameters of aerosol properties are more or less differ from the real situation. In addition, the effects of urban surface may contribute to some differences in the simulation of skylight polarization. Despite all of these factors, the comparison between the calculated results and model simulations generally shows a good agreement (Li et al., 2014a).

5.1.3 Comparison with the AMPR measurements

To validate the calculated results of polarization parameters in this study, the results measured by CE318-DP are also intended to compare with corresponding measurements by other types of instruments. However, the comparisons of absolute values of the Stokes parameters I , Q , U , and the degree of linear polarization present several challenges. There are strict requirements on time synchronization, spectral matching, and observation geometry consistent. Only qualitative comparison between the CE318-DP and the advanced Atmosphere Multi-angle Polarization Radiometer (AMPR) measurements is carried out in this subsection since these requirements can not be fully satisfied.

The AMPR is developed by the Anhui Institute of Optics and Fine Me-



Figure 5.4: Ground-based synchronous observations by the CE318-DP #962 and the AMPR on 19 January, 2013 in Hefei, China (31.9N, 117.2E).

chanics (AIOFM), Chinese Academy of Sciences (Wang et al., 2014a). It is currently an airborne instrument and will be carried on satellite platform in the near future. The AMPR contains six normal polarized spectral bands with central wavelengths at 490, 555, 665, 865, 960, and 1640 nm. Among them, the wavelength band at 960 nm is applied to estimate column content of water vapor and other channels are designed for atmospheric aerosol and cloud detections. The 490, 665, 865, and 1640 nm channels of the AMPR can approximately match with the 500, 675, 870, and 1640 nm wavelength bands of the CE318-DP, respectively. A ground-based synchronous measurements by these two instruments were taken during 02:52-05:49 UTC on 19 January, 2013 in Hefei, China (31.9N, 117.2E), see Fig. 5.4. The polarized skylight measurements by these two instruments were only conducted in the solar principal plane geometry. The scanning angles were from -85° to $+85^\circ$ with 5° interval for the CE318-DP measurements, while from -55° to $+55^\circ$ with 1° interval for the AMPR measurements. Here, 0° represents zenith obser-

vation. Negative scanning angles indicate the solar direction, otherwise, the anti-solar direction.

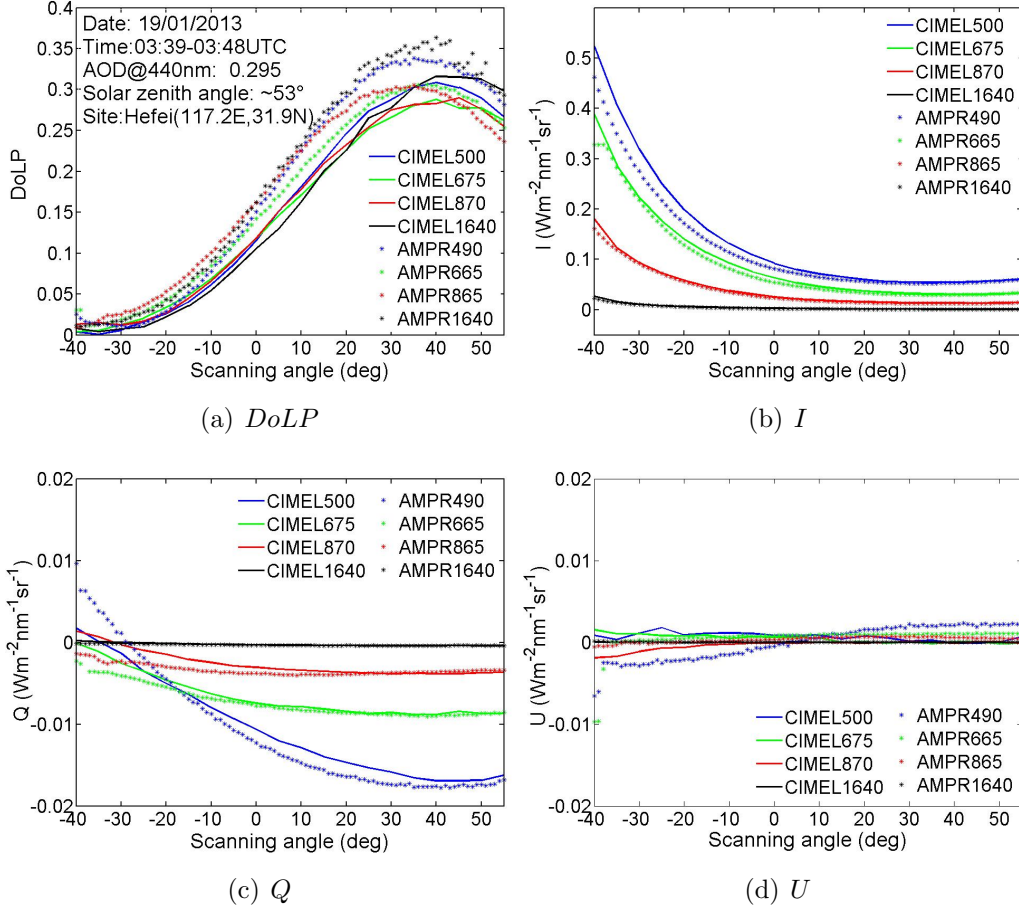


Figure 5.5: Comparisons of $DoLP$ and the Stokes parameters I , Q , and U between the CE318-DP #962 and the AMPR measurements.

Fig. 5.5 illustrates comparisons of the $DoLP$ and the Stokes parameters I , Q , and U during 03:39-03:48 UTC on 19 January, 2013. It was a clear sky and the aerosol optical depth at 440 nm was around 0.295 during this period. The solar zenith angle was about -53° . Only observations at scanning angles from -40° to $+55^\circ$ are shown in this figure. It is clear that results measured by the CE318-DP are qualitatively in consistent with the AMPR measurements. The $DoLP$ calculated from the CE318-DP measurements are less than those of the AMPR measurements for the scanning angles from -40° to $+40^\circ$, see Fig. 5.5 (a). But the total radiances I measured by the

CE318-DP are all larger than those of the AMPR measurements, especially for the scanning angles close to the solar direction, see Fig. 5.5 (b). For the Stokes parameters Q and U , discrepancies in the solar direction between the CE318-DP and the AMPR measurements are more obvious than those in the anti-solar direction, see Fig. 5.5 (c) and (d). In general, differences in $DoLP$, I , Q , and U between the 500 nm channel of CE318-DP and the 490 nm channel of AMPR are more obvious than those for other corresponding channels. Some possible reasons for quantitative differences could be inaccuracy of relative azimuthal angles for the AMPR caused by manual adjustment of the solar principal plane, inconsistencies of central wavelengths and spectral responses for corresponding channels of these two polarimetric radiometers.

5.2 Uncertainty estimation

According to above comparisons, the polarization parameters derived in this study are consistent with previous results, and comparable with the vector radiative transfer simulations and the measurements by other polarization radiometer. Moreover, uncertainties in the new calculated Stokes parameters Q , U and the angle of polarization should be further estimated in details.

As we know, uncertainties of the Stokes parameter I and the $DoLP$ those can be obtained from CE318-DP polarized skylight measurements in the past could be due to: i) accuracy of polarization calibration; ii) assumption of the instrument's Mueller matrix for perfect polarizers; iii) pointing errors of scanning angles in the solar principal plane and the almucantar plane geometries. These factors also have similar influences on the new derived Stokes parameters Q and U . In this study, an additional hypothesis of AoP theoretical value of skylight in the principal plane geometry for perfect installation of the optical sensor head to automated mount of the instrument is proposed for calculating of the Stokes parameters Q and U . A rotation angle is obtained based on this hypothesis. Then, the Stokes parameters Q and U are deduced by rotating the reference coordinate system from the instrument frame to

the sky frame. Therefore, the value of AoP measured in the reference plane is necessary for the calculations of Q and U .

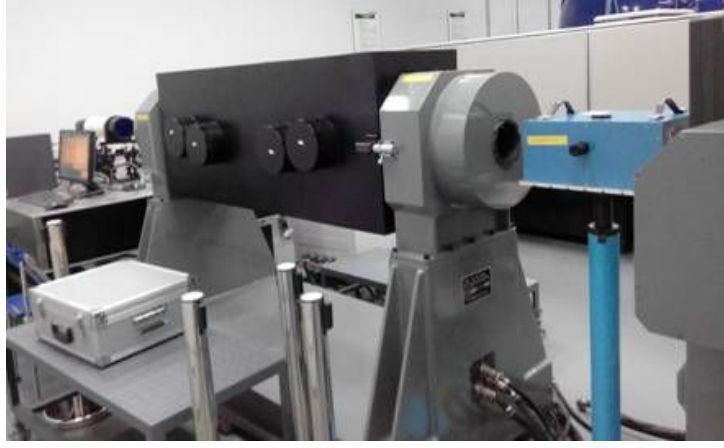
To specify uncertainties in the new derived Q , U , and AoP in this study, rationality of hypothesis of the AoP theoretical value is first discussed, then the error in measured AoP by CE318-DP is estimated, and finally the uncertainties in I , $DoLP$, and AoP are propagated to Q and U according to the law of uncertainty propagation:

First, rationality of the theoretical AoP assumption for the CE318-DP perfect installation is discussed.

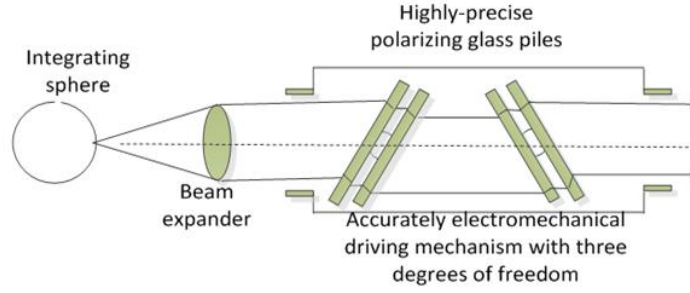
In the case of perfect installation for CE318-DP, the collimators of optical sensor head should be within the solar principal plane. The scattering plane is the same as the solar principal plane in the principal plane observing geometry (see Fig. 2.1). According to the celestial polarization pattern (see Fig. 4.5), the direction of polarization should be perpendicular to the scattering plane in theory, that is, AoP of skylight is equal to 90° with respect to the solar principal plane (Horváth and Varjú, 2004; Smith, 2007). Measurements have shown that differing from the $DoLP$ and total radiance of skylight which are highly variable, AoP is the most stable and predictable parameter of skylight even under a wide range of atmosphere conditions (e.g., in a cloudy sky, or in fog) (Horváth and Varjú, 2004). So, similar to the hypothesis of non-polarization (i.e., $DoLP = 0$) for the direct solar beam and the emergent light of integrating sphere which are widely adopted as references in polarization calibration (Li et al., 2010), the $90^\circ AoP$ of skylight in the solar principal plane around the scanning angles corresponding to the strongly polarized directions (e.g., at 90° from the sun) can be a reasonable theoretical value.

Second, the error in AoP measured by CE318-DP is estimated through a laboratory experiment.

Experimental measurement of AoP by the CE318-DP #350 was carried out in a super clean chamber on 19 and 20 June, 2014. As the reference light, partially polarized light with a fixed large $DoLP$ (strong polarized)



(a) Picture of the VPOLS system



(b) Schematic diagram of the VPOLS system

Figure 5.6: The high-precision Variable POLarization Light Source (VPOLS) system, cited from <http://klocc.aiofm.ac.cn/yqsb>.

and variable AoP (different polarization directions) is generated through a new generation of the high-precision Variable POLarization Light Source (VPOLS), see Fig. 5.6 (Chen et al., 2012). Like the POLBOX system, the VPOLS system is also composed of an integrating sphere and a polarizing system which consists of four K9 glass plates (Pietras et al., 2000; Chen et al., 2012). This system is usually applied for calibration of polarized instruments. The degree and direction of polarization for partial polarized light generated from the VPOLS system are adjusted by changing dip angles of the glass plates and rotating the VPOLS box, respectively. The $DoLP$ of the reference polarized light is calculated from the refractive index and dip angles of the glass plates, which is normally from 0 to ~ 0.6 in a spectral range from visible

to near infrared. To obtain a fixed large *DoLP* and variable directions of polarized light as reference light, the rotation angle of the VPOLS can be adjusted from 0° to 180° with a fixed 60° dip angle for the glass plates. The values of *DoLP* in this situation are listed in Tab. 5.1.

Table 5.1: The degree of linear polarization of the VPOLS system with a fixed 60° orientation angle for the glass plates.

Wavelengths	<i>DoLP</i>
440 nm	0.632275270943109
675 nm	0.621291188587754
870 nm	0.617285951824228
1020 nm	0.615209735179417

The relative digital numbers (i.e., ratio of digital numbers in polarized channels to the corresponding unpolarized channels) of the reference light measured by the CE318-DP #350 are illustrated in Fig. 5.7. It is clear that any solid line which indicates peak position for one polarizer's curve just goes through the intersection point of the other two polarizers' curves, while it is also true for any dash line which indicates valley position for one polarizer's curve. It illustrates that three polarizers for the same channel keep 60° between orientations of any two polarizer-preferred transmittance axes. Moreover, it can also be found that the wavelength bands at 675 and 870 nm have the same peak and valley positions. That means, these two bands share the same set of polarizer triplets.

Fig. 5.8 shows *AoP* calculated from the digital numbers with respect to the plane containing the vibration direction and the propagation direction of partially polarized light for the VPOLS system with rotation angle of 0° . According to Fig. 5.8, *AoP* measured by the CE318-DP shows good agreement with the theoretical *AoP* for the VPOLS system. Most of the angle differences between them are less than $\pm 1^\circ$. Previous study has illustrated that regions of the sky that provide reliable compass information are

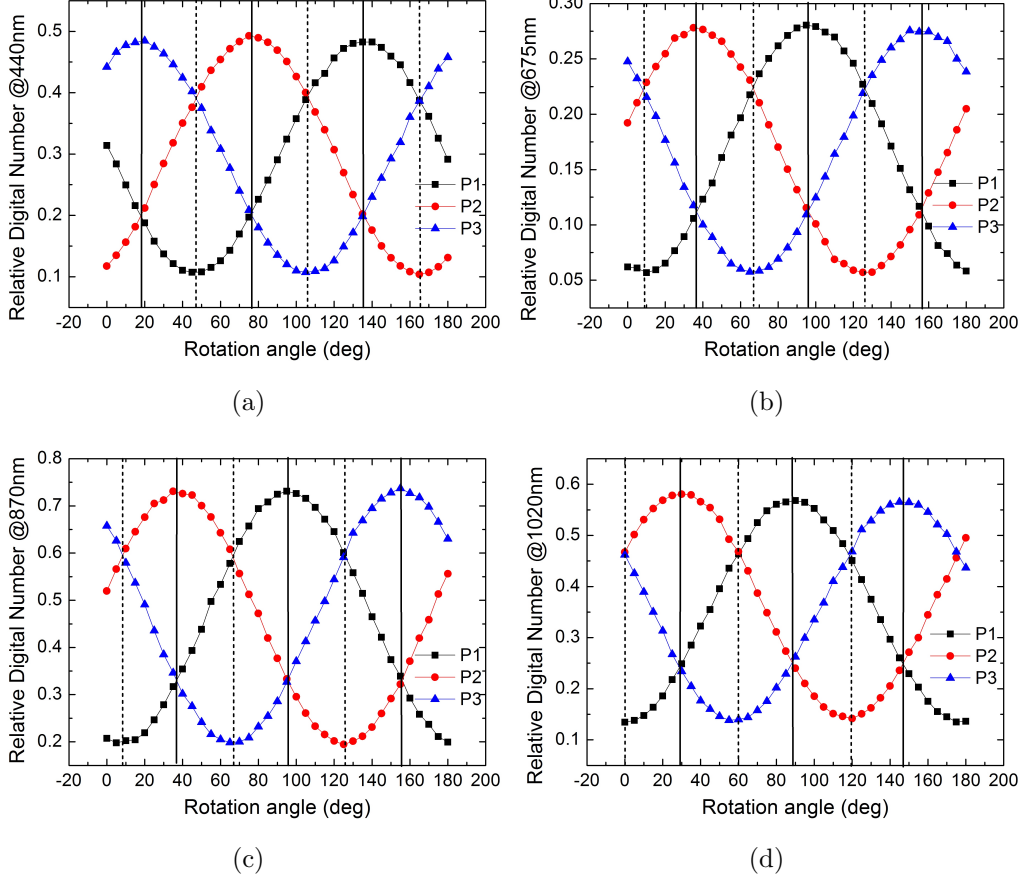


Figure 5.7: Relative digital numbers measured by the CE318-DP #350 for partially polarized incident light with a fixed *DoLP* (fixed dip angle of the glass plates) and polarization orientations (rotating angles of the VPOLS box) changing from 0° to 180° . P1, P2, and P3 represent the three polarizers for the same wavelength band; solid lines indicate positions of the wave peaks where the angles correspond to the linear polarizer-preferred transmission directions; and dash lines indicate positions of the wave valleys where the angles correspond to directions of 90° to the linear polarizer-preferred transmittance axes. (a) 440 nm, (b) 675 nm, (c) 870 nm, (d) 1020 nm.

5 Validation and uncertainty assessment

characterized by $|AoP_{\text{clear sky}} - AoP_{\text{cloud}}| \leq 4^\circ \sim 6.5^\circ$ (Horváth and Varjú, 2004). So, the discrepancy of 1° in measured AoP is acceptable for skylight polarization navigation.

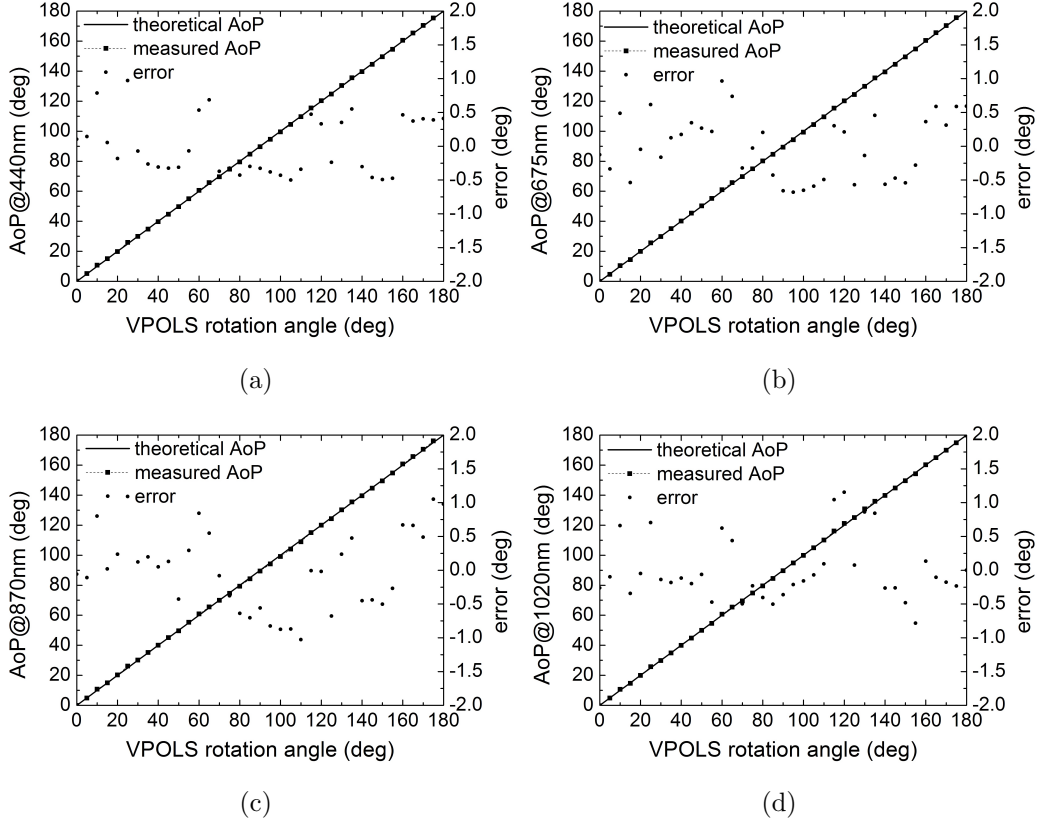


Figure 5.8: AoP calculated from the CE318-DP #350 measurements for partially polarized incident light with a fixed $DoLP$ and polarization orientations changing from 0° to 180° . (a) 440 nm, (b) 675 nm, (c) 870 nm, (d) 1020 nm.

Sensitivities of AoP to the atmospheric particle properties (including real and imaginary parts of the complex refractive index, the particle shape and size) are illustrated in Fig. 5.9. The simulated results show that AoP change significantly with real and imaginary parts of the complex refractive index and particle shape around the solar direction in the almucantar geometry (i.e., the relative azimuthal angles are close to 30° and 330°), see Fig. 5.9 (a), (b), and (c). The sudden changes around the solar direction are related to large real part and small imaginary part of the refractive index and spherical

particles (i.e., $a/b=1$). This usually can be observed in the haze polluted days. However, in other directions in Fig. 5.9 (a), (b), (c) and in all directions in Fig. 5.9 (d), AoP show extremely small variations. Compared with the large variations of AoP (usually $> 80^\circ$) around the solar direction affected by different atmospheric particle properties, the discrepancy of 1° in measured AoP is acceptable. Hence, the discrepancy of AoP between the theoretical and real values is treated as 1° (~ 0.017 rad) in the following.

Table 5.2: Input parameters of the radiative transfer simulation for the AoP sensitivity study in Fig. 5.9.

Parameters	Standard value	Changes of the value
Wavelength(λ)	0.55 μm	constant
Aerosol particle effective radius (r)	0.1 μm	0.02, 0.08, 0.48, 1.28 μm
Particle size distribution	power law	constant
Shape parameter of spheroid (a/b)	1(sphere)	0.5, 1, 2, 3
Real part of refractive index (m_r)	1.53	1.33, 1.4, 1.53, 1.75
Imaginary part of refractive index (m_i)	0.007	0.1E-7, 0.007, 0.02, 0.44
Aerosol optical thickness	0.5	constant
Rayleigh optical thickness	0.097069	constant
Surface albedo	0.1	constant
Solar zenith angle	45°	constant
Viewing zenith angle	45°	constant
Relative azimuthal angle	$0^\circ, 180^\circ$	$30^\circ - 330^\circ$

Last, uncertainties in the calculated Stokes parameters Q and U resulting from uncertainties of I , $DoLP$, and AoP are evaluated.

As discussed above, uncertainty in AoP measured by CE318-DP is $\sim 1^\circ$ (i.e., ~ 0.017 rad) . Previous studies have also shown that the fractional

5 Validation and uncertainty assessment

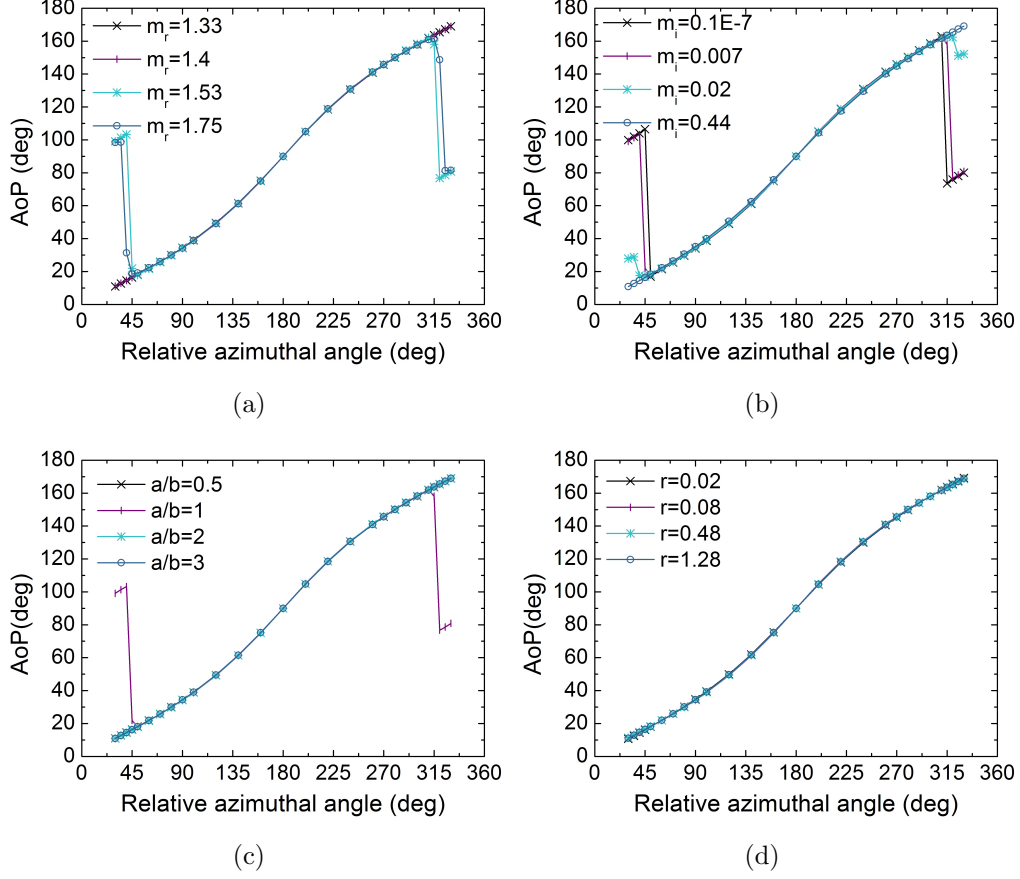


Figure 5.9: Sensitivities of the AoP to real part of the refractive index m_r (a), imaginary part of the refractive index m_i (b), particle shape a/b (c), and particle size r (d). a/b is the axial ratio, where a is the horizontal semi-axis and b is the rotational (vertical) semi-axis of the spheroid particle. $a/b = 1$ indicate the spherical particle. r denotes radius of spherical particle. (Input parameters for the simulation are listed in Tab. 5.2. The Mie and T -matrix codes were used to calculate single scattering by spherical and non-spherical particles, respectively. Outputs of the particle optical properties, including extinction coefficient, asymmetry factor, single scattering albedo and expansion coefficients of scattering matrix were then put into the vector radiative transfer model SCIATRAN to simulate the Stokes parameters, and to further calculate angle of polarization.)

uncertainty in I has been decreased from 5 % at early stage of the AERONET to the current ~ 3 % (Holben et al., 1998; Li et al., 2008). The final $DoLP$ calibration uncertainty for the CE318-DP has also been estimated ~ 0.005 (Li et al., 2010). Moreover, it is reasonable to suppose that I , $DoLP$, and AoP have independent random errors. Then, we can consider 3 % fractional uncertainty in I , 0.005 uncertainty in $DoLP$, and 0.017 rad uncertainty in AoP here. Namely,

$$\begin{aligned}\frac{\delta I}{I} &= 3\%, \\ \delta DoLP &= 0.005, \\ \delta \chi &= 0.017.\end{aligned}\tag{5.2}$$

According to Eqs. (2.10) and (2.11), Q and U are calculated as

$$\begin{aligned}Q &= I \cdot DoP \cdot \cos 2\beta \cdot \cos 2\chi, \\ U &= I \cdot DoP \cdot \cos 2\beta \cdot \sin 2\chi.\end{aligned}\tag{5.3}$$

Where β is equal to 0° for linear polarization (i.e., $\cos 2\beta = 1$). As discussed above, the partially polarized skylight is predominantly linear polarized. Then, the calculations of the Stokes parameters Q and U are simplified as (Tilstra et al., 2003)

$$\begin{aligned}Q &= I \cdot DoLP \cdot \cos 2\chi, \\ U &= I \cdot DoLP \cdot \sin 2\chi.\end{aligned}\tag{5.4}$$

Uncertainties in the Stokes parameters Q and U are estimated according to the law of propagation of uncertainties (Taylor, 1982; Zhang, 2006):

$$\begin{aligned}\delta Q &= [(DoLP \cdot \cos 2\chi \cdot \delta I)^2 + (I \cdot \cos 2\chi \cdot \delta DoLP)^2 \\ &\quad + (I \cdot DoLP \cdot 2 \sin 2\chi \cdot \delta \chi)^2]^{1/2}, \\ \delta U &= [(DoLP \cdot \sin 2\chi \cdot \delta I)^2 + (I \cdot \sin 2\chi \cdot \delta DoLP)^2 \\ &\quad + (I \cdot DoLP \cdot 2 \cos 2\chi \cdot \delta \chi)^2]^{1/2}.\end{aligned}\tag{5.5}$$

Considering Q and U are often expressed in a normalized form (normalized by the total radiance), the uncertainties in Q and U are also normalized

by the total radiance I to compare with the fractional uncertainty in I (Liu and Voss, 1997; Feng et al., 2013; Li et al., 2013). On the basis of long-term observations, the angle of 90° for AoP and the typical values of 0.6 and 0.2 for $DoLP$ in the clear and multiple-scattering atmosphere conditions around the maximum polarization positions in the anti-solar half sky are adopted. Then,

$$\begin{aligned}
 \frac{\delta Q}{I} &= [(DoLP \cdot \cos 2\chi \cdot \frac{\delta I}{I})^2 + (\cos 2\chi \cdot \delta DoLP)^2 \\
 &\quad + (DoLP \cdot 2 \sin 2\chi \cdot \delta\chi)^2]^{1/2}, \\
 &\approx 0.8\%, \quad \text{for } DoLP = 0.2, \\
 &\approx 1.9\%, \quad \text{for } DoLP = 0.6; \\
 \frac{\delta U}{I} &= [(DoLP \cdot \sin 2\chi \cdot \frac{\delta I}{I})^2 + (\sin 2\chi \cdot \delta DoLP)^2 \\
 &\quad + (DoLP \cdot 2 \cos 2\chi \cdot \delta\chi)^2]^{1/2}, \\
 &\approx 0.7\%, \quad \text{for } DoLP = 0.2, \\
 &\approx 2\%, \quad \text{for } DoLP = 0.6.
 \end{aligned} \tag{5.6}$$

In the typical clear atmospheric condition with $DoLP = 0.2$, $\delta Q/I$ is about 0.8% and $\delta U/I$ is approximately equal to 0.7%; while in the typical multiple-scattering atmospheric condition with $DoLP = 0.6$, $\delta Q/I$ is about 1.9% and $\delta U/I$ can reach up to 2%. It can be found that the relative uncertainties in Q and U increase as $DoLP$ increases. Given that the normalized U in the solar principal plane is quite small, the uncertainty in U is relatively large. So the value of U calculated from CE318-DP measurements in the solar principal plane geometry can not be solely utilized. Nevertheless, the uncertainties of Q in both of the solar principal plane and almucantar plane geometries and that of U in the almucantar plane geometry are acceptable relative to values of the normalized Q and U in these observation geometries.

Chapter 6

Concluding remarks

6.1 Summary

As a mature commercial ground-based polarimetric instrument, the CIMEL Dual-Polar sun/sky radiometer (CE318-DP) provides accurate, reliable, and continuous skylight polarization measurements for an extended wavelength range from 340 to 1640 nm. It has been routinely operated within the SONET in China and selected stations of the AERONET around the world. Retrievals of several microphysical properties of aerosol particles are improved significantly by using the degree of linear polarization derived from CE318-DP polarized skylight observations. Besides $DoLP$ and the total radiance I , which are obtain from CE318-DP polarization measurements in the past, other polarization parameters such as the Stokes parameters Q and U , as well as the angle of polarization contain additional information on linear polarization and its orientation. They have much potential to improve retrievals of aerosol microphysical and chemical properties. However, they have not been derived from the CE318-DP measurements so far. In response to the needs for improving observation capabilities of the CE318-DP regrading atmospheric skylight polarization, this thesis has developed a method to calculate the Stokes components Q , U , and AoP from ground-based CE318-DP measurements, and further derive the perpendicular and parallel polarized

radiances I_r and I_l , as well as the linear depolarization ratio ρ . These new polarization parameters in conjunction with $DoLP$ and I are analyzed based on the long-term observations in key areas of China.

In Chapter 2, to calculate Q and U , the relationship between the angle of polarization and signs of the Stokes parameters Q and U is discussed first. When Q is known, the perpendicular and parallel components of the polarized radiance I_r and I_l are separated from the total radiance I , and ρ is derived from I_r and I_l . They can provide unique polarization information for atmospheric aerosol remote sensing. The $DoLP$, I_r , and I_l of skylight are deduced after single Rayleigh scattering, spherical particle scattering, and nonspherical particle scattering for the unpolarized, the perpendicular linearly polarized, and the parallel linearly polarized incident radiation, respectively. For the unpolarized incident radiation, the scattered light becomes partly polarized (i.e., $0 < DoLP < 1$) after the interaction with a scattering particle in the atmosphere. When the scattering obstacle is a very small spherical particle such as an air molecular, I_r is larger than I_l at all scattering angles. When the scatter is a spherical or nonspherical aerosol particle, I_r can be larger or less than I_l at different scattering angles. For the perpendicular or parallel linearly polarized incident radiation, the scattered light is still perpendicular or parallel linearly polarized (i.e., $DoLP = 1$) after the interaction with a very small spherical particle or a spherical aerosol particle in the atmosphere, while it becomes partly polarized (i.e., $0 < DoLP < 1$) after the interaction with a nonspherical particle. Scattering by spherical particles does not change polarization state of the polarized incident radiation, whereas scattering by nonspherical particle changes polarization state of the polarized incident radiation, resulting in a decrease in the incident polarization and an increase in polarization perpendicular to the original polarization. When taking multiple scattering into account, the contributors from scattering path to the ground-based polarimetric radiometer in a clear, cloudless sky (including Rayleigh scattering, spherical or nonspherical particle single scattering, and multiple scattering) are elaborated. As a result, the polarization state of skylight measured by ground-based instruments could be unpolarized, polarized perpendicular or parallel to the scattering plane

for different atmospheric conditions depending upon the relative magnitudes of each unpolarized and polarized components in the scattering processes. Some single scattering codes (including Mie, T -matrix, and Spheroid kernels) and vector radiative transfer models (including SOS and SCIATRAN) are employed to simulate these processes.

The ground-based polarimetric instrument used to measure skylight polarization is the CE318-DP in this study. It has polarization observation capability in 8 polarized channels with center wavelengths at 340, 380, 440, 500, 675, 870, 1020, and 1640 nm, respectively. The Stokes components Q and U are calculated from three radiance measurements by the polarized channels. Working mechanism and polarization calibration for the CE318-DP are illustrated in Chapter 3. The polarization measurements at each wavelength band are done through combination of polarizers and filters. Correspondences between different bands and polarizers are explained first. Some bands share the same set of polarizer triplets. The combinations are fixed for the same instrument, but are not unified for different instruments. For the CE318-DP labeled #954, #962, and #969, the channels of 340 and 380 nm; 440, 500, and 675 nm; 870, 1020 and 1640 nm share the three set of polarizer triplets, respectively. However, for the CE318-DP labeled #350, the bands of 340, 380, 440, and 500 nm; 675 and 870 nm; 1020 and 1640 nm bands share the three sets of polarizer triplets, separately. The CE318-DP normally conducts polarization measurements only in the principal plane geometry. Considering that some polarization parameters (e.g., U and AoP) in almucantar geometry contain more variation features of skylight, the polarized observations of a CE318-DP (labeled #350) are also extended from the solar principal plane to the almucantar plane. Then, it preforms skylight polarization measurements at 35 scanning angles in the solar principal plane geometry and at 28 relative azimuthal angles in the almucantar geometry per hour. To calculate Q and U from three radiance measurements at each wavelength, calibration coefficients of radiances for the polarized channels are needed to know. They are obtained by measuring unpolarized light from an integrating sphere. The polarizing efficiency describing imperfect polarizer is not considered here. CE318-DP is the main instrument for the SONET. The long-term

sites of polarization measurements in key areas of China within the SONET are introduced in this chapter.

There is an uncontrolled initial error angle when the optical sensor head of CE318-DP is installed on the automated mount. Then, orientations of the polarizers' axes in the optical sensor head is hard to know due to this initial angle. Since the values of Q and U depend on the reference plane which is conventionally defined with respect to the meridian plane other than the plane containing orientation of the 0° polarizer axis, they are difficult to be obtained from CE318-DP polarization measurements. In Chapter 4, two reference planes and corresponding coordinate systems in the sky frame and the instrument frame related to the CE318-DP polarization measurements are clarified first. To calculate Q and U in the sky frame, a rotation angle for transforming the reference coordinate systems from the instrument frame to the sky frame should be known. The polarization pattern of skylight is applied to correct the initial angle of the instrumental reference plane and to obtain the rotation angle in this study. Then, Q , U , and AoP are obtained from the CE318-DP polarization measurements besides $DoLP$ and I . I_r , I_l , and ρ are further derived from the Stokes components.

Results of these polarization parameters (including I , Q , U , $DoLP$, AoP , I_l , I_r , and ρ) of skylight affected by different types of aerosol particles are also discussed in Chapter 4. For the solar principal plane observations, results of the typical haze polluted urban, rural, clean continental, mineral dust and maritime aerosol cases are selected from sufficiently long observations at the “Beijing-RADI”, “ZhangyeHH”, “Lhasa”, “Minqin” and “Zhoushan” sites within SONET. There are some common features in these five cases. The maximum I and minor $DoLP$ are measured around the solar direction for all wavelengths. I decreases as the scattering angle increases in the forward direction, while the $DoLP$ increases as the scattering angle increases in the forward direction and reaches a peak around the 90° scattering angle. Around the solar direction, I_l are very close to I_r . However, I_r are obviously larger than I_l around the scattering angle of 90° . That means the skylight is nearly non-polarized around the solar direction but is polarized perpendicular to the principal plane around the 90° scattering angle. From the results

of depolarization ratio, it is more clear that ρ for all wavelengths are larger than 1. Results of Q , U , and AoP after rotation are generally consistent with the polarization pattern of skylight in nature. Namely, Q are less than zero; U are almost all equal to zero; AoP are close to 90° for all wavelengths in the anti-solar direction of the principal plane. U and AoP after rotation have no significant variations with scanning angle and wavelength, while results of Q after rotation change obviously with them. Then, Q is recommended to analyze the influences of different aerosol microphysical properties and chemical components on the polarized skylight in the solar principal plane geometry. In addition to these common features, there are also obvious differences among these cases. For example, although both $DoLP$ and I are wavelength-dependent, they show opposite tendencies in the haze polluted urban case at the “Beijing-RAD” site. That is, the longer the wavelengths, the higher the maximum $DoLP$ values and the lower the minimum I values. On the contrary, in the rural case at the “ZhangyeHH” site and the clean continental case at the “Lhasa” site, the wavelength-dependences of $DoLP$ are consistent with I . Namely, the longer the wavelengths, the lower the maximum $DoLP$ and the minimum I values. Moreover, there are no obvious wavelength-dependence of $DoLP$ in the mineral dust and maritime aerosol cases at the “Minqin” and “Zhoushan” sites. These discrepancies indicate different effects among these five types of aerosol particles. Meanwhile, results of AoP before rotation can imply combinations of polarizers and filters for different instruments. The 80° difference between AoP at 870, 1020 nm and that at 1640 nm has also been clarified in this chapter.

Only one site within SONET, the “Beijing-RADI”, has polarization measurements in the almucantar plane. In Chapter 4, results of I , Q , U , $DoLP$, AoP , I_l , I_r , and ρ calculated from CE318-DP polarized almucantar measurements are discussed for the first time. They show some common features in the haze polluted and clear sky conditions. All these results are symmetric with respect to the principal plane (i.e., $RAA = 180^\circ$). I and I_r keep steady or fall slowly first and then rise rapidly with RAA away from 180° , while I_l simply increases with RAA deviating from 180° . I , I_r , and I_l all reach peak values close to the solar direction (i.e., $RAA = 30^\circ, 330^\circ$). For all

wavelengths, $DoLP$ reach two peaks around the 90° scattering angles in the left and right almucantar planes, and reach valleys in the principal plane or close to the solar directions. Unlike in the principal plane where the depolarization ratios show similar variations with the scanning angle as the $DoLP$, they show opposite variation features to $DoLP$ in the almucantar geometry. For all wavelengths, ρ are larger than 1 and reach maximums around the principal plane, but are less than 1 at most other relative azimuthal angles. That means, the skylight is perpendicular polarized around the principal plane, but is parallel polarized in other observing directions in the almucantar plane. Q , U , and AoP in the almucantar geometry can present more variation features of skylight in comparison with corresponding results in the principal plane geometry. After the reference coordinate system rotation, Q is symmetric and U is anti-symmetric with respect to the principal plane, while AoP appears almost monotonous variation as relative azimuthal angle increases. When RAA is equal to 180° , Q reaches the minimum; U is nearly equal to zero, and AoP is 90° . The peak values of Q and U vary with wavelength. But AoP change little with wavelength at most relative azimuthal angles, especially in the solar principal plane.

Significant discrepancies also exist between results of the haze polluted urban and the clear cases in the almucantar geometry. For example, $DoLP$ in the clear and haze polluted cases show different wavelength-dependences. The values of $DoLP$ at long wavelengths are less than those at short wavelengths at most relative azimuthal angles (except around the principal plane) in the clear sky. On the contrary, the values of $DoLP$ at long wavelengths are mostly larger than those at short wavelengths in the haze polluted sky. It could be due to sensitivities of different wavelengths to different particle sizes or to the fraction of spherical particles. Similar to $DoLP$, the maximums of Q and U in the haze polluted case are generally less than those in the clear case. For the clear case, Q and U change regularly with wavelengths. Namely, the shorter the wavelengths, the higher the Q and U peak values, the lower the Q and U valley values. But in the haze polluted case, there are no regular wavelength-dependence for Q and U . ρ also show different wavelength-dependences in the haze polluted and clear cases. The longer the

wavelengths, the lower the valley values in the haze polluted case; however, it shows that the longer the wavelengths, the higher the valley values in the clear case. Moreover, results of the depolarization ratio in the left and right almucantar planes show bad symmetry for the clear sky. It could be due to changes of the skylight polarization during two scanning processes in the left and right almucantar planes, which is significant for the clear sky but is negligible for the haze polluted sky.

In Chapter 5, results of I and $DoLP$ in the solar principal plane are first separately compared with the total radiance I measured from non-polarized channels of CE318-DP and the $DoLP$ obtained from three polarized radiance observations instead of calculating from the Stokes parameters I , Q , and U . Two results of $DoLP$ are highly consistent for all wavelengths. The biggest difference around the maximum $DoLP$ at 870 nm is less than 0.005. Two results of I obtained from the measurements of polarized and non-polarized principal plane modes are very close to each other. The biggest difference in I is less than $0.007 \text{ W m}^{-2} \text{ nm}^{-1} \text{ sr}^{-1}$ in the anti-solar direction. Considering that there was no results of Q , U , and AoP calculated from CE318-DP measurements in the past, the polarization parameters I , Q , U , $DoLP$, and AoP simulated by the SOS vector radiative transfer model are also compared with corresponding calculated results in this chapter. Model simulated I and AoP agree well with the calculated results, especially for the almucantar observation geometry. The absolute differences are less than 0.007 for the normalized I , and the angle differences are less than 2° for AoP in the almucantar geometry. However, model simulations only qualitatively correspond with results of the normalized Q , U , and AoP calculated in this study. Obvious deviations for Q in the anti-solar direction of the principal plane and deviations for the extreme values of Q , U , and $DoLP$ in the almucantar geometry are possibly attribute to unrealistic inputs adopted in model simulations. Furthermore, a comparison between the CE318-DP and the AMPR polarization measurements is carried out. In general, results measured by the CE318-DP are qualitatively in consistent with the AMPR measurements. $DoLP$ calculated from the CE318-DP measurements are less than those of the AMPR measurements at the scanning angles from -40°

to $+40^\circ$ in the principal plane. But I measured by the CE318-DP are all larger than those of the AMPR measurements, especially for the scanning angles close to the solar direction. For Q and U , discrepancies in the solar direction are more obvious than those in the anti-solar direction. According to these comparisons, the polarization parameters calculated in this study are consistent with previous results, and generally comparable with the vector radiative transfer simulations and measurements by other polarization radiometer.

To further specify uncertainties in the new derived Q , U , and AoP in Chapter 5, rationality of the theoretical AoP assumption for the CE318-DP perfect installation is discussed. Then, considering a 1° (~ 0.017 rad) discrepancy of AoP between the theoretical and real values and 3% fractional uncertainty in I and 0.005 uncertainty in $DoLP$, these uncertainties are propagated to the new derived Q and U according to the law of uncertainty propagation. In the typical clear sky with $DoLP = 0.2$, uncertainties in normalized Q and U (i.e., $\delta Q/I$ and $\delta U/I$) are about 0.8% and 0.7%, respectively; while in the typical multiple-scattering sky with $DoLP = 0.6$, $\delta Q/I$ is about 1.9% and $\delta U/I$ can reach up to 2%. Considering that U in the solar principal plane is quite small, the uncertainty in U is relatively large. While the uncertainties of Q in both of the solar principal plane and almucantar plane geometries and that of U in the almucantar plane geometry are acceptable.

6.2 Outlook

(A) calibration of the angle of polarizer

The Stokes parameters I , Q , and U are calculated from three radiance measurements by the polarized channels of CE318-DP. $DoLP$, AoP and other polarization parameters are indirectly derived from I , Q , and U . Polarization calibration is vital to obtain the Stokes components and other polarization parameters. As discussed in Chapter 3 and 4, the orientations of three polarizers for one set of triplet are considered to maintain 60° from

each other for CE318-DP. When choosing the instrument coordinate system as a reference, the plane containing the direction of 0° polarizer-preferred transmittance axis and the direction of propagation of light beam is defined as the reference plane. Then, polarizer orientation angles are determined following $\Psi_1 = 0^\circ$, $\Psi_2 = 60^\circ$, and $\Psi_3 = 120^\circ$. The Mueller matrix of instrument is obtained according to these orientation angles in calculation of the Stokes components I , Q , and U .

However, the laboratory experiment in Chapter 5 has shown that the angle differences between AoP measured by the CE318-DP and theoretical AoP of the VPOLS system are about $\pm 1^\circ$. The discrepancy could be introduced by the orientations of three polarizers which are not keeping 60° interval, see the angle differences between any two solid lines or dash lines in Fig. 5.7. These angle differences should be considered in the Mueller matrix of instrument. So, the interval between two polarizers' orientations should be dealt with in polarization calibration of CE318-DP in the future. The angles of polarizer will be measured in laboratory and introduced into the Mueller matrix to further improve calculation accuracy of the Stokes parameters.

(B) application in nonspherical aerosol identification

Polarization of skylight can imply valuable information on atmospheric aerosol particles due to interactions of light and aerosol particles in the atmosphere. Considering that particle morphology is of vital importance to how electromagnetic radiation is scattered by aerosol particle, knowledge about various nonspherical aerosol particle shapes get more and more attention in aerosol remote sensing. Light scattering by nonspherical particle such as mineral dust is commonly known as a major difficulty in aerosol characterization (Mishchenko et al., 1997; Dubovik et al., 2002; Merikallio et al., 2011). Compared with the total radiance, polarization measurements have distinct advantage in nonspherical aerosol remote sensing according to the special sensitivities of skylight polarization to aerosol particle shape.

As discussed in Chapter 4, in addition to $DoLP$, the new polarization parameters I_l , I_r , ρ calculated from Stokes components I , Q , and U have shown unique characteristics with respect to nonspherical mineral dust aerosol par-

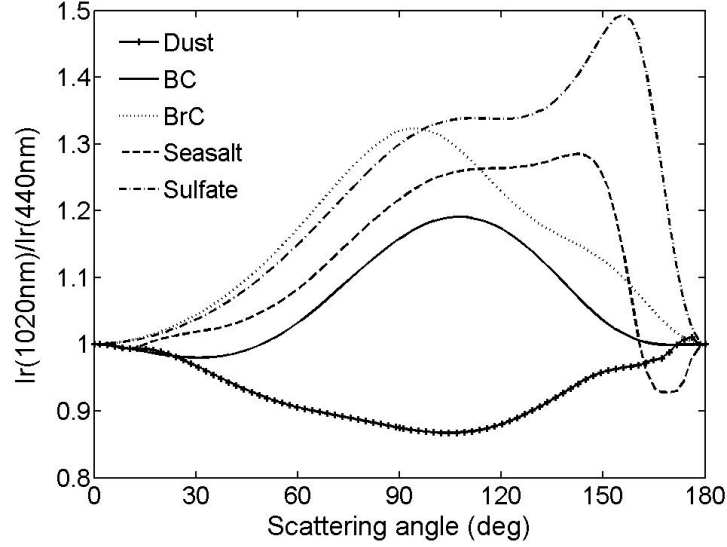


Figure 6.1: Spectral ratio of the perpendicular polarized radiance I_r for non-spherical dust particle with radii of 0.12 and 4.517 μm for fine and coarse modes (refractive index $m = 1.57 + 0.01i$ at 440 nm and $m = 1.57 + 0.001i$ at 1020 nm); for spherical BC particle with radius of 0.095 μm ($m = 1.95 + 0.66i$ at 440 and 1020 nm); for spherical BrC particle with radius of 0.126 μm ($m = 1.53 + 0.063i$ at 440 nm and $m = 1.53 + 0.005i$ at 1020 nm); for spherical seasalt particle with radii of 0.16 and 2.46 μm for fine and coarse modes ($m = 1.5 + 0.0i$ at 440 and 1020 nm); and for spherical sulfate particle with radius of 0.17 μm ($m = 1.53 + 0.0i$ at 440 and 1020 nm). The BC curve was simulated by the Mie code, and other curves were simulated by the Spheroid kernels, see Chapter 2.

ticles. Simulations have also shown that nonspherical dust particle can be distinguished from other spherical aerosol components including Black Carbon (BC), Brown Carbon (BrC), seasalt, and sulfate by spectral ratio of the perpendicular polarized radiance I_r , see Fig. 6.1. In the future, some subsequent studies are engaged utilizing these polarization parameters to derive aerosol particle shape parameter and help to identify aerosol types.

Bibliography

- Aben, I., Helderma, F., Stam, D. M., and Stammes, P. (1997). High-spectral resolution polarization measurements of the atmosphere with the GOME BBM. *Proceedings of SPIE the International Society For Optical Engineering*, pages 446–453.
- Arai, K. (2013). Method for Estimation of Aerosol Parameters Based on Ground Based Atmospheric Polarization Irradiance Measurements. *International Journal of Advanced Computer Science and Applications*, 4(2):226–233.
- Bass, M., Van Stryland, E. W., Williams, D. R., and L., W. W. (1995). *Handbook of Optics, Second Edition Volume I: Fundamentals, Techniques, and Design*. McGRAW-HILL, Inc.
- Bayat, A., Khalesifard, H., and Masoumi, A. (2013). Retrieval of aerosol single-scattering albedo and polarized phase function from polarized sun-photometer measurements for Zanjan’s atmosphere. *Atmospheric Measurement Techniques*, 6(10):2659–2669.
- Bhandari, P., Voss, K. J., Logan, L., and Twardowski, M. (2011). The variation of the polarized downwelling radiance distribution with depth in the coastal and clear ocean. *Journal of Geophysical Research: Oceans*, 116.
- Bodhaine, B. A., Wood, N. B., Dutton, E. G., and Slusser, J. R. (1999). On Rayleigh Optical Depth Calculations. *Journal of Atmospheric and Oceanic Technology*, pages 1854–1860.

BIBLIOGRAPHY

- Boesche, E., Stammes, P., Ruhtz, T., Preusker, R., and Fischer, J. (2006). Effect of aerosol microphysical properties on polarization of skylight: sensitivity study and measurements. *Applied optics*, 45(34):8790–8805.
- Boucher, O., Randall, D., Artaxo, P., Bretherton, C., Feingold, G., Forster, P., Kerminen, V. M., Kondo, Y., Liao, H., Lohmann, U., Rasch, P., Satheesh, S., Sherwood, S., Stevens, B., and Zhang, X. (2013). *Climate Change 2013: The Physical Science Basis. Contribution of Working Group I to the Fifth Assessment Report of the Intergovernmental Panel on Climate Change*. Cambridge University Press.
- Buchwitz, M., Eichmann, K., Rozanov, A., and Burrows, J. (2004). *User’s Guide for the Software Package SCIATRAN (Radiative Transfer Model and Retrieval Algorithm)*, 2.0 edition.
- Cairns, B., Russell, E. E., and Travis, L. D. (1999). Research scanning polarimeter: calibration and ground-based measurements. In *SPIE’s International Symposium on Optical Science, Engineering, and Instrumentation*, pages 186–196.
- CE318Manual (2014). *SunPhotometer User Manual*, 4.6 edition.
- Chen, C., Li, Z., Li, D., Li, K., Zhang, Y., Hou, W., and Xie, Y. (2013). Ground-based Polarization Remote Sensing of Atmospheric Aerosols and the Correlation between Polarization Degree and PM_{2.5}. Earth and Environmental Science, Beijing. The ISRSE 35 Technical Program Committee, IOP.
- Chen, L., Hong, J., Qiao, Y., Sun, X., and Wang, Y. (2008). Accuracy analysis on a sort of polarized measurement in remote sensing. *Spectroscopy and Spectral Analysis*, 28(10):2384–2387.
- Chen, L., Meng, F., Yuan, Y., and Zheng, X. (2012). High-precision Variable Polarization Light Source. In *2012 International Workshop on Information and Electronics Engineering*, volume 29 of *Procedia Engineering*, pages 1835–1839.

BIBLIOGRAPHY

- Cheng, T., Gu, X., Yu, T., and Tian, G. (2010). The reflection and polarization properties of non-spherical aerosol particles. *Journal of Quantitative Spectroscopy and Radiative Transfer*, 111(6):895–906.
- Coulson, K. L. (1988). *Polarization and Intensity of Light in the Atmosphere*. A. Deepak Pub.
- De Rooij, W. and Van der Stap, C. (1984). Expansion of Mie scattering matrices in generalized spherical functions. *Astronomy and Astrophysics*, 131(2):237–248.
- Deuzé, J., Bréon, F., Devaux, C., Goloub, P., Herman, M., Lafrance, B., Maignan, F., Marchand, A., Nadal, F., Perry, G., et al. (2001). Remote sensing of aerosols over land surfaces from POLDER-ADEOS-1 polarized measurements. *Journal of Geophysical Research: Atmospheres*, 106:4913–4926.
- Deuzé, J., Herman, M., and Santer, R. (1989). Fourier series expansion of the transfer equation in the atmosphere-ocean system. *Journal of Quantitative Spectroscopy and Radiative Transfer*, 41(6):483–494.
- Dubovik, O., Holben, B. N., Lapyonok, T., Sinyuk, A., Mishchenko, M. I., Yang, P., and Slutsker, I. (2002). Non-spherical aerosol retrieval method employing light scattering by spheroids. *Geophysical Research Letters*, 29(10):54–1–54–4.
- Dubovik, O., Sinyuk, A., Lapyonok, T., Holben, B. N., Mishchenko, M., Yang, P., Eck, T. F., Volten, H., Muñoz, O., Veihelmann, B., et al. (2006). Application of spheroid models to account for aerosol particle nonsphericity in remote sensing of desert dust. *Journal of Geophysical Research: Atmospheres*, 111(D11208).
- Emde, C., Buras, R., Mayer, B., and Blumthaler, M. (2010). The impact of aerosols on polarized sky radiance: model development, validation, and applications. *Atmospheric Chemistry and Physics*, 10(2):383–396.

BIBLIOGRAPHY

- Evans, K. and Stephens, G. (1991). A new polarized atmospheric radiative transfer model. *Journal of Quantitative Spectroscopy and Radiative Transfer*, 46(5):413–423.
- Feng, W., Ji, Y., and Chen, L. (2013). The impact of signal-noise ratio on degree of linear polarization measurement. *Optik*, 124(3):192–194.
- Goldstein, D. (2003). *Polarized Light*. Marcel Dekker, Inc., second edition.
- Goloub, P., Li, Z., Dubovik, O., Blarel, L., Podvin, T., Jankowiak, I., Lecoq, R., Deroo, C., Chatenet, B., Morel, J., et al. (2007). PHOTONS/AERONET sunphotometer network overview: description, activities, results. In *Fourteenth International Symposium on Atmospheric and Ocean Optics/Atmospheric Physics*, volume 6936. International Society for Optics and Photonics.
- Gu, X., Cheng, T., Xie, D., Li, Z., Yu, T., Li, D., and Qiao, Y. (2010). Aerosol retrieval over cities using an airborne directional polarimetric camera. *SPIE Newsroom*.
- Hasekamp, O. P. and Landgraf, J. (2007). Retrieval of aerosol properties over land surfaces: capabilities of multiple-viewing-angle intensity and polarization measurements. *Applied optics*, 46(16):3332–3344.
- He, X., Pan, D., Bai, Y., Wang, D., and Hao, Z. (2014). A new simple concept for ocean colour remote sensing using parallel polarisation radiance. *Scientific Reports*, 4.
- Holben, B., Eck, T., Slutsker, I., Tanre, D., Buis, J., Setzer, A., Vermote, E., Reagan, J., Kaufman, Y., Nakajima, T., et al. (1998). AERONET—A federated instrument network and data archive for aerosol characterization. *Remote sensing of environment*, 66(1):1–16.
- Horváth, G. and Varjú, D. (2004). *Polarized light in animal vision: polarization patterns in nature*. Springer.
- Hovenier, J., Cornelis, V. M. v. d. M., and Domke, H. (2004). *Transfer of Polarized Light in Planetary Atmospheres: Basic Concepts and Practical Methods*, volume 318. Springer.

BIBLIOGRAPHY

- Hovenier, J. and van der Mee, C. V. M. (1988). Scattering of polarized light - Properties of the elements of the phase matrix. *Astronomy and Astrophysics*, 196(1-2):287–295.
- Kobayashi, H., Hayashi, M., Shiraishi, K., Nakura, Y., Enomoto, T., Miura, K., Takahashi, H., Igarashi, Y., Naoe, H., Kaneyasu, N., Nishizawa, T., and Sugimoto, N. (2014). Development of a polarization optical particle counter capable of aerosol type classification. *Atmospheric Environment*, 97:486–492.
- Kokhanovsky, A. A. (2003). *Polarization optics of random media*. Springer.
- Kokhanovsky, A. A. (2006). *Light Scattering*. Springer.
- Kokhanovsky, A. A., Budak, V. P., Cornet, C., Duan, M., Emde, C., Katsev, I. L., Klyukov, D. A., Korkin, S. V., et al. (2010). Benchmark results in vector atmospheric radiative transfer. *Journal of Quantitative Spectroscopy and Radiative Transfer*, 111(12):1931–1946.
- Lafrance, B. and Hagolle, O. (2010). *Successive Order of Scattering radiative transfer code User Guide*, 5.0 edition.
- Lenoble, J., Herman, M., Deuzé, J., Lafrance, B., Santer, R., and Tanré, D. (2007). A successive order of scattering code for solving the vector equation of transfer in the earth’s atmosphere with aerosols. *Journal of Quantitative Spectroscopy and Radiative Transfer*, 107(3):479–507.
- Li, L., Li, Z., Li, K., Blarel, L., and Wendisch, M. (2014a). A method to calculate Stokes parameters and angle of polarization of skylight from polarized CIMEL sun/sky radiometers. *Journal of Quantitative Spectroscopy and Radiative Transfer*, 149:334–346.
- Li, L., Li, Z., and Wendisch, M. (2013). Simulation of the influence of aerosol particles on Stokes parameters of polarized skylight. Earth and Environmental Science, Beijing. The ISRSE 35 Technical Program Committee, IOP.

BIBLIOGRAPHY

- Li, Z., Blarel, L., Podvin, T., Goloub, P., Buis, J., and Morel, J. (2008). Transferring the calibration of direct solar irradiance to diffuse-sky radiance measurements for CIMEL Sun-sky radiometers. *Applied Optics*, 47(10):1368–1377.
- Li, Z., Blarel, L., Podvin, T., Goloub, P., and Chen, L. (2010). Calibration of the degree of linear polarization measurement of polarized radiometer using solar light. *Applied optics*, 49(8):1249–1256.
- Li, Z., Eck, T., Zhang, Y., Zhang, Y., Li, D., Li, L., Xu, H., Hou, W., Lv, Y., Goloub, P., et al. (2014b). Observations of residual submicron fine aerosol particles related to cloud and fog processing during a major pollution event in Beijing. *Atmospheric Environment*.
- Li, Z., Goloub, P., Devaux, C., Gu, X., Deuzé, J. L., Qiao, Y., and Zhao, F. (2006). Retrieval of aerosol optical and physical properties from ground-based spectral, multi-angular, and polarized sun-photometer measurements. *Remote Sensing of Environment*, 101(4):519–533.
- Li, Z., Goloub, P., Dubovik, O., Blarel, L., Zhang, W., Podvin, T., Sinyuk, A., Sorokin, M., Chen, H., Holben, B., et al. (2009). Improvements for ground-based remote sensing of atmospheric aerosol properties by additional polarimetric measurements. *Journal of Quantitative Spectroscopy and Radiative Transfer*, 110(17):1954–1961.
- Li, Z., Li, D., Li, K., Xu, H., Chen, X., Chen, C., Xie, Y., Li, L., Li, L., Li, W., Lv, Y., Qie, L., Zhang, Y., and Gu, X. (2015). Sun-sky radiometer observation network with the extension of multi-wavelength polarization measurements. *Journal of Remote Sensing*, 19(3):496–520.
- Liou, K. (2002). *An introduction to atmospheric radiation*, volume 84. Academic press.
- Liu, Y. and Voss, K. (1997). Polarized radiance distribution measurement of skylight. II. Experiment and data. *Applied optics*, 36(33):8753–8764.

BIBLIOGRAPHY

- Marbach, T., Phillips, P., and Schlüssel, P. (2013). 3MI: The Multi-Viewing Multi-Channel Multi-Polarization Imaging Mission of the EUMETSAT Polar System-Second Generation (EPS-SG) dedicated to aerosol characterization. In *RADIATION PROCESSES IN THE ATMOSPHERE AND OCEAN (IRS2012): Proceedings of the International Radiation Symposium (IRC/IAMAS)*, volume 1531, pages 344–347. AIP Publishing.
- Merikallio, S., Lindqvist, H., Nousiainen, T., and Kahnert, M. (2011). Modelling light scattering by mineral dust using spheroids: assessment of applicability. *Atmospheric Chemistry and Physics*, 11(11):5347–5363.
- Mishchenko, M. I. and Travis, L. D. (1998). Capabilities and limitations of a current FORTRAN implementation of the T -matrix method for randomly oriented, rotationally symmetric scatterers. *Journal of Quantitative Spectroscopy and Radiative Transfer*, 60(3):309–324.
- Mishchenko, M. I., Travis, L. D., Kahn, R. A., and West, R. A. (1997). Modeling phase functions for dustlike tropospheric aerosols using a shape mixture of randomly oriented polydisperse spheroids. *Journal of Geophysical Research Atmospheres*, 102(D14):16831–16847.
- Mishchenko, M. I., Travis, L. D., and Lacis, A. A. (2002). *Scattering, absorption, and emission of light by small particles*. Cambridge university press.
- Nousiainen, T., Kahnert, M., and Lindqvist, H. (2011). Can particle shape information be retrieved from light-scattering observations using spheroidal model particles? *Journal of Quantitative Spectroscopy and Radiative Transfer*, 112(13):2213–2225.
- Okamura, Y., Tanaka, K., Amano, T., Hiramatsu, M., and Shiratama, K. (2008). Breadboarding activities of the Second-generation Global Imager (SGLI) on GCOM-C.
- Peralta, R. J., Nardell, C., Cairns, B., Russell, E. E., Travis, L. D., Mishchenko, M. I., Fafaul, B. A., and Hooker, R. J. (2007). Aerosol polarimetry sensor for the Glory Mission. In *International Symposium on*

BIBLIOGRAPHY

- Multispectral Image Processing and Pattern Recognition*. International Society for Optics and Photonics.
- Pietras, C., Miller, M., Ainsworth, E., Frouin, R., Holben, B., and Voss, K. (2000). Calibration of sun photometers and sky radiance sensors. Technical report, Goddard Space Flight Space Center, Greenbelt, Maryland.
- Pomozi, I., Horvath, G., and Wehner, R. (2001). How the clear-sky angle of polarization pattern continues underneath clouds: full-sky measurements and implications for animal orientation. *Journal of Experimental Biology*, 204(17):2933–2942.
- Pust, N. J. and Shaw, J. A. (2008). Digital all-sky polarization imaging of partly cloudy skies. *Applied optics*, 47(34):H190–H198.
- Rozanov, V., Buchwitz, M., Eichmann, K., De Beek, R., and Burrows, J. (2002). SCIATRAN—a new radiative transfer model for geophysical applications in the 240–2400 nm spectral region: The pseudo-spherical version. *Advances in Space Research*, 29(11):1831–1835.
- Rozanov, V. and Kokhanovsky, A. (2006). The solution of the vector radiative transfer equation using the discrete ordinates technique: selected applications. *Atmospheric Research*, 79(3):241–265.
- Rozanov, V., Rozanov, A., Kokhanovsky, A., and Burrows, J. (2014). Radiative transfer through terrestrial atmosphere and ocean: software package SCIATRAN. *Journal of Quantitative Spectroscopy and Radiative Transfer*, 133:13–71.
- Schuster, G. L., Dubovik, O., and Holben, B. N. (2006). Angstrom exponent and bimodal aerosol size distributions. *Journal of Geophysical Research: Atmospheres*, 111(D7):234–244.
- Schutgens, N., Tilstra, L., Stammes, P., and Bréon, F. (2004). On the relationship between Stokes parameters Q and U of atmospheric ultraviolet/visible/near-infrared radiation. *Journal of Geophysical Research: Atmospheres*, 109(D9).

BIBLIOGRAPHY

- Smith, G. S. (2007). The polarization of skylight: An example from nature. *American Journal of Physics*, 75(1):25–35.
- Song, M., Sun, B., Sun, X., and Hong, J. (2012). Polarization calibration of airborne multi-angle polarimetric radiometer. *Optics and Precision Engineering*, 20(6):1153–1158.
- Stam, D., Aben, I., and Helderman, F. (2002). Skylight polarization spectra: Numerical simulation of the Ring effect. *Journal of Geophysical Research: Atmospheres*, 107(D20).
- Sun, W., Liu, Z., Videen, G., Fu, Q., Muinonen, K., M., W. D., Lukashin, C., Jin, Z., Lin, B., and Huang, J. (2013). For the depolarization of linearly polarized light by smoke particles. *Journal of Quantitative Spectroscopy and Radiative Transfer*, 122(2):233–237.
- Sun, X., Wang, H., Shen, J., and Liu, W. (2012). Depolarization and Polarization of Light Scattering by Dustlike Tropospheric Aerosols. *Journal of Electromagnetic Waves and Applications*, 24(10):1353–1364.
- Taylor, J. R. (1982). *An Introduction to Error Analysis: The Study of Uncertainties in Physical Measurements*. Mill Valley: Unversity Science Books.
- Tilstra, L., Schutgens, N., and Stammes, P. (2003). Analytical calculation of Stokes parameters Q and U of atmospheric radiation. Scientific report, Koninklijk Nederlands Meteorologisch Instituut (KNMI), De Bilt, The Netherlands.
- Vermeulen, A., Devaux, C., and Herman, M. (2000). Retrieval of the scattering and microphysical properties of aerosols from ground-based optical measurements including polarization. I. Method. *Applied optics*, 39(33):6207–6220.
- Voss, K. J. and Liu, Y. (1997). Polarized radiance distribution measurements of skylight. I. System description and characterization. *Applied optics*, 36(24):6083–6094.

BIBLIOGRAPHY

- Wang, H., Sun, X., Sun, B., Liang, T., Li, C., and Hong, J. (2014a). Retrieval of aerosol optical properties over a vegetation surface using multi-angular, multi-spectral, and polarized data. *Advances in Atmospheric Sciences*, 31(4):879–887.
- Wang, J., Xu, X., Ding, S., Zeng, J., Spurr, R., Liu, X., Chance, K., and Mishchenko, M. (2014b). A numerical testbed for remote sensing of aerosols, and its demonstration for evaluating retrieval synergy from a geostationary satellite constellation of GEO-CAPE and GOES-R. *Journal of Quantitative Spectroscopy and Radiative Transfer*, 146:510–528.
- Wendisch, M. and von Hoyningen-Huene, W. (1994). Possibility of refractive index determination of atmospheric aerosol particles by ground-based solar extinction and scattering measurements. *Atmospheric Environment*, 28(5):785–792.
- Wendisch, M. and Yang, P. (2012). *Theory of atmospheric radiative transfer*. Wiley-VCH.
- Zdunkowski, W., Trautmann, T., and Bott, A. (2007). *Radiation in the atmosphere: A course in theoretical meteorology*. Cambridge University Press.
- Zeng, J., Han, Q., and Wang, J. (2008). High-spectral resolution simulation of polarization of skylight: Sensitivity to aerosol vertical profile. *Geophysical Research Letters*, 35(20).
- Zhang, J. (2006). The calculating formulae, and experimental methods in error propagation analysis. *IEEE Transactions on Reliability*, 55(2):169–181.

Nomenclature

Symbol	Description	Unit
α	Size parameter	—
β	Ellipticity angle	rad or °
\mathbf{A}	Complex scattering matrix	—
\mathbf{F}	Scattering matrix	—
\mathbf{F}^{nor}	Normalized form of scattering matrix	—
\mathbf{L}	4×4 rotation matrix	—
\mathbf{P}	Phase matrix	—
\mathbf{R}	2×2 rotation matrix	—
χ	Angle of polarization	rad or °
δ	Orientation angle of the 0° polarizer axis of perfect installation with respect to the reference plane	rad or °
ϵ	Complex electric permittivity	A s V ⁻¹ m ⁻¹
η	Polarizing efficiency	—
γ	Initial angle of the polarizer axis with respect to the orientation of perfect installation	rad or °
$\hat{l}, \hat{r}, \hat{z}$	Unit vectors along axes of Cartesian coordinate system	—
$\hat{l}_{\text{ins}}, \hat{r}_{\text{ins}}, \hat{z}_{\text{ins}}$	Unit vectors in the instrument frame	—
$\hat{l}_{\text{sky}}, \hat{r}_{\text{sky}}, \hat{z}_{\text{sky}}$	Unit vectors in the sky frame	—

6 Nomenclature

κ	Complex magnetic permeability	$\text{V s A}^{-1} \text{ m}^{-1}$
λ	Wavelength	nm or μm
Ω	Solid angle	sr
μ	Zenith distance	—
ϕ_{abs}	Absorption radiant energy flux	W
ϕ_{ext}	Extinction radiant energy flux	W
ϕ_{sca}	Scattering radiant energy flux	W
ψ	Orientation angle of polarizer axis for perfect installation	rad or $^\circ$
ρ	Depolarization ratio	—
$\sigma, \sigma_1, \sigma_2$	Rotation angle	rad or $^\circ$
θ	Zenith angle	rad or $^\circ$
φ	Azimuthal angle	rad or $^\circ$
ϖ	Single scattering albedo	—
Ψ	Orientation angle of the polarizer axis	rad or $^\circ$
ϑ	Scattering angle	rad or $^\circ$
\vec{E}	Complex electric field vector	V m^{-1}
\vec{S}	Stokes Vector	W m^{-2}
\vec{S}_0	Solar irradiance Stokes vector	W m^{-2}
A	Surface area	m^2
a	Horizontal semi-axis of the spheroid particle	μm
a/b	Axial ratio of the spheroid particle	—
A_{proj}	Projected particle cross section	m^2
$A_{i,j}, i, j = 1, 2$	Complex scattering amplitudes	—
B	Planck's function	$\text{W m}^{-2} \text{ nm}^{-1} \text{ sr}^{-1}$
b	Rotational (vertical) semi-axis of the spheroid particle	μm
b_{abs}	Volumetric absorption coefficient	m^{-1}
b_{ext}	Volumetric extinction coefficient	m^{-1}
b_{sca}	Volumetric scattering coefficient	m^{-1}
C	Calibration coefficient of the polar- ized radiance	—

6 Nomenclature

c	Speed of light in a vacuum	m s^{-1}
C_{abs}	Absorption cross section	m^2
C_{ext}	Extinction cross section	m^2
C_{sca}	Scattering cross section	m^2
E	Complex amplitude of the electric field vector	V m^{-1}
E_l	Electric field component parallel to the reference plane	V m^{-1}
E_r	Electric field component perpendicular to the reference plane	V m^{-1}
F	Total irradiance	W m^{-2}
f	Scattering function	—
F_0	Extraterrestrial solar flux density, or irradiance	W m^{-2}
F_{inc}	Incident radiant flux density, or irradiance	W m^{-2}
$F_{i,j}, i, j = 1, 2, 3, 4$	Elements of the scattering matrix	—
g	Asymmetry factor	—
h	Planck's constant	J s
I	Total radiance	$\text{W m}^{-2} \text{ nm}^{-1} \text{ sr}^{-1}$
I_0	Total radiance of directly incident sunlight at the TOA	$\text{W m}^{-2} \text{ nm}^{-1} \text{ sr}^{-1}$
I_l	Component of radiance parallel to the reference plane	$\text{W m}^{-2} \text{ nm}^{-1} \text{ sr}^{-1}$
I_r	Component of radiance perpendicular to the reference plane	$\text{W m}^{-2} \text{ nm}^{-1} \text{ sr}^{-1}$
I_{lin}	Linearly polarized radiance	$\text{W m}^{-2} \text{ nm}^{-1} \text{ sr}^{-1}$
I_{unp}	Unpolarized radiance	$\text{W m}^{-2} \text{ nm}^{-1} \text{ sr}^{-1}$
$I_{l,\text{unp}}$	Parallel component of the unpolarized radiance	$\text{W m}^{-2} \text{ nm}^{-1} \text{ sr}^{-1}$
$I_{r,\text{unp}}$	Perpendicular component of the unpolarized radiance	$\text{W m}^{-2} \text{ nm}^{-1} \text{ sr}^{-1}$
$I_{l,\text{lin}}$	Parallel component of the linearly polarized radiance	$\text{W m}^{-2} \text{ nm}^{-1} \text{ sr}^{-1}$

6 Nomenclature

$I_{r,\text{lin}}$	Perpendicular component of the linearly polarized radiance	$\text{W m}^{-2} \text{ nm}^{-1} \text{ sr}^{-1}$
k	Wavenumber	nm^{-1}
k_1	Transmittance of the linear polarizer along the preferred axis	—
k_1	Transmittance of the linear polarizer along the preferred axis	—
k_2	Transmittance of the linear polarizer along an axis 90° to the preferred axis	—
k_2	Transmittance of the linear polarizer along an axis 90° to the preferred axis	—
k_B	Boltzmann constant	J K^{-1}
m	Complex refractive index	—
m_i	Imaginary part of complex refractive index	—
m_r	Real part of complex refractive index	—
N	Digital number	—
p	Phase function	—
$P_{i,j}, i, j = 1, 2, 3, 4$	Elements of the phase matrix	—
Q	Parallel minus perpendicular linear irradiance	W m^{-2}
Q	Second Stokes parameter of the monochromatic specific intensity vector	$\text{W m}^{-2} \text{ nm}^{-1} \text{ sr}^{-1}$
Q_{abs}	Absorption efficiency factor	—
Q_{ext}	Extinction efficiency factor	—
Q_{sca}	Scattering efficiency factor	—
R	Radial distance from a scattering particle	m
r	Radius of a sphere	μm
R_{12}, R_{13}	Calibration coefficient of the <i>DoLP</i>	—

S_1, S_2	Elements of the rotation matrix	—
T	Absolute temperature	K
t	Time	s
U	Linear polarized irradiance under 45°	W m^{-2}
U	Third Stokes parameter of the monochromatic specific intensity vector	$\text{W m}^{-2} \text{ nm}^{-1} \text{ sr}^{-1}$
V	Circularly polarized irradiance	W m^{-2}
V	Fourth Stokes parameter of the monochromatic specific intensity vector	$\text{W m}^{-2} \text{ nm}^{-1} \text{ sr}^{-1}$
X_1, X_2	Elements of the rotation matrix	—
z	Cartesian coordinate in the direction of the propagation of the incident EM wave	m
\mathbf{M}_a	Mueller matrix of the aerosol particles	—
\mathbf{M}_{ms}	Mueller matrix of multiple scatterings	—
\mathbf{M}_m	Mueller matrix of the air molecules	—
\mathbf{M}_p	Instrument's Mueller matrix	—
$dN/d \ln r$	Number particle size distribution	cm^{-3}
$dV/d \ln r$	Volume particle size distribution	$\mu\text{m}^3 \mu\text{m}^{-2}$
σ_i	Standard deviation	—
τ	Optical depth	—
$C_{V,i}$	Particle volume concentration	$\mu\text{m}^3 \mu\text{m}^{-2}$
$r_{V,i}$	Volume median radius	μm

Acronyms

AERONET	AErosol RObotic NETwork
AMPR	advanced Atmosphere Multi-angle Polarization Radiometer
<i>AoP</i>	Angle of Polarization
AOD	Aerosol Optical Depth
APS	Aerosol Polarimetry Sensor
ALM	ALMucantar
ALMP	Polarized ALMucantar
AIOFM	Anhui Institute of Optics and Fine Mechanics
BC	Black Carbon
BrC	Brown Carbon
CE318-DP	CIMEL Dual-Polar sun/sky radiometer
CAS	Chinese Academy of Sciences
<i>DoP</i>	Degree of Polarization
<i>DoLP</i>	Degree of Linear Polarization
<i>DoCP</i>	Degree of Circular Polarization
DOM	Discrete Ordinate Method

DPC	Directional Polarimetric Camera
EM	Electromagnetic
LOA	Laboratoire d'Optique Atmosphérique
LIM	Leipziger Institut für Meteorologie
3MI	Multi-Viewing Multi-Channel Multi-Polarization Imaging Mission
PHOTONS	PHOtométrie pour le Traitement Opérationnel de Normalisation Satellitaire
POLDER	Polarization and Directionality of Earth's Reflectances
PPP	Polarized Principle Plane
<i>RAA</i>	Relative Azimuthal Angle
RADI	Institute of Remote Sensing and Digital Earth
RSP	Research Scanning Polarimeter
SGLI-VNR	Second Generation Global Imager-Visible and Near Infrared Radiometer
SONET	Sun/sky-radiometer Observation NETwork
SOS	Successive Order of Scattering
SPP	Solar Principle Plane
SSA	Single Scattering Albedo
TOA	top of the atmosphere
UV	UltraViolet
VPOLS	Variable POLarization Light Source

List of Figures

2.1	Illustration of the reference planes. XO indicates the solar incident direction; OH denotes the local zenith; and YO is the viewing direction. The gray plane XOH is the solar principal plane which contains the directions of the incident sunlight and the local zenith; the plane YOH is the local meridian plane which contains the viewing direction and the local zenith; the plane XOY is the scattering plane which contains the direction of the incident sunlight and the scattered light in the viewing direction.	11
2.2	Relation between the angle of polarization and signs of Stokes parameters Q and U	13
2.3	Input microphysical parameters and output optical parameters of the single scattering calculation.	25
2.4	Simplified schematic diagram of scattering contributors to the ground-based polarimetric radiometer measurements in a clear, cloudless sky. The plane of the paper is the scattering plane. Redrawn according to Pust and Shaw (2008) with modification.	33
3.1	The new ground-based CIMEL Dual-Polar sun/sky radiometer (left: CE318-DP#962; top-right: the optical sensor head fixed on the automated mount; bottom-right: the electronic box).	40

LIST OF FIGURES

3.2	Schematic diagram of mechanism of the Dual-Polar sun/sky radiometer. Upper layer represents the polarizers' wheel and lower layer is the filters' wheel. The downward rays indicate incidence of the radiation. The double-headed arrows indicate the orientations of polarizers' transmittance axes. With rotations of these two wheels and combinations of different polarizers and filters, the CE318-DP conducts multi-wavelength polarization measurements. Drawn originally by Kaitao Li with modification.	41
3.3	Installation of the optical sensor head and arm of the automated mount of CE318-DP. (a) ideal installation with the optical sensor head perpendicular to the arm of the automated mount; (b) non-ideal installation with an initial error angle between the orange line and the yellow line, where γ indicates the initial angle with respect to the orientation of ideal installation.	43
3.4	Observation geometries of the CE318-DP. (a) "SPP" denotes the Solar Principal Plane scenario (non-polarization); "PPP" indicates the Polarized Principal Plane scenario. (b) "ALM" represents the ALMucantar scenario (non-polarization); "ALMP" denotes the Polarized ALMucantar scenario (Li et al., 2015).	43
3.5	Schematic diagram of calibration of the polarized radiances for the polarized channels of CE318-DP.	46
3.6	The SNET long-term site map (red dots denote 12 polarization observation sites, and green dots represent 5 non-polarization observation sites).	48

LIST OF FIGURES

4.1	Schematic diagram of the reference coordinate systems in the sky frame ($\hat{l}_{\text{sky}}, \hat{r}_{\text{sky}}, \hat{z}_{\text{sky}}$) and in the instrument frame ($\hat{l}_{\text{ins}}, \hat{r}_{\text{ins}}, \hat{z}_{\text{ins}}$) for the viewing direction of 180° . The instrument is placed at the origin of the reference coordinate systems O . \hat{l}_{sky} -axis is in the meridian plane (i.e., the principal plane in this situation). \hat{l}_{ins} -axis is along the 0° polarizer axis of the instrument. \hat{z}_{sky} - and \hat{z}_{ins} - axes are coincident, along the direction of the light propagation. \hat{r}_{sky} -axis is perpendicular to the meridian plane. \hat{r}_{ins} -axis is perpendicular to both \hat{l}_{ins} - and \hat{z}_{ins} -axes. σ is a rotation angle for transforming of the reference coordinate systems.	52
4.2	The signs of the Stokes parameters Q (a) and U (b). Redrawn from http://en.wikipedia.org with modification.	53
4.3	Schematic diagram of the processes of skylight polarization detected by the CE318-DP.	54
4.4	Illustration of the orientation angles of a set of triplet linear polarizer axes in the sky frame for the viewing direction of 180° . The instrument is located at the origin O . The light is traveling perpendicular into the paper. \hat{l}_{sky} -axis is in the meridian plane (i.e., the principal plane in this situation). \hat{l}_{ins} -axis is along the 0° polarizer axis of the instrument. They are corresponding to \hat{l}_{sky} - and \hat{l}_{ins} -axes in Fig. 4.1. σ is the rotation angle for transforming of the reference coordinate systems. “P1”, “P2”, and “P3” denote the 0° , 60° , and 120° polarizers, respectively. The blue double-headed arrows indicate the orientations of polarizers’ transmittance axes. The yellow double-headed arrow indicates the orientation of the 0° polarizer axis for ideal installation. The orientation angles of the three polarizer axes are $\sigma + 0^\circ$, $\sigma + 60^\circ$, and $\sigma + 120^\circ$. . .	58

LIST OF FIGURES

4.5	Counter plots of the polarization patterns of entire sky at 440 nm (simulated by SCIATRAN, where the aerosol type is “WMO-urban”; aerosol optical depth=1.0923; Rayleigh optical depth=0.24261; solar zenith angle=50.1293°; and the relative azimuthal angles of 0° and 180° indicate the solar and anti-solar directions of the principal plane, respectively).	62
4.6	Results of the total radiance I (a), $DoLP$ (b), the parallel and perpendicular polarized radiances I_l (dash line) and I_r (solid line) (c), and the depolarization ratio ρ (d) for the haze polluted urban case in the solar principal plane geometry at the “Beijing-RADI” site.	65
4.7	Results of the Stokes parameters Q (a,b), U (c,d), and AoP (e,f) for the haze polluted urban case in the solar principal plane geometry at the “Beijing-RADI” site.	66
4.8	Results of the total radiance I (a), $DoLP$ (b), the parallel and perpendicular polarized radiances I_l (dash line) and I_r (solid line) (c), and the depolarization ratio ρ (d) for the rural case in the solar principal plane geometry at the “ZhangyeHH” site.	67
4.9	Results of the Stokes parameters Q (a,b), U (c,d), and AoP (e,f) for the rural case in the solar principal plane geometry at the “ZhangyeHH” site.	68
4.10	Results of the total radiance I (a), $DoLP$ (b), the parallel and perpendicular polarized radiances I_l (dash line) and I_r (solid line) (c), and the depolarization ratio ρ (d) for the clean continental case in the solar principal plane geometry at the “Lhasa” site.	69
4.11	Results of the Stokes parameters Q (a,b), U (c,d), and AoP (e,f) for the clean continental case in the solar principal plane geometry at the “Lhasa” site.	70

LIST OF FIGURES

4.12	Results of the total radiance I (a), $DoLP$ (b), the parallel and perpendicular polarized radiances I_l (dash line) and I_r (solid line) (c), and the depolarization ratio ρ (d) for the mineral dust case in the solar principal plane geometry at the “Minqin” site.	71
4.13	Results of the Stokes parameters Q (a,b), U (c,d), and AoP (e,f) for the mineral dust case in the solar principal plane geometry at the “Minqin” site.	72
4.14	Results of the total radiance I (a), $DoLP$ (b), the parallel and perpendicular polarized radiances I_l (dash line) and I_r (solid line) (c), and the depolarization ratio ρ (d) for the Maritime case in the solar principal plane geometry at the “Zhoushan” site.	73
4.15	Results of the Stokes parameters Q (a,b), U (c,d), and AoP (e,f) for the Maritime case in the solar principal plane geometry at the “Zhoushan” site.	74
4.16	Schematic diagram of a 80° difference between the angles of polarization at 870, 1020 nm and at 1640 nm. Black point represents the rotating axis of the CE318-DP polarizers’ wheel; Blue points denote the detecting location for the UV-visible channels (e.g., 340, 380, 440, 500, 675, 870, and 1020 nm) and the detecting location for the near-infrared channels (e.g., 1640 nm). Note that the channels at 870, 1020, and 1640 nm employ the same set of polarizer triplets, but the sequence of measurements for the channels at 870 and 1020 nm (P1 to P2 to P3) differs from that for the channel at 1640 nm (P2 to P3 to P1).	77
4.17	Aerosol optical depth derived from the CE318-DP#350 sun measurements on December 7, 2013 following AERONET level 1.0 data criteria (Li et al., 2014a).	78

LIST OF FIGURES

4.18 Results of the total radiance I (a), $DoLP$ (b), the parallel and perpendicular polarized radiances I_l (dash line) and I_r (solid line) (c), and the depolarization ratio ρ (d) for the haze polluted urban case in the polarized almucantar geometry at the “Beijing-RADI” site.	85
4.19 Results of the Stokes parameters Q (a,b), U (c,d), and AoP (e,f) for the haze polluted urban case in the polarized almucantar geometry at the “Beijing-RADI” site.	86
4.20 Results of the total radiance I (a), $DoLP$ (b), the parallel and perpendicular polarized radiances I_l (dash line) and I_r (solid line) (c), and the depolarization ratio ρ (d) for the clear case in the polarized almucantar geometry at the “Beijing-RADI” site.	87
4.21 Results of the Stokes parameters Q (a,b), U (c,d), and AoP (e,f) for the clear case in the polarized almucantar geometry at the “Beijing-RADI” site.	88
4.22 Aerosol volume size distributions retrieved from the CE318-DP#350 measurements in the almucantar geometry at the “Beijing-RADI” site. (a) haze polluted case, (b) clear case. . .	92
5.1 (a) Comparison between the degree of linear polarization deduced from the Stokes parameters I , Q , U in this paper (points) with that calculated directly from three polarized radiance measurements (curves) in the solar principal plane; (b) Comparison between the first Stokes component I from polarized channel measurement (points) with the total radiance from the non-polarized channel measurement (curves) in the solar principal plane. The point notations are as: circle for 440 nm; diamond for 870 nm; triangle for 1020 nm; and cross for 1640 nm. The curve notations are as: dotted line for 440 nm; dashed line for 870 nm; dash-dot line for 1020 nm; and solid line for 1640 nm (Li et al., 2014a).	95

LIST OF FIGURES

5.2	Comparisons between results of the <i>DoLP</i> and the total radiance I calculated in this study and the SOS radiative transfer model simulations, where I is normalized by the extraterrestrial solar irradiance (Li et al., 2014a).	96
5.3	Comparisons between results of the Stokes parameters Q , U , and the <i>AoP</i> calculated in this study and the SOS radiative transfer model simulations, where Q and U are normalized by the extraterrestrial solar irradiance (Li et al., 2014a).	97
5.4	Ground-based synchronous observations by the CE318-DP #962 and the AMPR on 19 January, 2013 in Hefei, China (31.9N, 117.2E).	99
5.5	Comparisons of <i>DoLP</i> and the Stokes parameters I , Q , and U between the CE318-DP #962 and the AMPR measurements.	100
5.6	The high-precision Variable POLarization Light Source (VPOLS) system, cited from http://klocc.aiofm.ac.cn/yqsb	103
5.7	Relative digital numbers measured by the CE318-DP #350 for partially polarized incident light with a fixed <i>DoLP</i> (fixed dip angle of the glass plates) and polarization orientations (rotating angles of the VPOLS box) changing from 0° to 180° . P1, P2, and P3 represent the three polarizers for the same wavelength band; solid lines indicate positions of the wave peaks where the angles correspond to the linear polarizer-preferred transmission directions; and dash lines indicate positions of the wave valleys where the angles correspond to directions of 90° to the linear polarizer-preferred transmittance axes. (a) 440 nm, (b) 675 nm, (c) 870 nm, (d) 1020 nm.	105
5.8	<i>AoP</i> calculated from the CE318-DP #350 measurements for partially polarized incident light with a fixed <i>DoLP</i> and polarization orientations changing from 0° to 180° . (a) 440 nm, (b) 675 nm, (c) 870 nm, (d) 1020 nm.	106

5.9	Sensitivities of the <i>AoP</i> to real part of the refractive index m_r (a), imaginary part of the refractive index m_i (b), particle shape a/b (c), and particle size r (d). a/b is the axial ratio, where a is the horizontal semi-axis and b is the rotational (vertical) semi-axis of the spheroid particle. $a/b = 1$ indicate the spherical particle. r denotes radius of spherical particle. (Input parameters for the simulation are listed in Tab. 5.2. The Mie and T -matrix codes were used to calculate single scattering by spherical and non-spherical particles, respectively. Outputs of the particle optical properties, including extinction coefficient, asymmetry factor, single scattering albedo and expansion coefficients of scattering matrix were then put into the vector radiative transfer model SCIATRAN to simulate the Stokes parameters, and to further calculate angle of polarization.)	108
6.1	Spectral ratio of the perpendicular polarized radiance I_r for nonspherical dust particle with radii of 0.12 and 4.517 μm for fine and coarse modes (refractive index $m = 1.57 + 0.01i$ at 440 nm and $m = 1.57 + 0.001i$ at 1020 nm); for spherical BC particle with radius of 0.095 μm ($m = 1.95 + 0.66i$ at 440 and 1020 nm); for spherical BrC particle with radius of 0.126 μm ($m = 1.53 + 0.063i$ at 440 nm and $m = 1.53 + 0.005i$ at 1020 nm); for spherical seasalt particle with radii of 0.16 and 2.46 μm for fine and coarse modes ($m = 1.5 + 0.0i$ at 440 and 1020 nm); and for spherical sulfate particle with radius of 0.17 μm ($m = 1.53 + 0.0i$ at 440 and 1020 nm). The BC curve was simulated by the Mie code, and other curves were simulated by the Spheroid kernels, see Chapter 2.	120

List of Tables

2.1	Ranges of the angle of polarization χ determined by signs of Q and U for the linearly polarized light.	13
3.1	Center wavelengths, bandwidths (FWHM), polarization detection capabilities and detectors for different channels of CE318-DP (Li et al., 2015).	42
3.2	Observation angles for different polarization scenarios of the CE318-DP (Li et al., 2015).	44
3.3	Information on polarization observation sites of SONENT (listed in chronological order of site establishments).	49
4.1	Information on the cases of CE318-DP polarized principal plane observations in Figs. 4.6-4.15.	64
4.2	Atmospheric conditions for the skylight polarization measurements in the polarized almucantar geometry in haze polluted urban and clear cases shown in Figs. 4.18 to 4.21.	84
5.1	The degree of linear polarization of the VPOLS system with a fixed 60° orientation angle for the glass plates.	104
5.2	Input parameters of the radiative transfer simulation for the AoP sensitivity study in Fig. 5.9.	107

Acknowledgments

I would like to extend my sincere gratitude to my supervisors Prof. Manfred Wendisch and Prof. Zhengqiang LI. Prof. Wendisch is the sponsor of this research. He offered me the opportunity to work on this topic. He always took his time to discuss with me during my research stay at the Leipziger Institut für Meteorologie (LIM) and provided me very useful suggestions on this research. Prof. Wendisch encouraged me a lot whenever I thought I got stuck. He also gave me numerous comments to improve this thesis. I really enjoyed the time studying in his group. Prof. LI has rich knowledge and experiences in the field of polarimetric remote sensing of aerosol. He gave me a lot of instructive advices during this research. Prof. LI is the PI of SONET. Most of my research data was obtained from there. He also provided me much supports on polarization calibration and test of the new Polarized ALMucantar measurements based on the CE318-DP. This thesis would not have been possible without his guidance and help.

I am very grateful to the following scientists for sharing the scattering codes and the vector radiative transfer models (name of the codes in round brackets): Vladimir V. Rozanov (SCIATRAN), Bruno Lafrance and Olivier Hagolle (SOS), Michael I. Mishchenko (Mie and T -matrix codes), Oleg Dubovik and Tatyana Lapyonok (Spheroid kernels). Special thanks go to Kaitao LI and Donghui LI for their invaluable assistance to understand the structure of the CE318-DP instrument and to collect the measurement data of skylight polarization within SONET. I would like to thank Xiaobing SUN, P. Stammes, Yan CUI, Jin HONG for discussing the reference frame issue. Many thanks go to Alexei Rozanov, Ying ZHANG, Xiaoguang XU, Chao

6 Acknowledgments

LIU, Lei BI, and Weizhen HOU for discussing the vector radiative transfer calculation. I am also grateful to Huagang XIANG and Weizhen HOU for validating the Mueller matrix of the instrument. Han WANG, Bin SUN, Donghui LI, and Wei HUANG jointed the comparison experiment between the CE318-DP and AMPR; Jianjun LI, Kaitao LI, Yinlin YUAN, Fanggang MENG, and Qing KANG participated in the experiment of polarization calibration and measurements of the angle of polarizers; Yisong XIE and Lei LI gave me valuable information on properties of aerosol compositions. I am grateful to their contributions on this research.

I have benefited greatly from discussions with my colleagues at LIM, Universität Leipzig: Evelyn Jäkel, Vasileios Barlakas, Fanny Finger, Michael Schäfer, André Ehrlich, Clemens Fricke, Britta Mey, Eike Bierwirth, Marlen Brückner, Sebastian Otto, Dagmar Rosenow, Jörg Walther and Frank Werner. I also would like to thank the former and currents colleagues at RADI, Chinese Academy of Sciences (CAS): Hua XU, Xingfeng CHEN, Lili QIE, Yang LV, Aiqing WANG, Wanchun ZHANG, Zhao LIU, Yan MA, Fengxia ZHANG, Yuhuan ZHANG, Ling WANG, Wei HUANG, and many other colleagues. Many thank to my friends Shan HUANG and Wenjie REN for their encouragement during my stay in Germany. I express my deep gratitude to my husband Huagang XIANG for his patience, encouragement, and continuous support.

Financial support for me to study in Germany was given by the CAS-DAAD joint Fellowship Programme. This research was also supported by the Director's Foundation for Youth Scholars of RADI, CAS (Grant no. Y3SJ7300CX).

To my mother

Curriculum Vitae

PERSONAL

Name	Li Li
Date of Birth	21 March,1983
Place of birth	Beijing, China
Nationality	P.R. of China
Private address	3-1005 No.395 ChangPing Road ChangPing District, 100085, Beijing, China
Email	liligis@163.com

EDUCATION

1995-1998	junior school student at Beijing Shangzhuang Second Middle School
1998-2001	high school student at Beijing BaYi High School
2001-2005	undergraduate student at Beijing Normal University
2005	Bachelor of GIS (geographical information system)
2005-2008	postgraduate student at Institute of Remote Sensing Applications, CAS
2008	Master of SIP (signal and information processing)
2010-2016	doctoral candidate at

2012-2016	Institute of Remote Sensing and Digital Earth, CAS doctoral candidate at Universität Leipzig
-----------	---

PROFESSIONAL EXPERIENCE

2008-2010	Research assistant at Institute of Remote Sensing Applications, CAS
2011-2012	Research associate at Institute of Remote Sensing Applications, CAS
2013-2016	Research associate at Institute of Remote Sensing and Digital Earth, CAS